In-Situ Biodegradation of Organic Groundwater Contaminants: Delineating the Effect of Physical and Biological Processes by Reactive-Transport Modeling

Dissertation

der Mathematisch-Naturwissenschaftlichen Fakultät
der Eberhard Karls Universität Tübingen
zur Erlangung des Grades eines
Doktors der Naturwissenschaften
(Dr. rer. nat.)

vorgelegt von
Dipl.-Geol. Dominik Eckert
aus Groß-Umstadt

Tübingen
2014

Gedruckt mit Genehmigung der Mathematisch-Naturwissenschaftlichen Fakultät der Eberhard Karls Universität Tübingen.

Tag der mündlichen Qualifikation:	18.02.2015
Dekan:	Prof. Dr. Wolfgang Rosenstiel
1. Berichterstatter:	Prof. Dr.-Ing. Olaf A. Cirpka
2. Berichterstatter:	Prof. Dr. Peter Grathwohl

Abstract

Monitored Natural Attenuation (MNA) has emerged as a well recognized approach for the remediation of BTEX contaminated aquifers. In order to deem MNA as an adequate remediation scheme, their must exist proof of the occurrence of biodegradation processes at the site of interest. Furthermore, a comprehensive understanding of the coupled physical (e.g., advective transport, diffusion, and sorption) and biological (microbially-catalyzed contaminant degradation) processes, acting on the compound(s) of interest, is required to judge the natural attenuation potential of a certain site. This thesis is organized in two main parts. The first part focuses on the effects of transverse dispersion and sorption on the stable-carbon isotope signature of organic contaminants, and its potential interference with the assessment of in-situ biodegradation by compound-specific isotope analysis (CSIA). I performed scenario simulations for fringe-controlled ethylbenzene degradation in steady-state contaminant plumes, and analyzed a toluene-pulse experiment performed in an indoor model aquifer via reactive-transport modeling. The results of these two studies indicate that physical processes may affect the isotope signature of organic contaminants in groundwater systems, by either acting as rate-limiting step for biodegradation (e.g., transverse mixing in fringe-controlled biodegradation) or fractionating themselves between isotopically light and heavy contaminant molecules (e.g., transverse dispersion and sorption). The second part of this thesis addresses the influence of transient environmental conditions, such as the temporal absence of electron donors and/or acceptors (which might arise, e.g., due to changing hydraulic conditions) on in-situ biodegradation. I analyzed toluene degradation experiments, performed under aerobic conditions in one and two-dimensional bench-scale porous flow-through systems, by reactive-transport modeling. The analysis indicated that temporal periods of starvation of up to four months, which were induced in the experiments by interrupting the injection of the growth-substrate toluene, did not drastically reduce the biodegradation potential. To capture the dynamics of the system, the numerical modeling approach necessitated the inclusion of microbial dormancy, i.e., the switch to an 'inactive' state of low metabolic activity under unfavorable conditions, as well as peak cell detachment during growth of sessile bacteria.

Kurzfassung

Natürliche Schadstoffminderungsprozesse (Natural Attenuation - NA) rücken bei der Sanierung von BTEX-Altlasten zunehmend in den Fokus. Um auf MNA (Monitored Natural Attenuation) als Sanierungsverfahren zurückgreifen zu können, muss der natürliche Schadstoffabbau am Standort sichergestellt und kontinuierlich überwacht werden. Weiter ist zur Bewertung des MNA-Potentials eines Standortes ein umfassendes Verständnis der physikalischen (z.B. advektiver Transport, Diffusion und Sorption) und biologischen (mikrobieller Schadstoffabbau) Prozesse, welche in natürlichen Systemen immer gleichzeitig auf den Schadstoff einwirken, nötig. Die vorliegende Dissertationsschrift ist in zwei Teile gegliedert. Der erste Teil beschäftigt sich mit dem Effekt von transversaler Dispersion und Sorption auf das Verhältnis der stabilen Kohlenstoff-Isotope ^{12}C und ^{13}C in organischen Schadstoffen. Ziel der Studien war es die Auswirkungen physikalisch induzierter Isotopenfraktionierung auf die Abschätzung des biologischen In-Situ Abbaus durch die Methode der substanzspezifischen Isotopen-Analyse (CSIA) zu untersuchen. Hierzu simulierte ich Szenarien des durchmischungskontrollierten Ethylbenzol-Abbaus in stationären Schadstofffahnen und analysierte ein Toluol Puls-Experiment mittels Reaktiver Transportmodellierung. Die Ergebnisse dieser beiden Studien zeigen, dass physikalische Prozesse das Isotopensignal organischer Schadstoffe auf zweierlei Weise beeinflussen können; (1) indem sie den geschwindigkeitsbestimmenden Schritt für den biologischen Abbau darstellen (z.B. transversale Dispersion in durchmischungskontrolliertem Schadstoffabbau) und (2) indem sie selbst zwischen leichten und schweren Isotopen fraktionieren (z.B. transversale Dispersion und Sorption). Der zweite Teil der vorliegenden Dissertationsschrift behandelt den Einfluss schwankender Umweltbedingungen, wie zum Beispiel die durch Änderungen im Fließregime bedingte räumliche Verlagerung einer Schadstofffahne, auf den biologischen In-Situ Abbau. Hierzu analysierte ich den Toluol-Abbau in ein- und zweidimensionalen Durchflussexperimenten unter aeroben Bedingungen mit numerischen Modellen. Die Ergebnisse dieser Analyse deuten darauf hin, dass temporäre Hungerphasen, welche in den Experimenten durch das Abstellen der Toluol-Zufuhr induziert wurden, bis zu einer Dauer von vier Monaten keinen gravierenden Einfluss auf das biologische Abbaupotential aerober Systeme haben. Damit das numerische Modell die Dynamik der Systeme abbilden konnte musste dieses explizit eine aktive, eine inaktive, sowie eine mobile Zellfraktion berücksichtigen.

Clarification

All studies presented in this thesis, except for chapter 3, were conducted in close collaboration with the working groups of Dr. Martin Elsner (Environmental Isotope Chemistry) and Dr. Christian Griebler (Microbial Ecology) at the Institute of Groundwater Ecology at the Helmholtz Center for Environmental Health in Munich. My part in these collaborations lay in the quantitative analysis and interpretation of multiple flow-through experiments at different scales by means of reactive-transport modeling. Neither the experiments, nor the measurements, which my analysis and modeling was based on, were performed by myself. In the following the people which provided the individual datasets are listed.

- The toluene-pulse experiment discussed in chapter 4 was performed under the lead of Dr. Shiran Qiu as part of his PhD thesis (Qiu, 2014), under the supervision of Dr. Martin Elsner.
- The continuous toluene injection experiment discussed in chapter 4 was performed under the lead of Dr. Agnieszka Monika Herzyk as part of her PhD thesis (Herzyk, 2013), under the supervision of Dr. Christian Griebler.
- The two-dimensional flow-through microcosm experiments discussed in chapters 5 and 6 were performed by Petra Kürzinger as part of her Master thesis (Kürzinger, 2007) and Dr. Robert Bauer, under the supervision of Dr. Christian Griebler.
- The batch and column experiments discussed in chapter 7 were performed by Michael Grösbacher as part of his PhD thesis (which had not been finished when this thesis was submitted), under the supervision of Dr. Christian Griebler.

The principle idea that transverse dispersion might mask degradation-induced isotope fractionation, if it is the rate-limiting step in fringe-controlled biodegradation, which chapter 3 is based on, was already developed during my time as Diploma student and was presented in my Diploma thesis (Eckert, 2011).

Acknowledgments

I would like to express my gratitude to a number of people without whom it would have been impossible to complete this work:

- **Prof. Dr.-Ing. Olaf A. Cirpka** for giving me the opportunity to write my PhD thesis in his working group, his continuous support, help, and guidance throughout my PhD work, his scientific inspiration, constant input of ideas and the fruitful and revealing discussions on my work,
- **Prof. Dr.-Ing. Massimo Rolle** for his guidance, support, scientific input and many insightful discussions, especially during the first year of my PhD work, the preparation of my first manuscript, and our joint attendance of the Goldschmidt Conference 2013,
- **Dr. Martin Elsner and his former PhD student Dr. Shiran Qiu** for the successful collaboration on the interpretation of a toluene-pulse experiment they conducted. I really enjoyed this work, the exchange of ideas and the interesting and fruitful discussions,
- **Dr. Chritian Griebler and his PhD student Michael Grösbacher** for the close collaboration on the effect of dynamic conditions on in-situ biodegradation. I appreciate the many inspiring discussions, the input of new ideas, and last but not least Michaels patience in performing all the experiments to gather the experimental data.

Further, I would like to thank Prof. Dr. Peter Grathwohl for correcting and evaluating this thesis, DFG and the Helmholtz Association for funding my research, Dr. Christina Haberer and Adrian Mellage for insightful and helpful discussions, and Willi Kappler and his team for their support with computer and printer issues. Special thanks I also want to express to all former and recent members of the "mensa team" as well as the hydrogeolgy group for the wonderful time and all the tasty cakes we shared. Last but not least I want to thank the love of my life, my wife Simone Gerwig, and my family for their unconditional support and love.

Contents

List of Figures

List of Tables

Chapter 1

Introduction

1.1 Motivation

Human activity has resulted in the contamination of soils and groundwater with toxic chemicals worldwide. The European Soil Data Center of the European Commission estimated that approximately 350.000 contaminated sites in Europe are in need of remediation, one third of which has been identified and only about 15% have been remediated so far (Panagos et al., 2013).

Monitored natural attenuation (MNA) is a promising, minimal invasive, and cost effective alternative for in-situ remediation of contaminated sites (e.g., Wiedemeier et al., 1999; US-EPA, 1999; Röling et al., 2001; Scow and Hicks, 2005; LABO, 2009). According to the US Environmental Protection Agency (EPA), natural attenuation refers to "the reliance on natural attenuation processes to achieve site-specific remediation objectives within a time frame that is reasonable compared to that offered by more active methods" (US-EPA, 1999). In general, the term natural attenuation can refer to a variety of naturally occurring physical (e.g., sorption, dilution, volatilization), chemical, and biological processes that lead to a reduction in contaminant mass, toxicity, mobility or concentration without human intervention (US-EPA, 1999; Wiedemeier et al., 1999).

Among the processes that contribute to the natural attenuation potential, those which lead to an irreversible reduction in contaminant mass are the most desirable ones. Considering organic contaminants such as petroleum hydrocarbons (e.g., BTEX, PAH) and chlorinated solvents, biodegradation, i.e. the break down and/or transformation of organic contaminants by intrinsic microorganisms, is the dominant process leading to a

natural reduction in contaminant mass (e.g. Wiedemeier et al., 1999; Meckenstock et al., 2004). A crucial step on the way to adopt MNA as adequate means of contaminated site management, is to show that contaminant degradation by intrinsic microorganisms is actually occurring at the site of interest (Smets and Pritchard, 2003). Furthermore, continuous monitoring is necessary to evaluate the performance of contaminant removal due to intrinsic biodegradation and to check if the remediation goals are achieved (US-EPA, 1999; LABO, 2009).

Monitoring of contaminant concentrations alone is not sufficient to proof the occurrence of biodegradation, since a reduction in concentration might also be caused by non destructive processes, such as dilution (US-EPA, 1999; LABO, 2009). Among other methods, such as monitoring of geochemical parameters (e.g., electron acceptor concentrations), metabolite analysis or microbiological methods (e.g., detection of functional genes), compound-specific isotope analysis (CSIA) has emerged as a valuable tool for the assessment of in-situ biodegradation (e.g., Schmidt et al., 2004; Meckenstock et al., 2004; Scow and Hicks, 2005; Elsner et al., 2005; Hofstetter et al., 2008; US-EPA, 2008; Bombach et al., 2010; Braeckevelt et al., 2012).

If naturally occurring degradation of organic contaminants by intrinsic microorganisms is not sufficient to meet the remediation goals at a certain site, biodegradation might be stimulated/enhanced by the addition of electron acceptors, electron donors, nutrients, and/or specific contaminant degraders (e.g. US-EPA, 2006; Cunningham et al., 2001; Scow and Hicks, 2005).

A number of studies has pointed out that, besides the actual microbially catalyzed degradation process, also physical mass-transfer processes, such as diffusion/dispersion, sorption or NAPL dissolution, might limit the potential for contaminant mass removal by in-situ biodegradation at contaminated field sites (e.g. Sturman et al., 1995; Ghoshal et al., 1996; Bosma et al., 1997; Brusseau et al., 1999; Prommer et al., 2006; Anneser et al., 2008). In order to identify the bottlenecks of in-situ biodegradation, a thorough understanding of the coupled biological and physical processes, acting on the contaminant of interest, is necessary. While the complexity and inaccessibility of groundwater systems, however, make it difficult to gain detailed processes understanding by groundwater monitoring at contaminated sites alone, reactive-transport modeling (e.g., Schäfer et al., 1998; Schirmer et al., 2000; Mayer et al., 2001; Maier and Grathwohl, 2006; Prommer et al., 2006, 2009) as well as flow-through experiments under well controlled conditions (e.g., von Gunten and Zobrist, 1993; Hunkeler et al., 1998; Huang et al., 2003; Rees et al., 2007; Bauer et al., 2008; Herzyk et al., 2014) have proven to

be valuable tools for the delineation of the individual effects of coupled physical and biological processes on in-situ biodegradation.

1.2 Background information

This study deals with the degradation of organic contaminants by chemoheterotrophic bacteria, which gain energy by catalyzing redox reactions of the type:

$$C_7H_8 + 9O_2 \rightarrow 7CO_2 + 4H_2O, \tag{1.1}$$

where the organic contaminant (here toluene C_7H_8) serves as electron donor and is mineralized/oxidized to carbon dioxide, and a dissolved compound (e.g., O_2, NO_3^-, SO_4^{2-}) serves as terminal electron acceptor.

A specifically important group of organic groundwater contaminants are the mono-aromatic BTEX-hydrocarbons: benzene, toluene, ethylbenzene, and xylenes, which present a significant health risk due to their relatively high solubility and toxicity (Chakraborty and Coates, 2004). BTEX-hydrocarbons are constituents of petroleum fuels and precursors for various petrochemical products. They are among the most important groundwater contaminants in Germany, and have entered the subsurface mainly by improper storage and/or transport of fuels such as gasoline and diesel. Fuel-hydrocarbon NAPLs are less dense than water and tend to form a thin, pancake like layer, which acts as a continuous source of dissolved BTEX-hydrocarbons, once they reach the groundwater water table (Wiedemeier et al., 1999).

Even though aromatic compounds are abundant in nature, e.g. in form of the structural aromatic polymer lignin, plants and animals have limited capacity for metabolizing them and degradation of aromatics is dominated by microorganisms (Fuchs et al., 2011). Due to the limited chemical reactivity arising from the aromaticity, the BTEX-hydrocarbons were long thought to be only biodegradable under aerobic conditions, where oxygen does not only serve as terminal electron acceptor but also as co-substrate for the activation of the aromatic structure for oxidative ring cleavage by oxygenase enzymes (e.g. Fuchs et al., 2011; Díaz et al., 2013). In the last decades, however, it was shown that the BTEX-hydrocarbons can also be degraded in the absence of oxygen, by reductive ring cleavage (e.g. Lovely, 2001; Chakraborty and Coates, 2004; Fuchs et al., 2011).

The ability of microorganisms to degrade aromatic compounds under anaerobic conditions is of special importance for contaminated aquifers, where oxygen, owing to its low solubility and rapid consumption by abiotic and biotic reactions, is often only present in trace amounts. Based on concentration measurements of electron acceptors for BTEX-degradation, Wiedemeier et al. (1999) estimated the relative importance of aerobic BTEX-degradation for 38 BTEX-contaminated sites to be as small as 3%, whereas sulfate reduction was estimated to be the dominant electron accepting process, accounting for 70% of intrinsic biodegradation.

1.2.1 Fringe-controlled biodegradation

The continuous release of organic contaminants from a source zone will result in a plume of dissolved organic contaminants. Here, intrinsic biodegradation depending on the presence of dissolved electron acceptors such as oxygen, nitrate, or sulfate, was shown to be most pronounced at the plume fringe, the contact zone between contaminated and ambient groundwater (Thornton et al., 2001; Tuxen et al., 2006; Prommer et al., 2006; Takahata et al., 2006; Anneser et al., 2008; Prommer et al., 2009). Due to continuous contaminant release and ongoing microbial activity, the plume core becomes depleted in dissolved electron acceptors over time. Microbial activity is then focused in the narrow mixing zone along the plume fringe (Anneser et al., 2010), where transverse dispersion mixes contaminated water and ambient groundwater carrying 'fresh' dissolved electron acceptors.

Figure 1.1 shows vertical profiles of toluene, sulfate and sulfide concentration, measured by a multilevel sampling well with a spatial resolution up to 2.5 *cm* across a BTEX plume at a former gasworks site (Anneser et al., 2007; Anneser, 2008). The toluene plume has a vertical extension of less than one meter and could only be captured due to the high spatial resolution of the multilevel sampling well. The profiles indicate steep vertical gradients in toluene, sulfate (predominant electron acceptor at the site) and sulfide concentrations at the plume fringe. Sulfate is completely depleted in the plume center and the reaction product sulfide is enriched at the plume fringe.

Under steady-state conditions, the only process causing mixing of contaminated water and ambient groundwater, carrying fresh electron acceptors, is transverse dispersion (Cirpka et al., 1999b), which is governed to a large extent by molecular diffusion. Due to the slow nature of molecular diffusion in the aqueous phase, theoretical and numerical

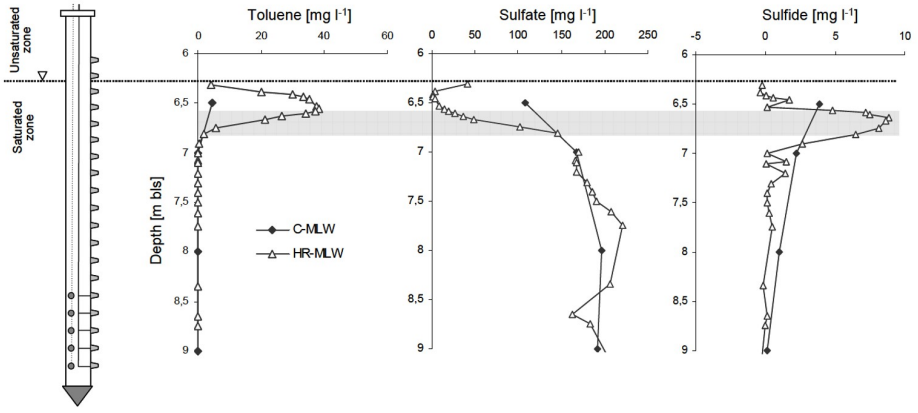

Figure 1.1: *Vertical profiles of toluene, sulfate (electron acceptor) and dissolved sulfide (reaction product) concentrations across a BTEX plume at a former gasworks site. The gray area indicates the lower plume fringe. Measurements were taken by a high-resolution multilevel well (HR-MLW; white triangles) and a conventional multilevel well (C-MLW; black diamonds). The Figure is taken from Anneser et al. (2007).*

studies suggested that the overall rate of contaminant removal in steady-state contaminant plumes might be controlled by transverse dispersion rather than actual biodegradation kinetics (e.g., Cirpka et al., 1999b; Chu et al., 2005; Maier and Grathwohl, 2006). Recent laboratory-scale experiments and model based analysis confirmed this finding for biodegradation under aerobic as well as denitrifying conditions, and showed that microbial activity in these mixing-controlled systems is indeed most pronounced in the narrow mixing zone along the plume fringe (Thullner et al., 2002; Huang et al., 2003; Rees et al., 2007; Bauer et al., 2008, 2009a).

Transverse mixing, and thus mixing-controlled biodegradation, was shown to be enhanced by aquifer heterogeneity (e.g., Werth et al., 2006; Rolle et al., 2009; Bauer et al., 2009a). In heterogeneous media, water flow is focused in high-permeability zones, which reduces both the transverse dispersion lengths and the time for mixing and reactions to take place. Werth et al. (2006) showed that the first effect outweighs the second one, and that mixing-controlled biodegradation is enhanced if the plume fringe is focused in a high-permeability zone.

1.2.2 Assessment of biodegradation by compound-specific isotope analysis

Compound-specific isotope analysis (CSIA) of organic contaminants (e.g. BTEX, chlorinated ethenes) has been identified as a powerful tool in studying fate and behavior of contaminants in groundwater systems (e.g. Meckenstock et al., 2004; Schmidt et al., 2004; Elsner et al., 2005; Hofstetter et al., 2008; US-EPA, 2008) and has been increasingly applied at contaminated field sites (e.g. Sherwood Lollar et al., 2001; Peter et al., 2004; Fischer et al., 2007; Pooley et al., 2009). Reaction-induced isotope fractionation during microbial degradation of organic contaminants generally leads to the enrichment of isotopically heavy molecules in the remaining contaminant fraction (Elsner et al., 2005), which can potentially serve as a proxy for biodegradation.

The standard approach is to analyze the carbon (^{12}C and ^{13}C) isotope composition of the contaminant. The bulk enrichment of ^{13}C for a given compound can be determined by gas chromatography-isotope ratio mass spectrometry (GC-IRMS) (e.g., Schmidt et al., 2004; Elsner et al., 2005). Observed $^{13}C/^{13}C$-ratios are conventionally reported as relative difference with respect to the international reference standard 'Pee Dee Belemnite' in the $\delta^{13}C$-notation:

$$\delta^{13}C = \frac{^{13}C/^{12}C - \left(^{13}C/^{12}C\right)_{ref}}{\left(^{13}C/^{12}C\right)_{ref}}. \tag{1.2}$$

A major challenge on the way to the implementation of monitored natural attenuation as means of contaminated site management is to proof that in-situ biodegradation is occurring. While a decrease in contaminant concentration might be caused by either biodegradation or dilution, isotope ratios, by contrast, are not affected by dilution and observed isotope enrichment at a contaminated site might be used as indicator for the occurrence of biodegradation.

In the limit that only biodegradation affects the isotope signal, the degree of isotope enrichment, i.e. enrichment of ^{13}C in the remaining contaminant fraction, can even serve as a measure for the extent of biodegradation. This is commonly done by applying the Rayleigh equation, which relates the reaction-induced isotope shift to the remaining contaminant fraction. For carbon isotopes at natural abundance the Rayleigh equation can be written as:

$$\frac{R_t}{R_0} = f_t^{(\alpha_r^{kin}-1)}, \tag{1.3}$$

in which R_t [-] is the ratio of heavy (^{13}C) over light (^{12}C) carbon isotopes at time t [T], R_0 is the original isotope ratio, f_t [-] is the remaining contaminant fraction at time t and α_r^{kin} [-] is the bulk kinetic isotope fractionation factor for biodegradation. The Rayleigh equation postulates a power-law dependence of the isotope ratio on the remaining fraction of the contaminant. If the Rayleigh equation holds, the measured values follow a straight line with a constant slope $(\alpha_r^{kin} - 1)$ in a double logarithmic plot of the isotope ratio vs. the remaining contaminant fraction, which was shown by numerous batch experiments (e.g. Meckenstock et al., 2004; Elsner et al., 2005, and references cited herein).

The Rayleigh equation is based on several underlying assumptions such as: the (bio)-chemical transformation is the only fractionating process, it is irreversible and represents the rate-limiting step; the reaction product does not further interact with the reactant; the reaction takes place in a well-mixed closed system and the pseudo-first order rate coefficients of the heavy and light isotopologues are in a constant ratio that does not depend on the concentration. If one or more of these assumptions are violated, the Rayleigh equation is no more strictly valid.

Several studies have pointed out the limitations of the Rayleigh equation when applied to groundwater systems (e.g., Abe and Hunkeler, 2006; Green et al., 2010; Thullner et al., 2012) and proposed methodologies to extend its validity to open systems (e.g., Mak et al., 2006; van Breukelen, 2007; Fischer et al., 2007) or alternative approaches to describe isotope fractionation in the presence of complex reaction networks (e.g., van Breukelen et al., 2005). An extensive review on short-comings of the Rayleigh approach to quantify biodegradation in groundwater systems is given by Thullner et al. (2012).

Isotope fractionation by physical processes

Recent experimental studies have shown that, besides (bio)chemical reactions, also physical mass-transfer processes can significantly affect the isotopic composition of organic contaminants in groundwater systems. Mass-transfer processes were shown to affect the isotope signal in two ways: (1) the extend of isotope fractionation is decreased if not the reaction itself, but transport of the contaminant to the reactive site, is limiting the overall rate of contaminant removal; (2) it may be increased if the physical transport step is fractionating between heavy and light isotopes in addition to biodegradation.

Kopinke et al. (2005) showed that sorption of organic contaminants to humic compounds can lead to significant isotope fractionation. Thullner et al. (2008) and Kampara et al. (2008) studied the effect of bioavailability restrictions on the observed isotope fractionation associated with biodegradation and came to the conclusion that limited bioavailability reduces isotope fractionation upon biodegradation. Bouchard et al. (2008) observed *C*-isotope fractionation due to gas-phase diffusion of petroleum hydrocarbons. Aeppli et al. (2009) showed that the limitation of biodegradation by inter-phase mass transfer may mask isotope fractionation. Rolle et al. (2010) found that transverse dispersion significantly fractionates between labeled and non-labeled ethylbenzene in two-dimensional flow-through microcosm experiments. Jin et al. (2014) observed *Cl*-isotope fractionation due to aqueous-phase diffusion of PCE and TCE

Isotopes and reactive-transport modeling

In contrast to simple analytical tools like the Rayleigh equation, reactive-transport models can account for the complex interaction of physical and microbial processes during contaminant transport in the subsurface. They have been proven as a useful tool in the interpretation of complex isotope patterns, resulting from the combined effects of microbial and physical processes on the isotope signal of organic contaminants (Rolle et al., 2010; Bouchard et al., 2008; van Breukelen and Prommer, 2008; Prommer et al., 2009; Thullner et al., 2012; van Breukelen and Rolle, 2012).

By means of reactive-transport modeling, Bouchard et al. (2008) quantified the combined effect of biodegradation and gas-phase diffusion on the measured isotope signal of petroleum hydrocarbons in the unsaturated zone, LaBolle et al. (2008) pointed out that diffusive exchange of contaminants between high and low permeability zones can lead to similar isotope ratio patterns as biodegradation does, Prommer et al. (2009) interpreted biogeochemical and isotopic gradients observed across a contaminant plume of various aromatic hydrocarbons, whereas Rolle et al. (2010) as well as van Breukelen and Rolle (2012) separated the effects of reaction- and transverse-dispersion-induced isotope fractionation on observed $\delta^{13}C$-patterns in mixing-controlled biodegradation.

While reactive transport modeling is highly useful for the interpretation of complex isotope signals, the availability of isotope data has also been able to give important, new constraints for the calibration of complex reactive transport models providing the key to an improved process understanding (e.g., Atteia et al., 2008; D'Affonseca et al., 2011; Prommer et al., 2008), which would not be obtained from concentration data

alone. Specifically, the additional experimental observable provides the opportunity to test additional model parameters reflecting additional processes.

1.3 Objectives and structure of the thesis

In this thesis I apply reactive-transport modeling to delineate the effects of coupled physical and biological processes on organic contaminants in groundwater systems. To this end, I performed scenario simulations, and analyzed laboratory-scale flow-through experiments at different scales. The thesis is divided into two main parts.

The focus of the first part, which comprises chapters 3 and 4, lies on the coupled effect of biodegradation, transverse dispersion and sorption on the stable-carbon isotope signature of BTEX-hydrocarbons, in steady-state as well as transient contaminant plumes. Special emphasize is put on possible implications for the assessment of in-situ biodegradation by compound specific isotope analysis (CSIA).

- **Chapter 3** - Isotope fractionation in steady-state contaminant plumes:

  The focus of the parameter study presented in chapter 3 lies on the effect of transverse dispersion, if acting as degradation-rate limiting step, on observed isotope signals, which has not been addressed in previous studies on the coupled effect of transverse dispersion and biodegradation on isotope fractionation (Rolle et al., 2010; van Breukelen and Rolle, 2012). Furthermore, the effect of depth-integrated sampling by fully-screened monitoring wells, on the interpretation of spatial isotope enrichment patterns in fringe-controlled biodegradation, is assessed.

- **Chapter 4** - Isotope fractionation in a toluene-pulse experiment:

  Kopinke et al. (2005) and Hoehener and Yu (2012) have shown that sorption of hydrophobic organic contaminants can cause isotope fractionation. This chapter addresses the coupled effect of sorption, transverse dispersion, and biodegradation on the stable-carbon isotope signature of toluene, in a pulse experiment under field-like conditions. The effect of individual processes on overall isotope fractionation is quantified by reactive-transport modeling, the model complexity needed to adequately describe the system is identified, and the value of isotope data for model calibration is assessed.

The second part (chapters 5, 6 and 7) addresses the influence of transient plume conditions, e.g., spatial plume relocation due to changing hydraulic conditions, on in-situ biodegradation.

- **Chapter 5** - Fringe-controlled biodegradation under dynamic conditions:

  While fringe-controlled biodegradation has been extensively studied for steady-state contaminant plumes (e.g., Prommer et al., 2006; Cirpka and Valocchi, 2007; Anneser et al., 2008; Bauer et al., 2008), so far little is known on the effects of dynamic plume conditions, which might arise due to changing hydraulics. In this chapter, laboratory-scale flow-through experiments are analyzed by reactive-transport modeling to assess the effect of the spatial relocation of a toluene plume on fringe-controlled biodegradation. Special emphasize is put on the behavior of the toluene-degrading bacteria during periods of toluene(substrate)-starvation.

- **Chapter 6** - Effect of heterogeneity on biodegradation in dynamic plumes:

  Aquifer heterogeneity has been shown to increase the rate of biodegradation, if it is controlled by transverse mixing of 'fresh' electron acceptors from the ambient groundwater into the plume (e.g., Werth et al., 2006; Bauer et al., 2009a). This chapter addresses the effect of aquifer heterogeneity on biodegradation in dynamic contaminant plumes. If the plume fringe is focused in the same high-conductivity zone before and after a shift in plume position, the effect of plume dynamics on biodegradation might also be reduced.

- **Chapter 7** - Microbial dynamics in flow-through systems:

  While biodegradation at the plume fringe is mainly controlled by physical mixing in steady-state plumes (e.g., Cirpka et al., 1999b; Bauer et al., 2008), microbial processes such as growth, decay, and attachment/detachment might become important under dynamic conditions. Multiple column experiments were analyzed by reactive-transport modeling to study the coupling between microbial growth, decay and transport in porous media, as well as the ability of bacteria to cope with periods of substrate starvation.

Chapter 2

Methods

2.1 Governing equations

2.1.1 Groundwater flow and conservative transport

As basis for the reactive-transport simulations, I consider two-dimensional steady-state flow fields in fully water-saturated porous media under confined conditions. Fixed-head boundary conditions are applied to the in- and outflow-boundary of the two-dimensional domain whereas the remaining two boundaries are assumed to be impermeable. Hydraulic conductivity is considered to be isotropic but spatially variable. Under the above mentioned conditions the spatial distributions of hydraulic head h $[L]$ and stream function value ψ $[L^2T^{-1}]$ are given by:

$$-\nabla \cdot (K\nabla h) = 0 \tag{2.1}$$

$$-\nabla \cdot (\frac{1}{K}\nabla \psi) = 0, \tag{2.2}$$

with the hydraulic conductivity K $[LT^{-1}]$. The specific discharge vector $\mathbf{q}$ $[LT^{-1}]$ at each point in the domain is given by Darcy's law:

$$\mathbf{q} = -K\nabla h. \tag{2.3}$$

In the case of isotropic hydraulic conductivity, the isopotential lines of hydraulic head ϕ and stream-function value ψ are perpendicular to each other, which is used later on for the construction of streamline-oriented transport grids.

Conservative transport of a dissolved compound can be described by the advection-dispersion equation:

$$\frac{\partial c}{\partial t} + \nabla \cdot (\mathbf{v}c) - \nabla \cdot (\mathbf{D}\nabla c) = 0, \tag{2.4}$$

in which c $[ML^{-3}]$ is the concentration of the compound, $\mathbf{v}$ $[LT^{-1}]$ is the seepage velocity, given by the ratio of the specific discharge q and the flow effective porosity n $[-]$ and $\mathbf{D}$ $[L^2T^{-1}]$ is the local dispersion tensor.
The longitudinal component of $\mathbf{D}$ is parameterized using the standard linear model (Scheidegger, 1961):

$$D_l = \frac{D_{aq}}{\tau} + v\alpha_L, \tag{2.5}$$

where D_{aq} $[L^2T^{-1}]$ is the aqueous diffusion coefficient, τ $[-]$ is the tortuosity, which is usually approximated by $1/n$, and α_L $[L]$ is the longitudinal dispersivity. The transverse component of $\mathbf{D}$ is parameterized by a non-linear model recently proposed by Chiogna et al. (2010). The latter parameterization shows compound dependence of transverse dispersion not only in the pore diffusion term D_{aq}/τ but also in the mechanical dispersion term:

$$D_t = \frac{D_{aq}}{\tau} + v\frac{d}{\sqrt{\frac{vd}{D_{aq}} + 123}}, \tag{2.6}$$

in which d $[L]$ is the median grain size of the porous medium.

2.1.2 Reactive transport

Standard bioreactive-transport model

Transport of oxidizable organic contaminants (electron donors) in porous media coupled to microbially-mediated degradation and consumption of dissolved electron acceptors can be mathematically described by a system of advection-dispersion-reaction equations:

$$\frac{\partial c_{sub}}{\partial t} = -\mathbf{v}\nabla c_{sub} + \nabla \cdot (\mathbf{D_{sub}}\nabla c_{sub}) - r_{sub} \tag{2.7}$$

$$\frac{\partial c_{ea}}{\partial t} = -\mathbf{v}\nabla c_{ea} + \nabla \cdot (\mathbf{D_{ea}}\nabla c_{ea}) - r_{ea}, \tag{2.8}$$

in which c_{sub} and c_{ea} [ML^{-3}] are the concentrations of the dissolved contaminant (substrate) and electron acceptor, respectively, r_{sub} [$\mathrm{ML}^{-3}\mathrm{T}^{-1}$] is the rate of the contaminant (substrate) oxidation, and r_{ea} [$\mathrm{ML}^{-3}\mathrm{T}^{-1}$] is the rate of electron-acceptor consumption.

The rate of contaminant degradation due to microbially catalyzed oxidation can be described by Michaelis-Menten kinetics:

$$r_{sub} = r_{sub}^{max} \frac{c_{sub}}{c_{sub} + K_{sub}}, \tag{2.9}$$

with the maximum degradation rate r_{sub}^{max} [$ML^{-3}T^{-1}$] and the half-saturation concentration (Michaelis-Menten coefficient) of the contaminant K_{sub} [ML^{-3}].

The Michaelis-Menten kinetic expression was originally developed for single enzyme kinetics but is frequently applied to describe contaminant degradation by microorganisms. It approaches a zero-order reaction rate law with the maximum degradation rate r_{sub}^{max} at high substrate concentrations ($c_{sub} >> K_{sub}$) and first order kinetics, with the first order rate coefficient r_{sub}^{max}/K_{sub}, at low substrate concentration ($c_{sub} << K_{sub}$).

Considering the dependence of contaminant degradation on the presence of an electron acceptor, the reaction rate law can be extended to dual Michaelis-Menten kinetics:

$$r_{sub} = r_{sub}^{max} \frac{c_{sub}}{c_{sub} + K_{sub}} \frac{c_{ea}}{c_{ea} + K_{ea}} \tag{2.10}$$

$$r_{ea} = f_{ea} r_{sub}^{max} \frac{c_{sub}}{c_{sub} + K_{sub}} \frac{c_{ea}}{c_{ea} + K_{ea}}, \tag{2.11}$$

with the half saturation concentration of the electron acceptor K_{ea} [ML^{-3}], the rate of electron acceptor consumption r_{ea} [$ML^{-3}T^{-1}$] and the stoichiometric coefficient f_{ea} [$-$] for electron acceptor consumption due to contaminant degradation.

Model assumptions

Reactive transport is simulated on the continuum (Darcy) scale. This implies that only volume averages of concentration are considered and concentration gradients that might

occur on the pore scale (e.g. Meile and Tuncay, 2006; Rolle et al., 2012) are not explicitly accounted for in the model. As done in most standard reactive-transport models (e.g. Barry et al., 2002; Cirpka and Valocchi, 2007; Prommer et al., 2006, 2009), the biomass is considered as immobile species, which can be justified by the fact that the vast majority of microorganisms in natural aquifers was found to live attached to the sediment surface (e.g. Hazen et al., 1991; Griebler et al., 2002; Anneser et al., 2010). Furthermore, the model is based on the simplifying assumptions that the microorganisms are equally distributed on the sediment surface and that electron donor/acceptor dissolved in the aqueous phase are readily available to the attached bacteria. While reduced substrate availability due to diffusive mass transfer on the pore scale to the cells, or diffusion-controlled uptake by the cells may result in a reduced macroscopic (continuum scale) degradation rate (e.g., Dykaar and Kitanidis, 1996; Knutson et al., 2007; Hesse et al., 2009), these effects are neglected in the present studies.

Microbial growth and decay

Considering growth of attached bacteria X_{att} [MM^{-1}] due to contaminant degradation, we have to add an ordinary differential equation describing the temporal evolution of bacterial concentration to the governing reactive-transport equations:

$$\frac{\partial X_{att}}{\partial t} = r_{gr} - r_{dec}, \tag{2.12}$$

where r_{gr} [$\mathrm{MM}^{-1}\mathrm{T}^{-1}$] is the microbial growth rate, and r_{dec} [$\mathrm{MM}^{-1}\mathrm{T}^{-1}$] is the biomass 'decay' rate.

Accounting for the dependence of microbial growth on the simultaneous presence of substrate (electron donor and carbon source) and electron acceptor, we can describe the growth rate r_{gr} by the empirical dual Monod growth rate law :

$$r_{gr} = \mu_{max} \frac{c_{sub}}{c_{sub} + K_{sub}} \frac{c_{ea}}{c_{ea} + K_{ea}} X_{att}, \tag{2.13}$$

where μ_{max} [T^{-1}] is the maximum specific growth rate, and K_{sub} and K_{ea} [ML^{-3}] are the half-saturation concentrations (Monod coefficients) of the substrate and the electron acceptor, respectively.

Equation 2.13 considers the concentrations of the electron acceptor and donor to be the only growth limiting factors. It does not account for other factors that might limit microbial growth, such as the availability of nutrients or diffusion-controlled transport

of solutes to the bacteria, which are attached to the sediment surface. As done frequently in reactive-transport modeling I account for additional growth limiting factors by the introduction of a maximum capacity X_{att}^{max} for attached bacteria (e.g., Zysset et al., 1994; Schirmer et al., 2000; Rolle et al., 2010):

$$r_{gr} = \mu_{max} \frac{c_{sub}}{c_{sub} + K_{sub}} \frac{c_{ea}}{c_{ea} + K_{ea}} X_{att} \left(1 - \frac{X_{att}}{X_{att}^{max}}\right). \tag{2.14}$$

The major drawback of this approach is that X_{att}^{max} is a purely empirical fitting factor and so far it can not be determined a priori.

The rates of substrate degradation r_{sub} $[ML^{-3}T^{-1}]$ and electron acceptor consumption r_{ea} $[ML^{-3}T^{-1}]$ can be related to the microbial growth rate by:

$$r_{sub} = -\frac{(1-n)\rho_s}{n} \frac{1}{Y} r_{gr} \tag{2.15}$$

$$r_{ea} = -\frac{(1-n)\rho_s}{n} \frac{f_{gr}}{Y} r_{gr}, \tag{2.16}$$

in which Y $[MM^{-1}]$ is the growth yield, relating the synthesis of new biomass to substrate consumption, f_{gr} $[-]$ is the stoichiometric coefficient for electron acceptor consumption due to microbial growth, and $(1-n)/n\rho_s$ $[\mathrm{M}^{-1}\mathrm{L}^{-3}]$ is the ratio of mass of solids to water volume in the porous medium with n [-] denoting porosity and ρ_s $[\mathrm{ML}^{-3}]$ the mass density of the solids. When bacteria use a contaminant as electron donor and carbon source, they transfer a fraction of the electrons to a terminal electron acceptor to gain energy, while the other fraction is used to build up new biomass (Rittmann and McCarty, 2001). The partial incorporation of reduced carbon from the substrate into new biomass leads to smaller values for f_{gr} than expected for complete mineralization.

A non-mechanistic lumped decay term of the form:

$$r_{dec} = k_{dec} X_{att}, \tag{2.17}$$

with a first order decay coefficient k_{dec} $[\mathrm{T}^{-1}]$, is applied in standard reactive transport models to account for any kind of biomass loss over time (e.g., Barry et al., 2002; Cirpka and Valocchi, 2007; Prommer et al., 2009).

Microbial transport

While microbial transport is neglected in most reactive-transport models in contaminant

hydrology, it is a crucial factor in groundwater transport of pathogens or bioaugmentation to enhance intrinsic biodegradation and has therefore been studied extensively (e.g., Clement et al., 1997; Murphy and Ginn, 2000; Ginn et al., 2002; Tufenkji, 2007). Transport of suspended bacteria X_{mob} can be described by an advection-dispersion equation, considering attachment to and detachment from the soil matrix:

$$\frac{\partial X_{mob}}{\partial t} = -\mathbf{v}\nabla X_{mob} + \nabla \cdot (\mathbf{D_X}\nabla X_{mob}) - r_{att} + \frac{(1-n)\rho_s}{n} r_{det} \tag{2.18}$$

$$\frac{\partial X_{att}}{\partial t} = +\frac{n}{(1-n)\rho_s} r_{att} - r_{det}, \tag{2.19}$$

where r_{att} $[ML^{-3}T^{-1}]$ and r_{det} $[MM^{-1}T^{-1}]$ are the rates of attachment/detachment for mobile and attached microorganisms, respectively. The rates of microbial attachment r_{att} and detachment r_{det} are commonly described by first-order rate laws:

$$r_{att} = k_{att} X_{mob} \tag{2.20}$$

$$r_{det} = k_{det} X_{mob}, \tag{2.21}$$

with the first-order attachment and detachment coefficients k_{att} and k_{det} $[T^{-1}]$ respectively. Commonly k_{att} is estimated based on colloid filtration theory (e.g., Harvey and Garabedian, 1991; Clement et al., 1997; Murphy and Ginn, 2000; Ginn et al., 2002), which predicts a linear dependence of k_{att} on the flow velocity:

$$k_{att} = \frac{3(1-n)q\eta\alpha}{2d}, \tag{2.22}$$

in which n is the porosity, q is the specific discharge, d is the average grain diameter, η is the collector efficiency and α is the sticking efficiency. While η can be estimated a priori based on colloid filtration theory, α is a fitting factor. This approach to describe bacterial attachment accounts only for attachment of bacteria due to physical filtration and does not consider any active attachment processes of bacteria.

Sorption

Sorption of the contaminant to soil organic mater leads to an additional storage capacity for the contaminant per volume porous media. Provided that sorption is locally in equilibrium, it can be accounted for by the introduction of the retardation factor R $[-]$ into equation 2.7:

$$R\frac{\partial c_{sub}}{\partial t} = -\nabla \cdot (\mathbf{v} c_{sub}) + \nabla \cdot (\mathbf{D_{sub}} \nabla c_{sub}) - r_{sub}, \tag{2.23}$$

in which the retardation factor R is given by:

$$R = 1 + \frac{1-n}{n} \rho_s \frac{\partial c^s_{sub}}{\partial c_{sub}}, \tag{2.24}$$

with the concentration of sorbed contaminant c^s_{sub} $[MM^{-1}]$. For the case of linear sorption, which is considered in this study, $\frac{\partial c^s_{sub}}{\partial c_{sub}}$ is given by the constant soil water partitioning K_d $[L^3M^{-1}]$.

2.1.3 Isotope fractionation

Carbon-isotope fractionation due to biodegradation of organic contaminants is implemented in the reactive-transport model by considering the two most abundant isotopologues ${}^{12}c_{sub}$ (molecule contains only light carbon isotopes) and ${}^{13}c_{sub}$ (one light carbon isotope is substituted by a heavy one) as separate species. Due to the low natural abundance of ${}^{13}C$, cases with two or more ${}^{13}C$ inside a single molecule can be neglected and fractionation by Monod kinetics can be described by a constant fractionation factor, in the same way as for first order reactions. Further, an operational "bulk" isotope fractionation factor can be defined (Elsner et al., 2005) reflecting the average behavior of the different ${}^{13}c_{sub}$ isotopomers (i.e., molecules with the heavy isotope in different molecular positions) so that a more complicated treatment as done, e.g., in Maggi and Riley (2010) and Jin et al. (2013) is not necessary and also prior knowledge of the reaction mechanism is not required (Elsner et al., 2005).

Degradation rates for the light (${}^{12}c_{sub}$) and heavy (${}^{13}c_{sub}$) isotopologues under growth conditions, considering competitive enzyme inhibition, are given by:

$${}^{12}r_{sub} = -{}^{12}k_{max} X \frac{{}^{12}c_{sub}}{{}^{12}K_{sub}\left(1 + {}^{12}c_{sub}/{}^{12}K_{sub} + {}^{13}c_{sub}/{}^{13}K_{sub}\right)} \frac{c_{ea}}{c_{ea} + K_{ea}} \tag{2.25}$$

$${}^{13}r_{sub} = -{}^{13}k_{max} X \frac{{}^{13}c_{sub}}{{}^{13}K_{sub}\left(1 + {}^{12}c_{sub}/{}^{12}K_{sub} + {}^{13}c_{sub}/{}^{13}K_{sub}\right)} \frac{c_{ea}}{c_{ea} + K_{ea}}, \tag{2.26}$$

in which the maximum specific degradation rate k_{max} $[T^{-1}]$ is given by the ratio of the maximum specific growth rate μ_{max} and the microbial growth yield Y. The kinetic bulk isotope fractionation factor for biodegradation following Monod kinetics α^{kin}_r is given

by the ratio of k_{max}/K_{tol} for ${}^{13}c_{sub}$ and ${}^{12}c_{sub}$ [19]:

$$\alpha_r^{kin} = \frac{{}^{13}r/{}^{13}c_{sub}}{{}^{12}r/{}^{12}c_{sub}} = \frac{{}^{13}k_{max}/{}^{13}K_{sub}}{{}^{12}k_{max}/{}^{12}K_{sub}}. \tag{2.27}$$

To derive the reaction rates for ${}^{12}c_{sub}$ and ${}^{13}c_{sub}$ from the overall degradation rate r_{sub}, the half saturation coefficient K_{sub} is assumed to be identical for both isotopologues, as done in previous studies (van Breukelen and Prommer, 2008; Rolle et al., 2010):

$${}^{12}r_{sub} = r_{sub}\frac{{}^{12}c_{sub}}{{}^{12}c_{sub} + {}^{13}c_{sub}} \tag{2.28}$$

$${}^{13}r_{sub} = r_{sub}\alpha_r^{kin}\frac{{}^{13}c_{sub}}{{}^{12}c_{sub} + {}^{13}c_{sub}}. \tag{2.29}$$

Recent laboratory and theoretical studies (Kopinke et al., 2005; Hoehener and Yu, 2012) suggest that sorption to organic matter is slightly stronger for the light isotopologues (${}^{12}K_d > {}^{13}K_d$), which leads to a faster breakthrough of the heavy isotopologues. This effect on the observed isotope signal is implemented in the reactive transport model by considering different retardation factors R for ${}^{12}c_{sub}$ and ${}^{13}c_{sub}$ (${}^{13}R < {}^{12}R$). Isotope fractionation due to equilibrium sorption can be described by the sorption-related equilibrium isotope fractionation factor α_s^{equ} $[-]$ (Kopinke et al., 2005):

$$\alpha_s^{equ} = \frac{{}^{13}R - 1}{{}^{12}R - 1} = \frac{{}^{13}K_d}{{}^{12}K_d}. \tag{2.30}$$

Also, transverse dispersion has been shown to affect the isotope signal of organic contaminants in recent laboratory and field studies (Rolle et al., 2010; van Breukelen and Rolle, 2012). The mass difference between ${}^{12}C$ and ${}^{13}C$ results in isotopologue-specific diffusion coefficients. Unlike longitudinal dispersion, which mainly depends on spatial velocity fluctuations due to subsurface heterogeneity, transverse dispersion is governed to a large extent by diffusion. Hence different diffusion properties of ${}^{12}c_{sub}$ and ${}^{13}c_{sub}$ directly result in different transverse dispersion coefficients of the different isotopologues. Isotope fractionation due to transverse dispersion can thus be described by the dispersion-related kinetic isotope fractionation factor α_D^{kin} $[-]$ (Elsner, 2010; Rolle et al., 2010):

$$\alpha_D^{kin} = \frac{{}^{13}D_t}{{}^{12}D_t}. \tag{2.31}$$

In this thesis, all isotope fractionation factors are reported as isotopic enrichment factors $\varepsilon = \alpha - 1$ in ‰.

Considering isotopologue-specific degradation rates, retardation factors and transverse

dispersion coefficients in the reactive transport model yields the following governing equations for the light ${}^{12}c_{sub}$ and heavy ${}^{13}c_{sub}$ contaminant isotopologues:

$$ {}^{12}R_{sub}\frac{\partial {}^{12}c_{sub}}{\partial t} = -\mathbf{v}\cdot\nabla {}^{12}c_{sub} + \nabla\cdot\left({}^{12}\mathbf{D_{sub}}\nabla {}^{12}c_{sub}\right) - {}^{12}r_{sub} \tag{2.32} $$

$$ {}^{13}R_{sub}\frac{\partial {}^{13}c_{sub}}{\partial t} = -\mathbf{v}\cdot\nabla {}^{13}c_{sub} + \nabla\cdot\left({}^{13}\mathbf{D_{sub}}\nabla {}^{13}c_{sub}\right) - {}^{13}r_{sub}. \tag{2.33} $$

Since we are interested in the enrichment of ${}^{13}C$ relative to a reference value rather than the absolute value of the isotope ratio ${}^{13}C/{}^{12}C$:

$$ \delta^{13}C = \frac{\left({}^{13}C/{}^{12}C\right) - \left({}^{13}C/{}^{12}C\right)_{ref}}{\left({}^{13}C/{}^{12}C\right)_{ref}}, \tag{2.34} $$

we can directly calculate $\delta^{13}C$ from the simulated ratio of heavy and light isotopologues ${}^{13}c_{sub}/{}^{12}c_{sub}$, without explicitly considering the actual abundance of ${}^{12}c_{sub}$ and ${}^{13}c_{sub}$, if we set the initial ratio of heavy and light isotopologues to $\left({}^{13}C/{}^{12}C\right)_{ref}$.

2.2 Numerical methods

2.2.1 Flow and conservative transport

Spatial discretization

The schemes for spatial discretization of the two-dimensional flow and transport equations applied in this thesis were developed by Cirpka (1997). The main principles are summarized in this section.

The two-dimensional steady-state groundwater flow equation for a confined system is spatially discretized by the Finite Element Method on a rectangular grid adopting bilinear quadrilateral elements. The resulting system of linear algebraic equations is solved with the UMFPACK solver implemented in Matlab (Davis and Duff, 1997).

The cell-centered finite volume method is adopted for spatial discretization of the two-dimensional transport equation. Streamline-oriented grids, with quadrilateral elements oriented into the direction of flow (see Fig. 2.2), are constructed as outlined in Cirpka

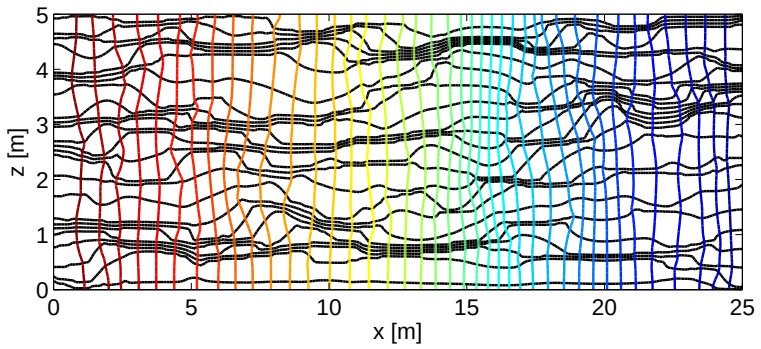

Figure 2.1: *Streamlines and isopotential lines of hydraulic head for flow in a two-dimensional heterogeneous domain. Streamlines (black lines) are focused in high conductivity zones.*

et al. (1999c). Along the flow direction, the domain is discretized by the isopotential lines of hydraulic head. Parallel to the flow direction, the domain is split into stream tubes of equal discharge Q_{tube} $[L^2T^{-1}]$. This leads to narrower elements in high velocity zones and wider ones in low velocity regions (see Fig. 2.2). Advection in each stream tube is one-dimensional and neighboring stream tubes solely interact by transverse dispersion. While a perfect streamline-oriented grid, which is discretized by streamlines and isopotential lines of hydraulic head, would yield curvilinear quadrilateral elements with orthogonal edges for isotropic conductivity fields, the elements for the construction of the finite volume grid are approximated by quadrilaterals (Cirpka et al., 1999a,c).

Aligning the grid with the flow direction restricts numerical diffusion arising from the approximation of advective fluxes to the longitudinal direction (Cirpka et al., 1999b) and reduces the dispersion tensor to a diagonal matrix. The accurate calculation of transverse dispersive fluxes is of special importance for the simulation of fringe-controlled biodegradation, in which the reaction rate is controlled by mixing of contaminant and electron acceptor due to transverse dispersion.

Advective fluxes between neighboring cells within each stream tube are approximated by upwind differentiation. Upwind differentiation combined with explicit Euler integration in time yields the exact solution for advective transport if the grid spacing Δx and time step size Δt are chosen to yield a Courant number ($Cr = v\Delta t/\Delta x$) of one. For

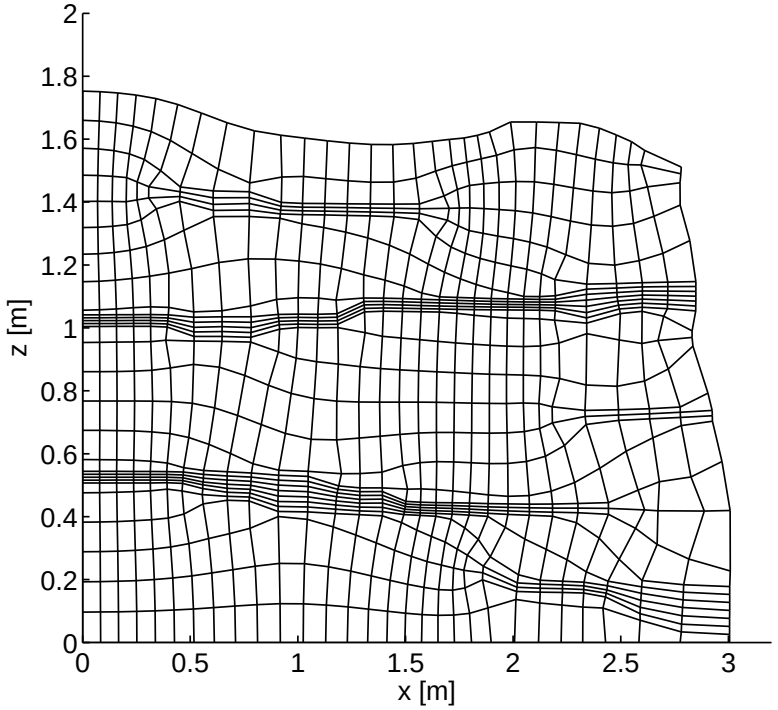

Figure 2.2: *Extract from the streamline-oriented grid with quadrilateral cells, which was constructed based on the flow field depicted in figure 2.1.*

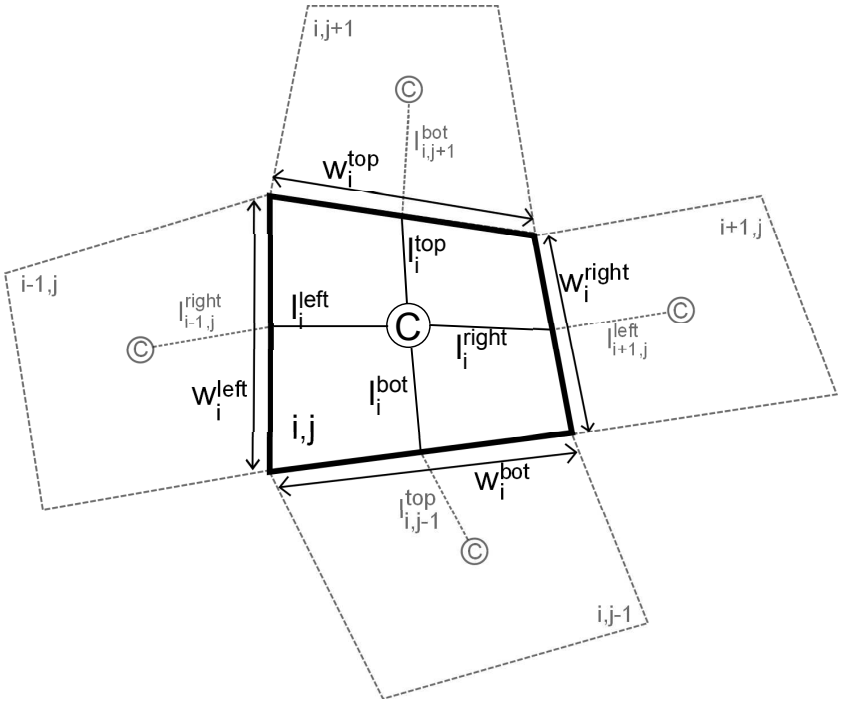

Figure 2.3: *Construction of fluxes between neighboring cells of the cell-centered finite volume grid.*

Courant numbers smaller than one, however, the upwind scheme causes numerical diffusion into the direction of flow and it is not stable for $Cr > 1$ if explicit integration in time is adopted, since only connections between neighboring cells are considered. For a detailed discussion of numerical schemes that are available for the solution of advection-dominated transport the reader is refered to Cirpka (1997).

The calculation of dispersive fluxes between adjacent cells requires the determination of spatial gradients and hence effective distances between adjacent cells. The distance between neighboring cells is calculated by connecting the center of gravity (C), which divides each cell into four parts of equal area, with the midpoint of the cell interface and the center of gravity of the adjacent cell. Following this procedure, the effective distance between cell i, j and cell $i+1, j$ is given by the sum of $l_{i,j}^{right}$ and $l_{i+1,j}^{left}$ (see Figure 2.3). Non-orthogonality of dispersive fluxes and element boundaries, that occurs due to the approximation of curvilinear elements by quadrilaterals is neglected and fluxes are assumed to be orthogonal to element boundaries.

The rate of change in compound mass for cell i, j due to advection (upwind differentiation) and dispersion is given by (Cirpka et al., 1999a):

$$\begin{aligned} nA_i \frac{\partial c_i}{\partial t} &= Q_{tube} \cdot c_{i-1,j} - Q_{tube} \cdot c_{i,j} \\ &= +nw_i^{left} D_l^{left} \frac{c_{i-1,j} - c_{i,j}}{l_{i-1,j}^{right} + l_{i,j}^{left}} - nw_i^{right} D_l^{right} \frac{c_{i,j} - c_{i+1,j}}{l_{i,j}^{right} + l_{i+1,j}^{left}} \\ &= -nw_i^{bot} D_t^{bot} \frac{c_{i,j} - c_{i,j-1}}{l_{i,j}^{bot} + l_{i,j-1}^{top}} - nw_i^{top} D_t^{top} \frac{c_{i,j} - c_{i,j+1}}{l_{i,j}^{top} + l_{i,j+1}^{bot}}. \end{aligned} \tag{2.35}$$

The longitudinal dispersion coefficients D_l^{left} and D_l^{right} are calculated with the specific discharge q at the left Q_{tube}/w_i^{left} and right Q_{tube}/w_i^{right} interface of element i, j. The specific discharge at the element interfaces parallel to the flow direction, which is needed for the calculation of the transverse dispersion coefficients D_t^{bot} and D_t^{top}, is approximated by the arithmetic mean of Q_{tube}/w_i^{left} and Q_{tube}/w_i^{right}. The longitudinal dispersivity α_l and the porosity n are assumed to be constant within the entire domain. The effective grain diameter d, which is needed for the calculation of D_t (see Eq. 2.6) is estimated for each cell, following the procedure outlined in Chiogna et al. (2011a), from the hydraulic conductivity by the empirical correlation of Hazen (1893):

$$d \approx \frac{\sqrt{K}}{100}. \tag{2.36}$$

The transverse dispersion coefficient at the cell interfaces is then calculated by the weighted harmonic mean of the D_t values for the two cells. For D_t at the interface between cell i, j and cell $i, j+1$ this leads to:

$$D_t^{(i,j)\to(i,j+1)} = \frac{l_{i,j}^{top} + l_{i,j+1}^{bot}}{l_{i,j}^{top}/D_t^{i,j} + l_{i,j+1}^{bot}/D_t^{i,j+1}}. \tag{2.37}$$

For transport simulations on heterogeneous conductivity fields, where a Courant number of one cannot be achieved for all cells of the finite volume grid, the Van Leer slope limiter (van Leer, 1973) is applied to reduce the amount of numerical diffusion which arises from the approximation of advective fluxes for cells with $Cr < 1$. The advective flux between cell i, j and cell $i+1, j$ is then calculated by:

$$F_{adv}^{(i,j)\to(i+1,j)} = Q_{tube}\left(c_{i,j} + s \cdot l_i^{right}\right), \tag{2.38}$$

with the slope s given by:

$$\begin{aligned} s &= 0 && \text{if} \quad s_{down} \cdot s_{up} < 0 \\ s &= \frac{2}{1/s_{up} + 1/s_{down}} && \text{if} \quad s_{down} \cdot s_{up} \geq 0, \end{aligned} \tag{2.39}$$

in which the concentration gradients between cell i, j and the upstream cell s_{up} and concentration gradient between cell i, j and the downstream cell s_{down} are given by:

$$s_{up} = \frac{c_{i-1,j} - c_{i,j}}{l_{i-1,j}^{right} + l_{i,j}^{left}} \tag{2.40}$$

$$s_{down} = \frac{c_{i,j} - c_{i+1,j}}{l_{i,j}^{right} + l_{i+1,j}^{left}}. \tag{2.41}$$

The implementation of van Leer's slope limiter scheme leads to advective fluxes entering and leaving cell i, j that depend non-linearly on the concentration in cell i, j.

Spatial discretization of the conservative-transport equation for the entire two-dimensional domain with upwind differentiation for the advection term, under consideration of a constant flux boundary condition for the inflow, results in the following system of linear oridnary differential equations:

$$\mathbf{M}_{store}\frac{\partial \mathbf{c}}{\partial t} + \mathbf{M}_{mob}\mathbf{c} = \mathbf{r}_{in}, \tag{2.42}$$

where $\mathbf{M}_{store}$ is the $n_{cells} \times n_{cells}$ storage matrix, containing the pore area of each cell along the main diagonal, $\mathbf{c}$ is the $n_{cells} \times 1$ vector of concentrations and, $\mathbf{M}_{mob}$ is the $n_{cells} \times n_{cells}$ mobility matrix, containing the transport connections between neighboring cells, and $\mathbf{r}_{in} = Q_{tube} \cdot \mathbf{c}_{in}$ is the vector of incoming mass flux.

Temporal discretization

Depending on the question of interest, temporal discretization of the transport equation is either performed by the implicit Euler Method, yielding the following system of linear algebraic equations for each time step:

$$\left(\mathbf{M}_{store} + \Delta t \mathbf{M}_{mob}\right) \mathbf{c}_{new} = \Delta t \mathbf{r}_{in} + \mathbf{M}_{store} \mathbf{c}_{old}, \tag{2.43}$$

or an operator splitting approach is adopted to separate the calculation of advective and dispersive transport. This way explicit Euler integration in time could be performed for advective transport:

$$\mathbf{c}_{new}^{adv} = \mathbf{c}_{old} + \Delta t \mathbf{M}_{store}^{-1} \left(\mathbf{r}_{in} - \mathbf{M}_{mob}^{adv} \mathbf{c}_{old}\right), \tag{2.44}$$

and implicit Euler integration for the dispersive fluxes:

$$\mathbf{c}_{new}^{disp} = \left(\mathbf{M}_{store} + \Delta t \mathbf{M}_{mob}^{disp}\right)^{-1} \mathbf{M}_{store} \mathbf{c}_{new}^{adv}. \tag{2.45}$$

The separation of advective and dispersive fluxes is chosen for transient simulations in homogeneous conductivity fields (chapter 4), for which the streamline-oriented grid converges to a regular grid, a Courant number of one can be achieved for all cells and explicit Euler integration in time of the advection term combined with upwind differentiation yields the exact solution. Depending on the velocity and cell length, however, rather small time steps have to be chosen in order to meet the Courant criterion, which might be computationally time consuming for long-time simulations.

While Δt is fixed for the whole simulation time in the explicit scheme, it can be adapted during the simulation if implict Euler integration in time is applied. This is beneficial for simulations with long phases of stable conditions, where larger time steps can be chosen (see chapter 5). Applying implicit integration in time, however, introduces additional numerical diffusion that scales linearly with the time step size.

For heterogeneous conductivity fields, the Courant criterion cannot be satisfied for all cells and upwind differentiation causes numerical diffusion which can be reduced by the implementation of van Leer's slope limiter scheme. While the implementation is straightforward for explicit Euler integration in time, the slope limiter scheme leads to systems of non-linear equations for the implicit Euler method, which have to be solved iteratively. Chapter 2.2.2 explains how this can be done for the non-linear reactive transport equation.

2.2.2 Coupling of transport and reaction processes

Reactive transport of a contaminant coupled to the consumption of an electron acceptor and growth of immobile bacteria can be described by the following system of non-linear partial differential equations:

$$\frac{\partial c_{sub}}{\partial t} = -\mathbf{v}\nabla c_{sub} + \nabla \cdot (\mathbf{D_{sub}}\nabla c_{sub}) - r_{sub} \tag{2.46}$$

$$\frac{\partial c_{ea}}{\partial t} = -\mathbf{v}\nabla c_{ea} + \nabla \cdot (\mathbf{D_{ea}}\nabla c_{ea}) - r_{ea} \tag{2.47}$$

$$\frac{\partial X_{att}}{\partial t} = r_{gr} - r_{dec}. \tag{2.48}$$

Spatial discretization is performed as outlined in the chapter on conservative transport (2.2.1). Differences in the diffusion coefficient for substrate and electron acceptor result in a different mobility matrix $\mathbf{M_{mob}}$ for each species. Discretization in space leads to the following system of non-linear ordinary differential equations:

$$\mathbf{M}_{STORE}\frac{\partial \mathbf{c}}{\partial t} + \mathbf{M}_{MOB}\mathbf{c} = \mathbf{r}_{in} + \mathbf{M}_{STORE}\mathbf{r}_{REAC}, \tag{2.49}$$

where $\mathbf{M}_{MOB}$ and $\mathbf{M}_{STORE}$ are the $n_{cells}n_{comp} \times n_{cells}n_{comp}$ global mobility and storage matrices (with ne number of compounds n_{comp}), respectively:

$$\mathbf{M}_{MOB} = \begin{bmatrix} \mathbf{M}^{sub}_{mob} & \mathbf{0} & \mathbf{0} \\ \mathbf{0} & \mathbf{M}^{ea}_{mob} & \mathbf{0} \\ \mathbf{0} & \mathbf{0} & \mathbf{0} \end{bmatrix} \tag{2.50}$$

$$\mathbf{M}_{STORE} = \begin{bmatrix} \mathbf{M}^{sub}_{store} & \mathbf{0} & \mathbf{0} \\ \mathbf{0} & \mathbf{M}^{ea}_{store} & \mathbf{0} \\ \mathbf{0} & \mathbf{0} & \mathbf{M}^{X_{att}}_{store} \end{bmatrix}, \tag{2.51}$$

and $\mathbf{c}$, $\mathbf{r}_{REAC}$ and $\mathbf{r}_{IN}$ are column vectors of concentration, reaction rate, and incoming mass flux for the substrate, the electron acceptor and the biomass for all cells with the length $n_{cells}n_{comp}$:

$$\mathbf{c} = \begin{bmatrix} \mathbf{c}_{sub} \\ \mathbf{c}_{ea} \\ \mathbf{X}_{att} \end{bmatrix} \quad (2.52) \qquad \mathbf{r}_{REAC} = \begin{bmatrix} -\mathbf{r}_{sub} \\ -\mathbf{r}_{ea} \\ \mathbf{r}_{gr} - \mathbf{r}_{dec} \end{bmatrix} \quad (2.53) \qquad \mathbf{r}_{IN} = \begin{bmatrix} \mathbf{r}_{in}^{sub} \\ \mathbf{r}_{in}^{ea} \\ \mathbf{0} \end{bmatrix}. \quad (2.54)$$

Depending on the question of interest, the coupled system of reactive-transport equations was either solved jointly by the global implicit method or the transport and reaction terms were integrated in time consecutively by an operator split approach.

Adopting the operator split approach, transport and reactive processes, which occur simultaneously in nature, are artificially separated in the numerical scheme. This introduces a splitting error, the magnitude of which depends on the time-step size and the speed of the reaction (Herzer and Kinzelbach, 1989; Valocchi and Malmstead, 1992; Morshed and Kaluarachchi, 1995). The splitting error can be minimized by iterating between transport and reaction step (Schäfer et al., 1998). Advantages of the operator-split approach are its straight-forward implementation, the possibility to couple existing transport and biogeochemical codes, and the fact that different, individually optimized numerical schemes can be applied to the transport and the reaction term (Herzer and Kinzelbach, 1989; Valocchi and Malmstead, 1992; Morshed and Kaluarachchi, 1995).

Adopting the global implicit method does not produce a splitting error but can be computationally expensive, since large systems of non-linear equations have to be solved (Herzer and Kinzelbach, 1989). Implicit integration in time of the advection term produces numerical diffusion in the direction of flow, the magnitude of which depends on the time step size.

Global implicit method

Integration in time of the full system of reactive transport equations by the implicit Euler method yields the following system on non-linear algebraic equations:

$$(\mathbf{M}_{STORE} + \Delta t \mathbf{M}_{MOB} - \Delta t \mathbf{M}_{STORE} \mathbf{r}_{REAC}(\mathbf{c}_{new}))\, \mathbf{c}_{new} = \Delta t \mathbf{r}_{IN} + \mathbf{M}_{STORE} \mathbf{c}_{old}, \quad (2.55)$$

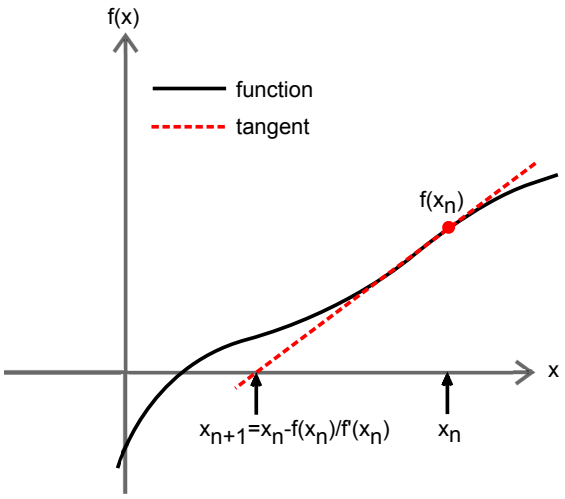

Figure 2.4: *Illustration of the Newton method.*

in which the non-linearity steams from the Monod kinetic expression used to simulate microbial growth (Eq. 2.13).

The Newton method, which is an iterative numerical scheme to find the root of a non-linear function, is used to solve the non-linear system of equations. For a non-linear function with a single variable Netwon's method consist of the following steps (see illustration in Fig. 2.4):

1. The basic principle is to approximate the non-linear function $f(x)$ by its tangent $t(x)$ at an starting point x_n and to find the root of the tangent x_{n+1}.

$$t(x) = f(x_n) + f'(x_n)\,(x_{n+1} - x_n) = 0 \tag{2.56}$$

$$x_{n+1} = x_n - \frac{f(x_n)}{f'(x_n)} \tag{2.57}$$

2. The root of the tangent x_{n+1} is taken as first approximation for the root of the non-linear function $f(x)$ and the deviation of $f(x_{n+1})$ from zero (the residual) is calculated.

3. Steps 1 and 2 are repeated with the tangent to point x_{n+1}, the current approximation for the root of $f(x)$, until the deviation of $f(x_{n+1})$ from zero is smaller than a specified tolerance.

Newton's method can be extended from a single equation with one variable to a system of equations with multiple variables, which is denoted Newton-Raphson Method. The

non-linear system of reactive-transport equations given in equation 2.55 has to be solved for each time step. Therefore it is linearized by the Newton-Raphson method at each time step, which is identical to finding the the roots of the system:

$$(\mathbf{M}_{STORE} + \Delta t \mathbf{M}_{MOB})\,\mathbf{c}_{new} - \Delta t \mathbf{r}_{IN} - \Delta t \mathbf{M}_{STORE}\mathbf{r}_{REAC}(\mathbf{c}_{new}) - \mathbf{M}_{STORE}\mathbf{c}_{old} = \mathbf{0}. \tag{2.58}$$

The Newton-Raphson method is an iterative numerical scheme that will only give an approximation of the roots. This implies that we have to define a stopping criteria for the algorithm. Therefor the vector of residuals ε:

$$\varepsilon = (\mathbf{M}_{STORE} + \Delta t \mathbf{M}_{MOB})\,\mathbf{c}_{new} - \Delta t \mathbf{r}_{IN} - \Delta t \mathbf{M}_{STORE}\mathbf{r}_{REAC}(\mathbf{c}_{new}) - \mathbf{M}_{STORE}\mathbf{c}_{old}, \tag{2.59}$$

is calculated at each iteration step and the iteration is stopped when a norm of the residuals is smaller than a specified value. Linearization of equation 2.59 about the current estimate of vector $\mathbf{c}_{new}^{n}$ at each iteration step leads to the vector of roots $\mathbf{c}_{new}^{n+1}$ to the linearized system of equations:

$$\mathbf{c}_{new}^{n+1} = \mathbf{c}_{new}^{n} - \mathbf{J}_{\varepsilon}^{-1}(\mathbf{c}_{new}^{n})\,\varepsilon(\mathbf{c}_{new}^{n}), \tag{2.60}$$

with the $n_{cells}n_{comp} \times n_{cells}n_{comp}$ Jacobian matrix $\mathbf{J}_{\varepsilon}$:

$$\mathbf{J}_{\varepsilon} = \mathbf{M}_{STORE} + \Delta t \mathbf{M}_{MOB} - \Delta t \mathbf{M}_{STORE}\mathbf{J}_{REAC}. \tag{2.61}$$

with the Jacobian matrix for the non-linear reaction rates $\mathbf{J}_{REAC}$ given by:

$$\mathbf{J}_{REAC} = \begin{bmatrix} -\frac{\partial \mathbf{r}_{sub}}{\partial \mathbf{c}_{sub}} & -\frac{\partial \mathbf{r}_{sub}}{\partial \mathbf{c}_{ea}} & -\frac{\partial \mathbf{r}_{sub}}{\partial \mathbf{X}_{att}} \\ -\frac{\partial \mathbf{r}_{ea}}{\partial \mathbf{c}_{sub}} & -\frac{\partial \mathbf{r}_{ea}}{\partial \mathbf{c}_{ea}} & -\frac{\partial \mathbf{r}_{ea}}{\partial \mathbf{X}_{att}} \\ \frac{\partial (\mathbf{r}_{gr}-\mathbf{r}_{dec})}{\partial \mathbf{c}_{sub}} & \frac{\partial (\mathbf{r}_{gr}-\mathbf{r}_{dec})}{\partial \mathbf{c}_{ea}} & \frac{\partial (\mathbf{r}_{gr}-\mathbf{r}_{dec})}{\partial \mathbf{X}_{att}} \end{bmatrix} \tag{2.62}$$

in which each entry $\frac{\partial \mathbf{r}_i}{\partial \mathbf{c}_j}$ is a $n_{cells} \times n_{cells}$ diagonal matrix, containing the partial derivative of reaction rate i for each grid cell with respect to the concentration of compound j.

The partial derivatives of the reaction rates with respect to substrate, electron acceptor and biomass concentration are approximated by direct numerical differentiation. For the first entry of $\mathbf{J}_{REAC}$ this leads to:

$$\frac{\partial \mathbf{r}_{sub}}{\partial \mathbf{c}_{sub}} \approx \frac{\mathbf{r}_{sub}(\mathbf{c}_{sub} + \Delta \mathbf{c}_{sub}) - \mathbf{r}_{sub}(\mathbf{c}_{sub})}{\Delta \mathbf{c}_{sub}}, \tag{2.63}$$

in which $\Delta \mathbf{c}_{sub}$ is an increment in substrate concentration by 1%. At the end of each iteration step the vector of residuals ε (Eq. 2.59) is updated and the iteration is stopped when the maximum residual is smaller than a specified value. As initial guess $\mathbf{c}_{new}$ is set to $\mathbf{c}_{old}$, which would be the result under steady state conditions.

The Newton-Raphson method converges quadratically, which is fast once $\mathbf{c}_{new}$ is close to the solution. However, since it is only locally convergent, convergence might not be achieved at all if the initial guess of $\mathbf{c}_{new}$ is far away from the solution. To ensure convergence and hence the reduction of the residual for each Newton step the relaxation factor λ, which can range from zero to one, is implemented:

$$\mathbf{c}_{new}^{n+1} = \mathbf{c}_{new}^{n} - \lambda \left(\mathbf{J}_{\varepsilon}^{-1} \left(\mathbf{c}_{new}^{n} \right) \varepsilon(\mathbf{c}_{new}^{n}) \right). \tag{2.64}$$

If the residual is not reduced within a Newton step, the step size is decreased by taking a smaller λ and the Newton step is repeated.

A major benefit of the global implicit method is that the time step size Δt can be adapted during the calculation. Small time steps can be chosen at times of rapid changes and larger time steps once the system has stabilized. Adaptive time stepping helps to find a good balance between numerical accuracy and computational costs. The time step size is continuously updated based on the number of iterations needed to solve the system of non-linear equations for the current time point. If the Newton-Raphson method does not converge within a specified maximum number of iterations, Δt is reduced by a factor of two and the Newton iteration for the current time point is repeated with the new value of Δt. If convergence, however, is achieved within less than a specified minimum number of iterations, Δt is doubled. To minimize the effect of numerical diffusion on the model outcome, Δt is artificially fixed to small values for periods when concentration fronts move through the system.

Operator split approach

Integration in time of the transport terms is performed as outlined for conservative transport at the end of chapter 2.2.1. The result from the transport step is taken as input for the reaction step and the implicit Euler method is applied for integration in time of the reaction term, using the Newton-Raphson method to solve the non-linear system of equations for each time step.

Chapter 3

Isotope fractionation in steady-state contaminant plumes[1]

This chapter deals with the coupled effect of transverse dispersion and fringe-controlled biodegradation on overall isotope fractionation of BTEX-hydrocarbons. Since the reaction depends on transverse mixing of the reaction partners, the coupled effects of mixing and degradation on isotope fractionation have to be assessed. We hypothesize that transverse dispersion, if acting as rate-limiting step, decreases the extent of overall isotope fractionation similarly to inter-phase mass-transfer processes in batch systems of biodegradation (Thullner et al., 2008; Kampara et al., 2008; Aeppli et al., 2009; Thullner et al., 2013). The masking of reaction-induced isotope fractionation by a preceding (non-fractionating) process, such as transport to the reactive site, is well known as 'commitment to catalysis' in the isotope literature. Observable isotope fractionation corresponds only to reaction-induced isotope fractionation, if the actual bond conversion, causing the isotope effect, represents the rate-limiting step (Elsner et al., 2005). Masking of reaction-induced isotope fractionation by a preceding rate-limiting, but non-fractionating process, results in a reduced observable (apparent) extent of isotope fractionation.

[1]The content presented in this chapter is modified from *D. Eckert, M. Rolle, O.A. Cirpka (2012). Numerical simulation of isotope fractionation in steady-state bioreactive transport controlled by transverse mixing. Journal of Contaminant Hydrology, 140, pp 95-106* (Eckert et al., 2012).

Assuming first-order processes, the apparent fractionation factor (α_{app}) can be related to the intrinsic fractionation factor (α_i) for the reactive step by (Northrop, 1981):

$$\alpha_{app} = \frac{1 + k_{reac}/k_{tr}}{1/\alpha_i + k_{reac}/k_{tr}}, \tag{3.1}$$

in which k_{reac} and k_{tr} are the first-order rate coefficients of the fractionating reactive, and the preceding non-fractionating mass-transfer step, respectively. Another complication in the interpretation of the isotope signals may arise from dispersion itself leading to fractionation between the heavy and light isotopologues of the contaminant (Rolle et al., 2010; van Breukelen and Rolle, 2012).

The complex effects of coupled physical and (bio)chemical processes on isotope fractionation are resolved by reactive-transport simulations using ethylbenzene as model compound. The focus lies on local-scale transverse mixing which is typically very small and can limit (bio)chemical reactions relying on mixing of substrates (e.g., electron donors and electron acceptors) and nutrients at the fringe of contaminant plumes. Two-dimensional simulations at the laboratory scale, where the flow field is assumed to be uniform, and at a larger field scale considering heterogeneous hydraulic conductivity fields, are performed. In the latter case, solute transport is influenced by the spatial variability of groundwater flow which determines local transverse mixing. For both, the homogeneous local scale and the heterogeneous field scale scenarios, an interpretation of the isotopic signals based on depth-integrated sampling, which represents the most common setup in the assessment of contaminated field sites, is provided.

3.1 Model description

Laboratory-scale simulations

The rates of the microbially-mediated ethylbenzene degradation and consumption of the electron acceptor nitrate are described by dual-Monod kinetics. Biomass is assumed to be attached to the sediment matrix and thus immobile. Its dynamics are governed by microbial growth (see Eq. 2.14) and linear decay of the biomass under consumption of the oxidizing agent nitrate.

The purpose of the laboratory-scale simulations is to study the interplay of transverse dispersion and biodegradation and its effect on isotope fractionation along the length of

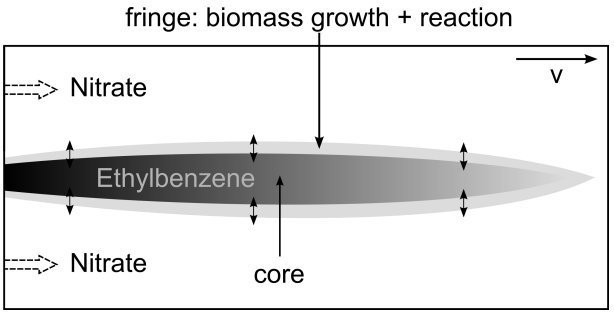

Figure 3.1: *General setup of the bioreactive transport model.*

a steady-state plume in a uniform groundwater flow field. Here, we mimic quasi two-dimensional setups used in recently performed flow-through microcosm experiments (e.g., Bauer et al., 2009a,b; Rolle et al., 2010). Figure 3.1 schematically illustrates the setup for the two-dimensional bioreactive transport model.

Ethylbenzene is continuously introduced with a constant inflow concentration of $c_S^{in} = {}^{12}c_S^{in} + {}^{13}c_S^{in} = 110\ \mu$M in the center of the inflow boundary through a line source with a width of 0.6 *cm*, whereas nitrate is introduced above and below the ethylbenzene line source with an inflow concentration of $c_{NO3}^{in} = 360\ \mu$M. The flow field is assumed uniform, which can only be achieved in laboratory experiments. At the outflow boundary, the flux of ethylbenzene and nitrate is restricted to the advective contribution. The remaining part of the boundary is assumed to be a no-flow boundary. The transport and reaction parameters listed in Table 3.1 are adapted from Rolle et al. (2010).

With the selected geometry, inflow concentrations, and kinetic parameters, 99% of the injected ethylbenzene mass flux is degraded before reaching the outflow of the model domain. The isotope ratio of ethylbenzene at the inlet is set to the ratio of the standard for carbon isotope measurements (Pee Dee Belemnite, ${}^{13}C/{}^{12}C = 0.011237$). Assuming an electron-transfer fraction of 0.5 from ethylbenzene to the synthesis of new cellular material and conceptualizing the biomass as chemical species $C_5H_7O_2N$, the stoichiometry for ethylbenzene degradation under nitrate reducing conditions, including biomass growth, reads as:

$$C_8H_{10} + 4.2NO_3^- + 1.05NH_4^+ + 0.4H^+ \rightarrow 1.05C_5H_7O_2N + 2.1N_2 + 2.75HCO_3^- + 2.25H_2O. \quad (3.2)$$

The empirical correlation of Worch (1993) is applied to calculate the aqueous diffusion coefficients D_{aq} of the light and the heavy ethylbenzene isotopologues. The correlation

Table 3.1: *Transport and reaction parameters in the base case of the uniform laboratory-scale simulations.*

Geometric Parameters		
domain dimensions (L×H)	$[m]$	1×0.1
number of cells	$[-]$	200×200
Transport Parameters		
seepage velocity, v	$[m/s]$	$1.39 \cdot 10^{-5}$
porosity, n	$[-]$	0.4
tortuosity, τ	$[-]$	2.5
grain size, d	$[m]$	$2 \cdot 10^{-4}$ [a]
longitudinal dispersivity, α_l	[m]	$2 \cdot 10^{-4}$
$D_{aq}^{^{12}C}$ at 10°C	$[m^2/s]$	$6.5679 \cdot 10^{-10}$ [b]
$D_{aq}^{^{13}C}$ at 10°C	$[m^2/s]$	$6.5354 \cdot 10^{-10}$ [b]
$D_{aq}^{NO_3^-}$ at 10°C	$[m^2/s]$	$1.24 \cdot 10^{-9}$
ε_{Diff}^{kin}	[-]	-5‰
Inflow Concentrations		
source width	$[m]$	0.006
c_s^{in}	$[\mu M]$	110
$c_{NO_3^-}^{in}$	$[\mu M]$	360
Biokinetic Parameters		
k_{max}	$[1/d]$	3.1
K_s	$[\mu M]$	11.4
K_{NO3}	$[\mu M]$	70
k_{dec}	$[1/d]$	0.02
Y_s	$[\mu M_{bio}/\mu M_s]$	1.05
f_{deg}	$[\mu M_{NO3}/\mu M_s]$	4.2
f_{dec}	$[\mu M_{NO3}/\mu M_{bio}]$	4.2
X_{max}	$[\mu M]$	250
ε_r^{kin}	[-]	-2.2‰ [c]

[a] Reconstructed from hydraulic conductivity using the relation of Hazen (1893).
[b] Calculated with empirical correlation of Worch (1993).
[c] Value from Meckenstock et al. (2004).

of Worch (1993) predicts a dependence of the aqueous diffusion coefficient D_{aq} on the molecular mass M of the diffusing compound close to $1/\sqrt{M}$:

$$D_{aq} = 3.595 \cdot 10^{-14} \frac{T}{\eta M^{0.53}}, \tag{3.3}$$

in which T [K] is the absolute temperature and η $[Pa \cdot s]$ is the dynamic viscosity of the

fluid. The calculated values are in agreement with the experimental values for deuterated species reported by Mills (1976) and Jin et al. (2014) and with the outcomes of the flow-through experiments of Rolle et al. (2010). Eq. 3.3 yields a slight difference in the aqueous diffusion coefficients between the two ethylbenzene isotopologues, thus leading to isotope fractionation by diffusion. In analogy to isotope fractionation by biodegradation, fractionation by diffusion can be described by the fractionation factor α^{kin}_{Diff} $[-]$:

$$\alpha^{kin}_{Diff} = \frac{^{13}D_{aq}}{^{12}D_{aq}} = \left(\frac{M_{12C}}{M_{13C}}\right)^{0.53}. \tag{3.4}$$

The isotopologue-specific transverse dispersion coefficients $^{12}D_t$ and $^{13}D_t$ are calculated from the diffusion coefficient obtained from Eq. 3.3 according to Eq. 2.6.

Field-scale simulations

Few recent contributions have attempted to assess the isotope fractionation behavior in complex heterogeneous porous media (e.g. LaBolle et al., 2008; Green et al., 2010; van Breukelen and Rolle, 2012), whereas the vast majority of scenario and/or applied modeling studies relied upon homogeneous equivalent representations of the aquifer system and upscaled macroscopic transport parameters. The nonuniform flow fields in heterogeneous aquifers govern solute transport and lead to significant enhancement and uncertainty of transverse mixing (Cirpka et al., 2011).

In the field-scale simulations, we consider an explicitly resolved representation of aquifer heterogeneity which leads to direct upscaling of transverse mixing. This is useful to gain insights into the interaction between physical mixing processes (not relying on upscaling) and (bio)chemical reactions and to improve our capability to interpret observed isotopic signatures in complex heterogeneous environments. To test how heterogeneity affects the overall isotope fractionation of the contaminants, we consider a setup similar to the laboratory-scale simulations with identical boundary conditions but larger dimensions (40 m $\times$ 2 m, 1000 $\times$ 100 cells) and heterogeneous conductivity fields. The latter are binary, representing a low-conductivity matrix with high-permeability inclusions (Werth et al., 2006). The typical length scale for the inclusions is 1 m in the horizontal direction and 10 cm in the vertical direction. Three binary fields are considered, differing in the conductivity contrast between the matrix and the inclusions. The conductivity of the matrix is set to the same value used for the laboratory-scale simulations described above and remains identical in the three binary fields. The conductivity of the high-permeability inclusions is chosen to obtain conductivity ratios $K_{inclusions}/K_{matrix}$ of 2, 10, and 50, respectively.

The reaction and transport parameters are identical to the ones used for the laboratory-scale simulations. Ethylbenzene is introduced over 5 % of the total incoming water flux in all K-field scenarios, implying a case-dependent width of the source. The porosity is kept constant throughout the domain and the grain size is evaluated from local conductivity values using the empirical correlation of Hazen (1893) (see Chiogna et al., 2011a).

Numerical methods

All simulations are performed in two-dimensional domains, discretized by the cell-centered Finite Volume Method using streamline oriented grids (Cirpka et al., 1999a,c). Advective fluxes are approximated by upwind differentiation. Temporal discretization is performed by the implicit Euler method. The resulting system of coupled non-linear algebraic equations is linearized by the Newton-Raphson method, and the UMFPACK solver, implemented in Matlab (Davis and Duff, 1997), is used to solve the linear system of equations. To obtain the steady-state concentration distributions, the system of equations is solved for the transient case until steady-state conditions are reached. An adaptive time-stepping scheme is applied to accelerate the rate at which the steady state is reached. The code was written as a Matlab program.

3.2 Results and discussion

3.2.1 Homogeneous laboratory scale

3.2.1.1 Effect of mixing control on isotope fractionation

Recent studies on biodegradation of organic contaminants in laboratory batch systems showed that kinetic mass-transfer processes affect isotope fractionation, if they represent the rate-limiting step in overall biodegradation (Thullner et al., 2008; Kampara et al., 2008; Aeppli et al., 2009). In this study we analyze mixing-controlled biodegradation in flow-through systems, which may be conceptualized as the sequence of a physical process, namely transverse mixing, and a reactive process, namely the bioreaction of the contaminant with the electron acceptor. The process exhibiting the larger characteristic time scale limits the overall degradation and dominates the observable overall isotope fractionation. Therefore, the physical mixing process, even if not fractionating *per se*, may lead to a significant modulation of isotope fractionation. If transverse

mixing represents the rate-limiting step, a significant impact on the observed isotope ratios is expected, even in the absence of any inter-phase mass-transfer process, such as sorption or NAPL dissolution.

We perform simulations using different specific rates of ethylbenzene degradation to assess the impact of the interplay between transverse mixing and different reaction kinetics on the simulated isotope ratios. As base-case scenario, we consider the kinetic parameters ($k_{max} = 3.1\ d^{-1}$ and $k_{dec} = 0.02\ d^{-1}$) determined for the microbial strain *Aromatoleum aromaticum* EbN1, an anaerobic degrader using nitrate as electron acceptor (Rolle et al., 2010). Successively, the maximum specific degradation rate constant k_{max} is increased and decreased by a factor of ten. The respective increase or decrease of this parameter may be representative of the activity of a more or less efficient degrader and of the effect of different environmental conditions, such as the presence of dissolved oxygen or sulfate as principal terminal electron acceptor, that can favor or slow down the kinetics of contaminant degradation. We calculate the remaining fraction $f(x)$ [-] of ethylbenzene at different longitudinal travel distances as the ratio of the contaminant mass flux $\dot{m}_s(x)$ at location x and the injected mass flux at the source $\dot{m}_s^{in}$:

$$f(x) = \frac{\dot{m}_s(x)}{\dot{m}_s^{in}}. \tag{3.5}$$

The computed length profile of $f(x)$ is plotted in Figure 3.2. Reducing k_{max} from $3.1\ d^{-1}$ to $0.31\ d^{-1}$ affects the remaining mass-flux fraction of ethylbenzene strongly, whereas the effect of increasing k_{max} by a factor of ten is less noticeable. This suggests that the experimental value ($k_{max} = 3.1\ d^{-1}$) used in the base-case scenario is already representative of a regime where mixing is the main controlling factor. As a consequence, further increasing the reaction-rate constant has little impact on the overall degradation of the contaminant. On the contrary, decreasing the specific rate coefficient of degradation results in considerable changes of the remaining fraction of ethylbenzene, therefore indicating that the microbial reaction becomes the limiting step to the overall degradation. The insert on the upper right corner of Figure 3.2 represents the results in a semilogarithmic scale: it is interesting to observe that towards the end of the plume the results for the cases with $k_{max} = 3.1\ d^{-1}$ and $k_{max} = 31\ d^{-1}$, which appear to merge in the linear representation, show distinct patterns. This indicates that the rate-limiting effect of transverse mixing vanishes towards the end of the plume. In this regime of low contaminant concentrations the electron acceptor is present throughout the entire width of the plume at concentration levels that don't limit biodegradation.

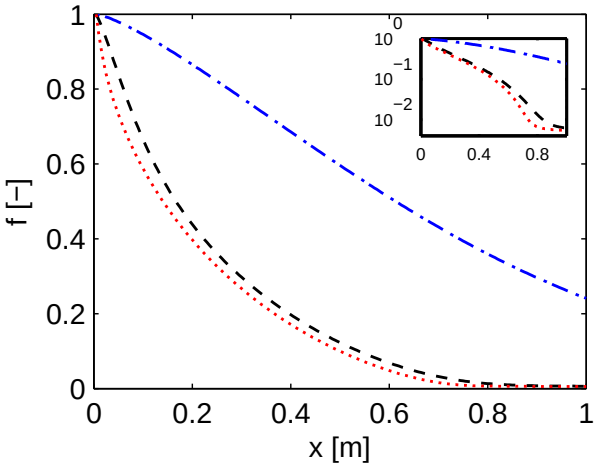

Figure 3.2: *Remaining fraction of injected ethylbenzene mass flux in the uniform laboratory-scale simulations; blue dash-dotted line:* $k_{max} = 0.31\ d^{-1}$*; black dashed line:* $k_{max} = 3.1\ d^{-1}$*; red dotted line:* $k_{max} = 31\ d^{-1}$.

Interpretation of Isotope Ratios

In mixing-controlled biodegradation, reaction rates vary strongly in the vertical direction with the highest rates encountered at the plume fringe. Consequently, also the isotope signals of the contaminants show steep gradients, with the heavy isotopologues being typically enriched at the plume fringes (Prommer et al., 2009; Rolle et al., 2010).

Depth-resolved isotope measurements are highly desirable, since averaging over steep isotopic gradients by sampling long-screen monitoring wells leads to apparent isotope ratios that are dominated by zones of high contaminant concentrations and low microbial activity (e.g. Kopinke et al., 2005; Abe and Hunkeler, 2006; van Breukelen and Prommer, 2008; Thullner et al., 2012). Unfortunately, high-resolution monitoring devices, that allow resolving steep concentration and isotope gradients at the fringes of organic contaminant plumes, are currently installed only at few contaminated sites (e.g. Hunkeler et al., 2004; Anneser et al., 2008). Thus, in most practical applications, isotope signatures of contaminants are measured from samples collected in fully-screened monitoring wells. The following interpretation is, therefore, given for depth-integrated sampling.

As discussed in the introduction, isotope data are conventionally analyzed using the Rayleigh equation, eq. (1.3). In the given steady-state setup, the time dependence of the isotope ratio and the remaining fraction of the contaminant appearing in eq. (1.3) have to be replaced by the dependence on travel distance x. Also, we consider the remaining

fraction of the depth integrated mass flux rather than the concentration. The Rayleigh equation postulates a power-law dependence of the isotope ratio on the remaining fraction of the contaminant. If the Rayleigh equation holds, the measured values follow a straight line with a constant slope ε_r^{kin} in a double logarithmic plot of the isotope ratio vs. the remaining contaminant fraction (denoted as Rayleigh plot).

Figure 3.3 shows the simulated dependence of $\log_{10}(R(x)/R_0)$ on $\log_{10}(f)$ for the given setup using different values of the maximum specific reaction rate coefficient k_{max}. The isotope ratios are computed for the total mass flux of the contaminant. The solid line in Figure 3.3 represents the linear relationship as expected by the Rayleigh equation for the given enrichment factor $\varepsilon_r^{kin} = -2.2$ ‰. When the degradation rate is small ($k_{max} = 0.31\ d^{-1}$, squares in Figure 3.3), the simulation results are well described by the Rayleigh approach. By contrast, the profiles for higher values, $k_{max} = 3.1\ d^{-1}$ (dashed line) and $k_{max} = 31\ d^{-1}$ (dotted line), respectively, do not follow the linear trend. In fact, for identical isotope ratios, the simulated remaining fraction of ethylbenzene mass flux is much smaller than the one predicted by the Rayleigh equation. That is, the Rayleigh equation gives conservative estimates regarding the degree of biodegradation.

The deviation from the linear Rayleigh trend increases with increasing k_{max} due to increasing limitation of the overall degradation by transverse mixing. Interestingly, the increasing limitation by transverse mixing from $k_{max} = 3.1\ d^{-1}$ to $k_{max} = 31\ d^{-1}$ shows a strong effect on isotope fractionation, whereas it has only a minor effect on the remaining ethylbenzene fraction (Figure 3.2). For the limiting scenario of an instantaneous reaction, no more isotope fractionation could be observed at all, because all ethylbenzene molecules would immediately react upon mixing with nitrate, regardless of their isotopic composition. The latter behavior would lead to a straight horizontal line in the Rayleigh plot. That is, while the overall remaining fraction of contaminant mass flux hardly differs between the reference case, $k_{max} = 3.1\ d^{-1}$, and the limit $k_{max} \to \infty$, the isotope fractionation dramatically changes from some fractionation (even though not as strong as predicted by the microbial reaction alone) to no fractionation at all, since in the latter case there is no more isotope selection in the reaction.

The results for $k_{max} = 3.1\ d^{-1}$ and $k_{max} = 31\ d^{-1}$ show nonlinear patterns for small to intermediate $log(f)$ values (i.e., large remaining ethylbenzene fraction) that considerably deviate from the linear Rayleigh behavior. For large $log(f)$ values (i.e., low remaining ethylbenzene fraction) simulation results show a linear dependence between $log(f)$ and $log(R_x/R_0)$.

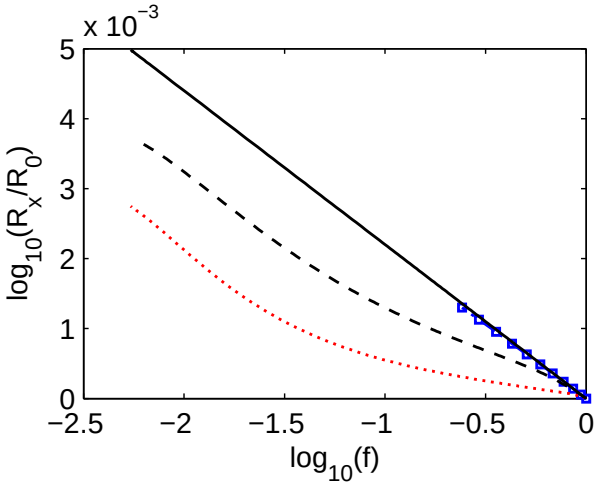

Figure 3.3: *Rayleigh plot of depth-averaged samples in the uniform laboratory-scale setup; solid line: linear Rayleigh model; blue squares: $k_{max} = 0.31\ d^{-1}$; black dashed line: $k_{max} = 3.1\ d^{-1}$; red dotted line: $k_{max} = 31\ d^{-1}$.*

Directly at the inflow boundary, the transverse concentration gradients are practically infinite so that transverse dispersion is not yet rate-limiting. However, already at small distances from the inlet, the transverse concentration gradients decrease, and the plume becomes wider, so that overall degradation is increasingly controlled by physical mixing rather than microbial activity. This results in the increasing deviation from the linear Rayleigh line in Figure 3.3. With decreasing plume width and decreasing ethylbenzene concentration, transverse mixing lengths and reaction rates decrease. The overall degradation becomes less controlled by physical mixing and the slope in the Rayleigh plot slowly tends towards ε_r^{kin}. Finally, towards the end of the plume, the concentrations of ethylbenzene and the biomass become so small that mixing with nitrate is no more limiting at all and hence the remaining degradation shows a linear Rayleigh plot.

Additional simulations (results not shown), in which we changed the width of the contaminant source, resulted in substantial deviations from the linear trend in the Rayleigh plot when the source width was increased, implying even stronger limitation by transverse mixing.

In practical applications, the Rayleigh equation is often used to estimate the extent of biodegradation, here denoted $B_{Rayleigh}$:

$$B_{Rayleigh} = \left(1 - \left(\frac{R_x}{R_0}\right)^{\frac{1}{\varepsilon_r^{kin}}}\right), \tag{3.6}$$

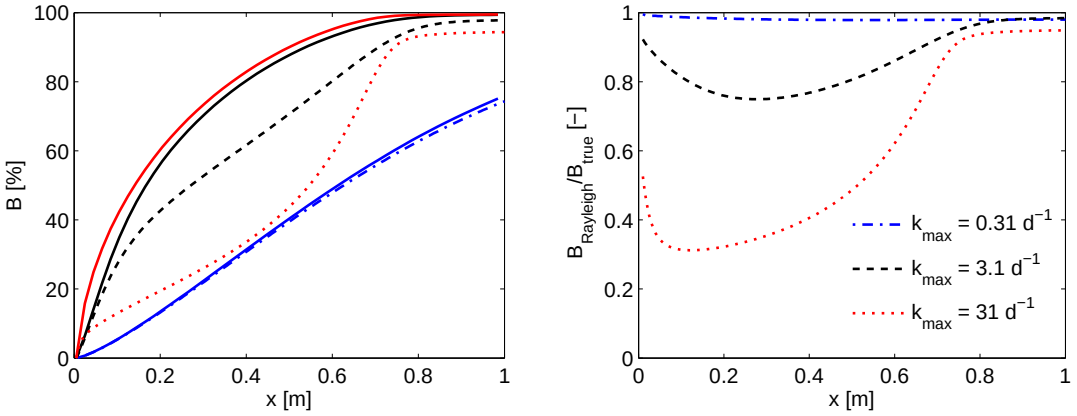

Figure 3.4: *Left subplot: Comparison of the extent of biodegradation B estimated by the Rayleigh equation and the extent of biodegradation obtained from the model (solid lines) as function of travel distance; blue: $k_{max} = 0.31\ d^{-1}$; black: $k_{max} = 3.1\ d^{-1}$; red: $k_{max} = 31\ d^{-1}$; right subplot: Extent of over-/underestimation of the actual extent of biodegradation by the Rayleigh equation.*

In Figure 3.4, the extent of biodegradation $B_{Rayleigh}$, estimated by the Rayleigh equation, is compared to the true extent of biodegradation B_{true} (solid lines), calculated from the remaining fraction f of ethylbenzene mass flux:

$$B_{true} = (1 - f). \tag{3.7}$$

B_{true} is strongly underestimated by the Rayleigh equation for $k_{max} = 3.1\ d^{-1}$ (dashed lines) and $k_{max} = 31\ d^{-1}$ (dotted lines) for the largest part of the ethylbenzene plume. The underestimation decreases only near the end of the plume where the microbial reaction becomes rate-limiting. However, a slight underestimation remains due to the offset to the linear Rayleigh line as shown in Figure 3.3.

3.2.1.2 Effect of isotope fractionation by dispersion

Recently, Rolle et al. (2010) showed that transverse dispersion significantly fractionates between labeled (perdeuterated) and non-labeled ethylbenzene molecules in conservative and mixing-controlled bioreactive transport experiments. Fractionation by transverse dispersion caused an enrichment of labeled ethylbenzene molecules in the plume core and their depletion at the plume fringes. In fact, dispersive mass-transfer is faster for the lighter (non-labeled) ethylbenzene molecules than for the heavier (labeled) ones. Biodegradation, in contrast, led to the enrichment of the heavier ethylbenzene molecules

at the plume fringes, where the reaction predominantly takes place. For weakly fractionating reactions it was shown that fractionation by transverse dispersion dominates the overall fractionation pattern. For more strongly fractionating reactions, the effects of both transverse dispersion and biodegradation had to be taken into account to reproduce the observed vertical isotope profiles .

In the current study, the fractionating effect of isotopologue-specific transverse dispersion is investigated for ethylbenzene at natural isotopic abundance. Isotope fractionation by dispersion is assumed to be weaker for ethylbenzene at natural abundance than for labeled (perdeuterated) ethylbenzene due to the smaller mass difference between light and heavy ethylbenzene molecules. The simulations are performed for ethylbenzene degradation under nitrate reducing conditions applying the reactive parameters of the base case discussed above ($k_{max} = 3.1\ d^{-1}$, $\varepsilon_r^{kin} = -2.2$ ‰).

Spatial distribution of simulated isotope ratios

Figure 3.5 shows the simulated spatial distribution of isotope ratios in the model domain, thus illustrating the coupled effects of dispersion and microbially-mediated reactions on isotope fractionation. The computed distribution of isotope ratios (R_x) is given as enrichment/depletion in the heavy isotopologue relative to the source zone (R_0) in the δ^{13}C notation.

$$\Delta^{13}\mathrm{C} = \left(\frac{R_x}{R_0} - 1\right). \tag{3.8}$$

The Δ^{13}C-values are only calculated for regions where the ethylbenzene concentration is above the detection limit for standard GC-MS measurements ($1\mu g/L$). Figure 3.5A shows results for conservative transport of ethylbenzene, considering isotopologue-specific dispersion, Figure 3.5B shows results for bioreactive transport of ethylbenzene, neglecting isotopologue-specific dispersion, and Figure 3.5C shows results for bioreactive transport of ethylbenzene, considering isotopologue-specific dispersion.

As experimentally observed for labeled ethylbenzene, transverse dispersion leads to a distinct spatial isotope pattern also for ethylbenzene at natural abundance (Figure 3.5A). The heavy isotopologue is slightly enriched along the plume centerline and strongly depleted at the fringe. The spatial distribution of δ^{13}C in Figure 3.5B (bioreactive transport, no isotopologue-specific dispersion) shows distinct maxima of δ^{13}C along the plume fringes. The δ^{13}C-distribution in Figure 3.5C (bioreactive transport with isotopologue-specific dispersion), by contrast, does not show these maxima of δ^{13}C-values at the fringes and has the largest enrichment of the heavy isotopologue in the plume core.

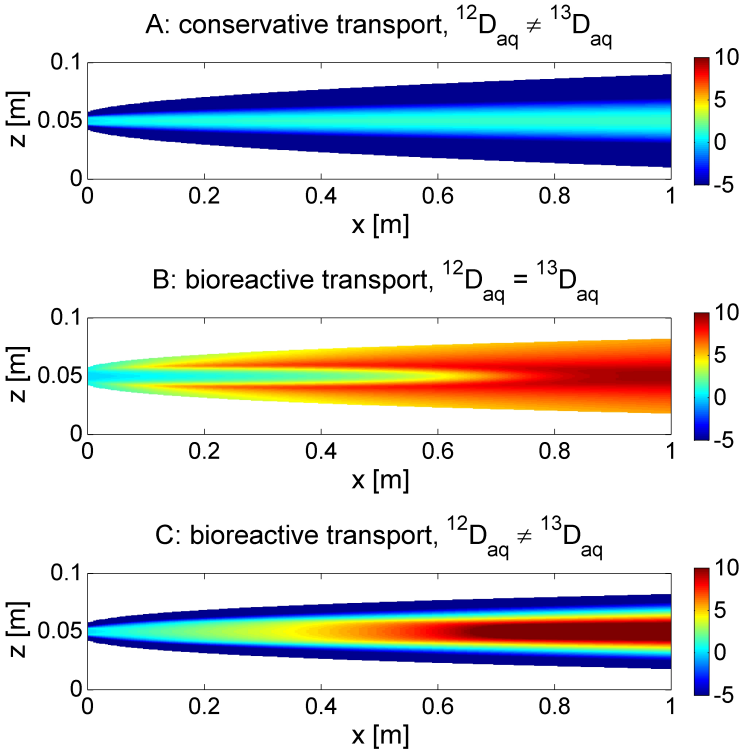

Figure 3.5: *Spatial distribution of $\Delta^{13}C$ [‰] in the laboratory-scale model domain; A: conservative transport considering isotopologue-specific dispersion, B: bioreactive transport neglecting isotopologue-specific dispersion, C: bioreactive transport considering isotopologue-specific dispersion.*

Interpretation of isotope ratios

Figure 3.6 shows longitudinal profiles of isotope ratios for samples averaged over the entire height of the domain. The Δ^{13}C-profile for conservative transport (solid line) remains constant at a value of zero, indicating the absence of net isotope fractionation. This is expected, because isotopologue-specific transverse dispersion makes the heavy and light ethylbenzene plumes spread differently only in the direction perpendicular to flow while the total longitudinal mass flux remains constant. Since it is the latter that is measured by depth-integrated sampling no net isotope fractionation is observed.

The longitudinal Δ^{13}C-profile for bioreactive transport considering isotopologue-specific dispersion (dash-dotted line) and the one neglecting it (dashed line) do not match. Δ^{13}C-values are larger for the case where isotopologue-specific dispersion is considered than

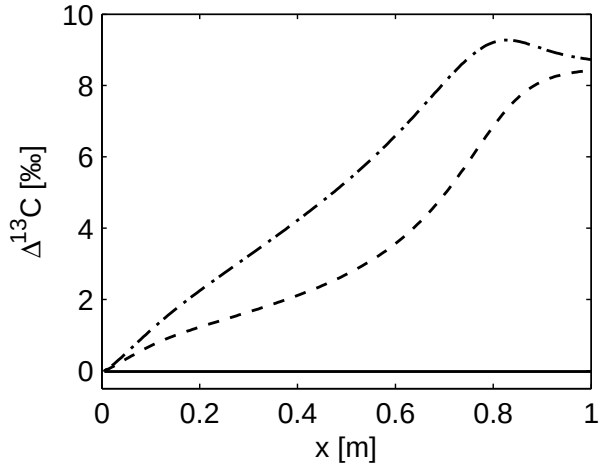

Figure 3.6: *Longitudinal profiles of Δ^{13}C-values obtained from depth-averaged concentrations in the uniform laboratory-scale simulations; solid line: conservative transport, isotopologue specific dispersion; dashed line: bioreactive transport, non isotopologue specific dispersion; dash-dotted line: bioreactive transport, isotopologue specific dispersion.*

for the case where it is neglected. In contrast to conservative transport, isotope fractionation by dispersion thus has an effect on isotope ratios in depth-averaged samples for bioreactive transport. This observation can be explained by the fact, that transverse dispersion and biodegradation act in series: in order to react, ethylbenzene and nitrate have to mix. The biomass in the reactive zone along the plume fringe samples ratios of heavy and light ethylbenzene isotopologues that have already been altered (prefractionated) by transverse dispersion. Since transverse dispersion is slightly faster for the light isotopologue, accounting for isotopologue specific dispersion leads to the increased removal of light ethylbenzene and consequently to increased Δ^{13}C-values. Towards the end of the domain the slopes of the Δ^{13}C- profiles decrease substantially, to finally approach a constant value. Ethylbenzene concentration in this regime are too low to support biomass and consequently no more isotope fractionation can be observed. Furthermore, a decrease in Δ^{13}C-values can be observed for the dash-dotted line (isotopologue specific dispersion) close to the right boundary of the domain (starting at about 0.8 m). This effect stems from the very low concentration levels in this portion of the domain, which cause biodegradation to occur predominantly in the plume core, where the heavy ethylbenzene isotopologue has been enriched by transverse dispersion.

Figure 3.7 shows a Rayleigh plot for bioreactive transport with isotope fractionation by both dispersion and the microbial reaction, considering three different values of the

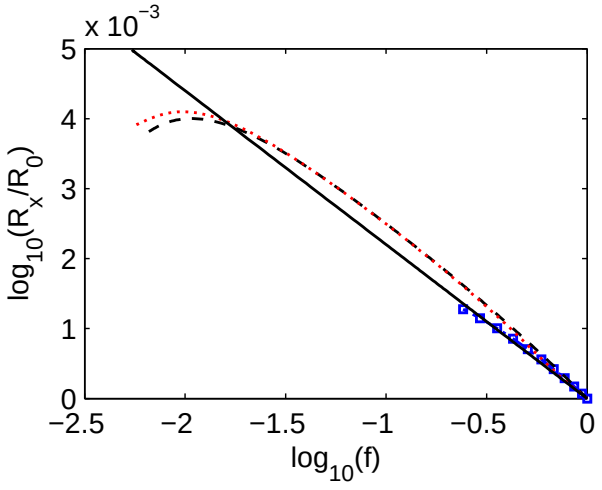

Figure 3.7: *Rayleigh plot of depth-averaged samples in the uniform laboratory-scale setup accounting for isotopologue specific dispersion coefficients; solid line: linear Rayleigh model; blue squares: $k_{max} = 0.31\ d^{-1}$; black dashed line: $k_{max} = 3.1\ d^{-1}$; red dotted line: $k_{max} = 31\ d^{-1}$.*

maximum specific rate coefficient. It can be observed that in the case of slow degradation kinetics ($k_{max} = 0.31\ d^{-1}$) the results are still captured by the linear trend of the Rayleigh line, although the agreement is less satisfying compared to the same case for the scenario reported in Figure 3.3. For faster reaction kinetics, the overall isotope signal is dominated by the prefractionating effect of transverse dispersion. While for isotopologue-independent transverse dispersion the Rayleigh model always underestimates the extent of biodegradation, the current results show that this can no more be the case if isotopologue-specific transverse dispersion is considered.

The effect of isotope fractionation by transverse dispersion strongly depends on the groundwater flow velocity (see Eq. 2.6). Figure 3.8 shows the isotope enrichment factor for transverse dispersion $\varepsilon_{D_t^{kin}}$ as function of the seepage velocity using the non-linear parameterization of D_t proposed by Chiogna et al. (2010) (solid line), and for the classical linear parameterization (dashed line). In both cases, we consider isotopologue-specific diffusion coefficients, but in the parameterization of Chiogna et al. (2010) the effects of diffusion do not vanish at high flow velocities. Independently of the D_t-parameterization, a fractionation effect can be observed at low velocities, where the contribution of pore diffusion to D_t is dominant. Considering the classical parameterization of D_t, isotope fractionation by transverse dispersion continuously decreases with increasing velocity to finally vanish at high velocities ($\lim_{v\to\infty} \varepsilon_{D_t} = 0$). Considering the D_t-parameterization of Chiogna et al. (2010), isotope fractionation by transverse

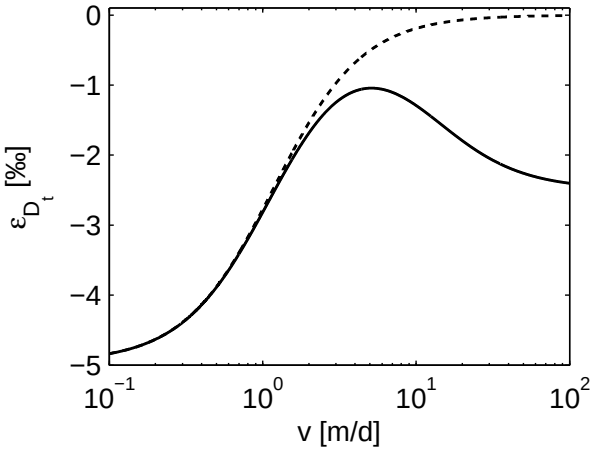

Figure 3.8: *Enrichment factor for isotope fractionation by transverse dispersion (ε_{D_t}) as function of velocity with the classical linear (dashed line) and a non linear compound-specific D_t-parameterization (solid line).*

dispersion does not vanish at high velocities. It decreases with increasing flow velocity up to a minimum, after which the fractionating effect of transverse dispersion increases reflecting the progressively more significant effect of incomplete mixing in the void space of the porous medium (e.g., Klenk and Grathwohl, 2002; Rolle et al., 2012).

3.2.2 Heterogeneous field scale

In order to assess the effect of heterogeneous flow fields on mixing-controlled bioreactive transport and on the spatial patterns of isotopic signals, we perform field-scale simulations using different hydraulic conductivity fields. Figure 3.9 shows the streamlines (gray lines) and the simulated outline of a steady-state plume resulting from the continuous release of ethylbenzene (black line) for a single realization of a random binary conductivity field for a K-ratio of 10.

In Figure 3.10, the remaining fraction of the injected ethylbenzene mass flux is plotted for individual K-fields with three different conductivity ratios between the inclusions and the matrix of 2, 10, and 50. Mixing enhancement in the high-permeability inclusions leads to a step-like profile of the remaining contaminant fraction f: a steep decrease of f occurs in zones of the domain where biodegradation is enhanced by effective mixing due to flow-focusing of the plume fringe in high-permeability inclusions. As shown in Figure 3.10, increasing the permeability contrast between the matrix and

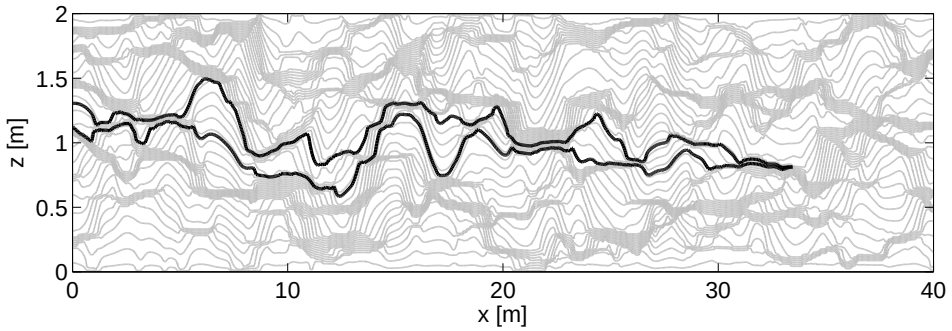

Figure 3.9: *Simulation results for a heterogeneous field-scale simulation with binary conductivity field (K_{ratio}=10); gray lines: streamlines; black line: outline of the ethylbenzene plume, defined as contour-line for 1 % of the source zone concentration.*

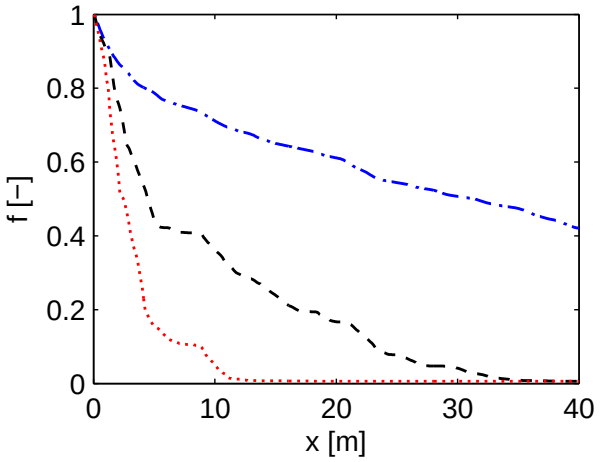

Figure 3.10: *Remaining fraction of injected ethylbenzene mass flux as function of distance from inflow boundary in the heterogeneous field-scale simulations; blue dash-dotted line: $K_{ratio} = 2$; black dashed line: $K_{ratio} = 10$; red dotted line: $K_{ratio} = 50$.*

the high-permeability zones increases transverse mixing and reduces the length of the ethylbenzene plume.

Effect of heterogeneity on isotope fractionation

Focusing of the plume fringe in high-permeability zones also affects the spatial pattern of the isotopic signature. In analogy to the analysis performed at the laboratory scale, we present two different scenarios considering no fractionating effects of the physical processes and including isotopologue-specific transverse dispersion. We consider different degrees of heterogeneity, generating the binary conductivity fields using K-ratios of 2, 10, and 50 between the matrix and the high-permeability inclusions. Reactive-transport

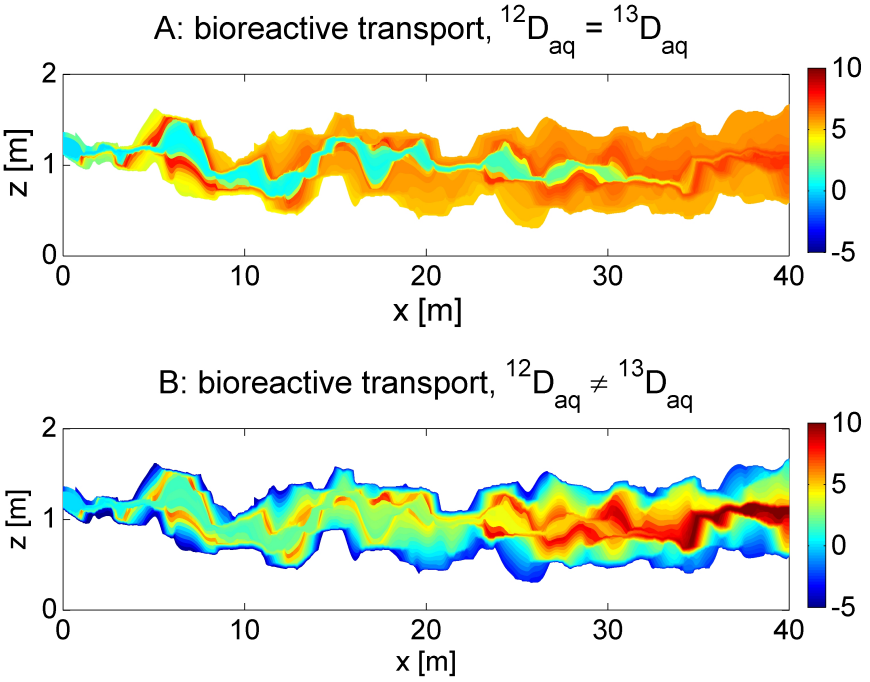

Figure 3.11: *$\Delta^{13}C$-distribution [‰] in the heterogeneous field-scale model domain for $K_{ratio} = 10$. A: bioreactive transport neglecting isotopologue-specific dispersion, B: bioreactive transport considering isotopologue-specific dispersion.*

simulations are performed with the same kinetic parameters used in the laboratory-scale simulations.

Figure 3.11 shows the spatial distribution of Δ^{13}C-values in the heterogeneous domain with a K-ratio of 10, neglecting (panel A) and considering (panel B) isotopologue-specific transverse dispersion. Flow focusing and de-focusing in the heterogeneous flow field determine a vertical squeezing and stretching of the Δ^{13}C-distribution. The two scenarios considered still have a distinct pattern, but in contrast to the laboratory-scale simulations in a homogeneous medium, these results show that the largest Δ^{13}C-values are found at the plume fringe, where the reaction predominantly takes place, also in the case of isotopologue-specific dispersion. In fact, the repeated flow-focusing events in the high-permeability inclusions have the effect of enhancing transverse mixing (i.e. limiting its controlling role on the overall degradation) and of reducing the fractionating effect of transverse dispersion, which strongly depends on the groundwater flow velocity (see Fig. 3.8). Therefore, the fractionating effect of the bioreaction can prevail over the physical effect of dispersion. A similar pattern would have been obtained considering a smaller degree of mixing enhancement but a higher fractionation factor of the

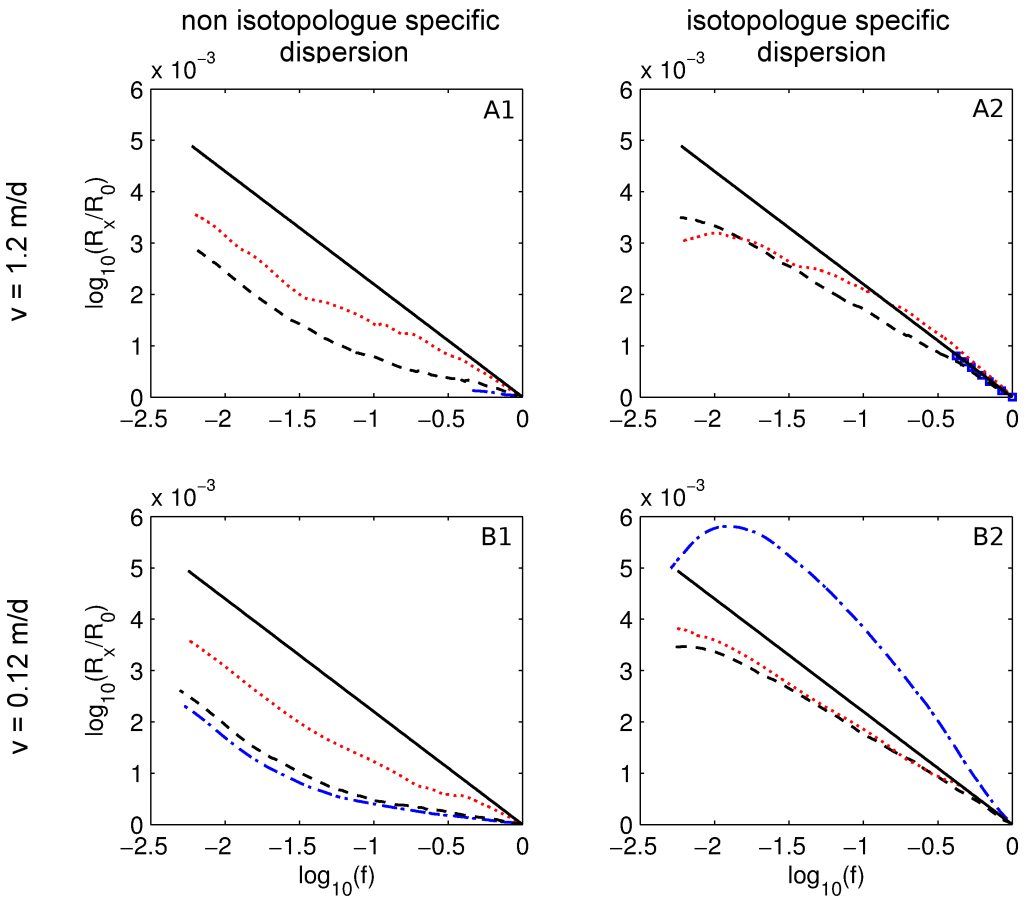

Figure 3.12: *Rayleigh plots of depth-averaged samples in the heterogeneous field-scale setup. A1 & A2: base-case seepage velocity* $v_{matrix} = 1.2\ m/d$*; B1 & B2: decreased seepage velocity* $v_{matrix} = 0.12\ m/d$*; A1 & B1: isotopologue-independent transverse dispersion; A2 & B2: isotopologue-specific transverse dispersion; blue dash-dotted line/squares:* $K_{ratio} = 2$*; black dashed line:* $K_{ratio} = 10$*; red dotted line:* $K_{ratio} = 50$*.*

bioreactive process.

Since the fractionating effect of transverse dispersion depends on the groundwater flow velocity, we performed simulations for a velocity of 0.12 m/d in the matrix and three degrees of heterogeneity (K-ratio of 2, 10, and 50) in addition to the base case velocity of 1.2 m/d. In analogy to the laboratory-scale simulations, we present the isotope ratios of the flux-averaged ethylbenzene concentration in Rayleigh plots and compare the results to the linear Rayleigh behavior. Results for a matrix velocity of 1.2 m/d (base case) are presented in Figure 3.12A1 (no fractionation by dispersion) and 3.12A2 (isotopologue-specific dispersion). Results for a matrix velocity of 0.12 m/d are presented in Figure 3.12B1 (no fractionation by dispersion) and 3.12B2 (isotopologue specific dispersion).

The results are illustrated for a single realization. However, Rayleigh plots for multiple realizations (not shown) do not qualitatively differ from the individual realizations shown in Figure 3.12.

As observed in the uniform laboratory-scale setup, non-fractionating transverse mixing causes a modulation of the isotope ratios which depart from the linear Rayleigh behavior (Figure 3.12A1 & 3.12B1) also in the heterogeneous field-scale simulations. As discussed before, this behavior can be explained by transverse mixing being rate limiting to the overall degradation of ethylbenzene. The deviation can be observed for both scenarios of the matrix velocity, but it seems to be slightly stronger for $v_{matrix} = 0.12\ m/d$ than for $v_{matrix} = 1.2\ m/d$. Increasing the degree of heterogeneity of the hydraulic conductivity fields (i.e., the contrast between the permeability of the matrix and the inclusions) increases the enhancement of mixing and therefore reduces the limiting effects of mixing on the overall contaminant degradation. As a consequence, the resulting isotope patterns show a reduced deviation from the linear Rayleigh trend. In the simulations with the smallest conductivity contrast (K-ratio of 2), biodegradation is not complete for $v_{matrix} = 1.2\ m/d$, whereas it can be considered complete (i.e., the ethylbenzene plume delimited by the 1% concentration contour does not leave the domain) for $v_{matrix} = 0.12\ m/d$. This can be attributed to the longer contact time between the reactants at slower velocities.

Figures 3.12A2 ($v_{matrix} = 1.2\ m/d$) and 3.12B2 ($v_{matrix} = 0.12\ m/d$) illustrate the effect of isotopologue-specific dispersion on the Rayleigh plot for the two different matrix velocities. As already observed in the uniform laboratory-scale setup, the profiles considering isotopologue-specific dispersion show higher values than the ones neglecting the fractionating effect of dispersion. This implies that the extent of biodegradation, calculated by equation (3.6) is always larger if isotopologue-specific dispersion is accounted for. For the seepage velocity used in the laboratory-scale simulations ($v = 1.2\ m/d$), the application of the Rayleigh equation resulted only in slight overestimation of the true extent of biodegradation (Figure 3.7). The field-scale results, however, indicate that the application of the Rayleigh equation can potentially lead to a much stronger overestimation of biodegradation if the seepage velocity is small and the flow field is only slightly heterogeneous (dash dotted line in Figure 3.12B2).

3.3 Chapter summary and conclusions

The aim of this study was to investigate the coupled effect of biodegradation and transverse dispersion on the behavior and evolution of isotope ratios in steady-state contaminant plumes. The analysis focused on fringe-controlled biodegradation of continuously emitted, oxidizable organic contaminants. The results were interpreted based on depth-integrated sampling, since standard groundwater sampling is conducted by the means of fully-screened monitoring wells.

Effect of degradation-rate limitation by mixing

The results presented in this chapter show that, similarly to other physical processes, transverse mixing can significantly bias the interpretation of observed isotope ratios. Even if transverse dispersion is considered a non-fractionating process, it can have important effects in the analysis of isotope signatures. In particular, when transverse mixing acts as rate-limiting step in contaminant degradation, applying the widely used Rayleigh equation to interpret the observed isotope ratios results in significant underestimation of biodegradation. The investigated scenarios show that these effects are more important when the rate of the reaction is relatively fast (e.g., in the presence of a readily degradable organic compound, a well-established and well-adapted microbial community, suitable environmental conditions, and thermodynamically favorable electron acceptors such as dissolved oxygen and nitrate) compared to the characteristic rate of transverse mixing. This is not uncommon, since the characteristic rate of diffusive/dispersive processes is typically very small in porous media. In particular, recent studies have pointed out the important role of diffusion for transverse mixing from the pore to the field scale (e.g. Knutson et al., 2007; Willingham et al., 2008; Chiogna et al., 2011b,a; Cirpka et al., 2011; Rolle et al., 2012). On the other hand, when the reaction can be identified as the slowest process, the limiting effect of mixing vanishes, fractionation is governed by biodegradation, and the Rayleigh equation might be applied.

We also show that the interplay between mixing and degradation varies along the length of a contaminant plume, therefore also the location where isotope ratios are measured (e.g., close to the contaminant source or farther down gradient) has an important influence on the quality of their interpretation.

For mixing-controlled reactive transport in heterogeneous conductivity fields, the spatial variability of the velocity fields leads to an enhancement of transverse mixing which

tends to attenuate the limiting effect of mass-transfer limitations by transverse dispersion to the overall degradation.

Isotope fractionation by transverse dispersion

While the rate-limiting effect of mixing alone always leads to conservative estimates of the extent of biodegradation by the Rayleigh equation, this is not necessarily the case if the fractionating effect of transverse dispersion is considered. The results of the reactive transport scenarios considering isotopologue-specific transverse dispersion point out that the effect of isotope fractionation due to the physical process depends on the fractionation strength of the reaction, on the seepage velocity and, as in the previous cases, on the interplay between mixing and biodegradation. In contrast to conservative transport, the effect of isotopologue-specific transverse dispersion is not eliminated for mixing-controlled biodegradation if isotope ratios are obtained from depth-integrated samples (fully-screened wells).

Simulations were based on aqueous diffusion coefficients for ^{12}- and ^{13}-ethylbenzene calculated by the empirical correlation for the diffusion coefficients of organic compounds of Worch (1993). This correlation was shown to accurately predict fractionation by diffusion/dispersion of deuterated and non-deuterated toluene and ethylbenzene (Rolle et al., 2010; Jin et al., 2014). The diffusion experiments of Jin et al. (2014), however, also showed a much smaller degree of *Cl* isotope fractionation for PCE and TCE than predicted by the correlation of Worch (1993). Therefore diffusion/dispersion experiments for BTEX compounds at natural isotope abundance are needed to ultimately constraint the strength of diffusive $^{13}C/^{12}C$ isotope fractionation for these contaminants.

Chapter 4

Isotope fractionation in a toluene-pulse experiment [1]

This chapter deals with the model-based analysis of a toluene-pulse experiment, performed in an indoor aquifer model at the Institute of Groundwater Ecology in Munich (Qiu et al., 2013). The goal of the experiment was to investigate the coupled effects of biodegradation, transverse dispersion, and sorption on the isotope signal of toluene under transient conditions. To this end, a two-dimensional reactive-transport model accounting for isotope fractionation by biodegradation, sorption, and transverse dispersion was developed, to aid in the interpretation of the high-resolution data set of toluene concentration and toluene-specific $\delta^{13}C$ obtained from the experiment (Qiu et al., 2013).

In a first step, the effects of individual attenuating and fractionating processes on the toluene pulse and its isotope signal were quantified by fitting the model jointly to the toluene concentration and $\delta^{13}C$ data. Based on the model fit, parameter values for individual processes were derived, and the uncertainty of these parameter values was quantified. In a consecutive step, the data were refitted with four successively simplified models, to investigate the error introduced in the interpretation of the data if individual processes (e.g., fractionation by physical processes or Michaelis-Menten kinetics) are

[1] The content presented in this chapter is adapted from from *D. Eckert, S. Qiu, M. Elsner, O.A. Cirpka (2013). Model Complexity Needed for Quantitative Analysis of High Resolution Isotope and Concentration Data from a Toluene-Pulse Experiment. Environmental Science & Technology, 47 (13), pp 6900–6907* (Eckert et al., 2013) and *S. Qiu, D. Eckert, O.A. Cirpka, M. Huenniger, P. Knappett, P. Maloszewski, R.U. Meckenstock, C. Griebler, M. Elsner (2013). Direct Experimental Evidence on Non-first Order Degradation Kinetics and Sorption-Induced Isotope Fractionation in a Mesoscale Aquifer: $^{13}C/^{12}C$ Analysis of a Transient Toluene Pulse. Environmental Science & Technology, 47 (13), pp 6892–6899* (Qiu et al., 2013). Copyright 2013 American Chemical Society.

neglected. Furthermore the the model complexity needed for the adequate description of the system was identified.

4.1 Experimental setup

The experiment was performed in a large-scale indoor aquifer model (4.83 $\times$ 0.8 $\times$ 0.7 m), filled with pristine aquifer material and flushed with natural groundwater at a rate of 240 $L\,d^{-1}$. Detailed information on the indoor aquifer model can be found in Hünniger (2011) and Herzyk (2013). A pulse of toluene and deuterated water was injected over a period of 30 h with an injection rate of 0.78 $L\,d^{-1}$ by a horizontal injection well.

Even though performed in a three-dimensional tank, the pulse experiment was effectively two-dimensional. Breakthrough curves of toluene concentration and toluene-specific $\delta^{13}C$ were measured at two different observation ports of a multilevel sampling well, denoted F2-8 and F2-9, with a vertical distance of 4 cm at 4.2 m distance from the injection point. In addition, the concentration of dissolved oxygen, which is considered to be the predominant electron acceptor for microbial respiration under the experimental conditions (i.e. pulse injection into an aerobic system) was measured at port F2-8. Compared to the inflow, significantly reduced toluene concentrations, enriched δ^{13} values and a slight depletion in dissolved oxygen could be observed at the two observation points.

The experiment was performed by Dr. Shiran Qiu under the supervision of Dr. Martin Elsner at the Institute of Groundwater Ecology at the Helmholtz Center for Environmental Health in Munich. Further information on the experiments and the measurements can be found in Qiu et al. (2013).

4.2 Model description

The toluene-pulse experiment in the indoor aquifer model was simulated along a two-dimensional vertical transect. In the model, toluene was injected with a concentration of 500 mgL^{-1} over an injection height of 2.4 mm for 30 h to simulate the experimental boundary conditions. Due to the short duration of the experiment microbial growth was neglected and toluene degradation was simulated by Michaelis-Menten kinetics. Oxygen was not explicitly considered in the model, since oxygen measurements showed

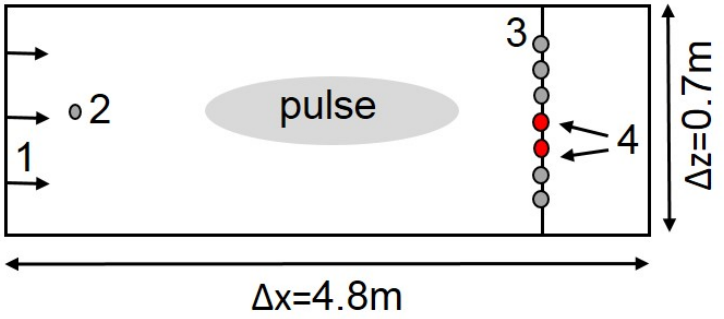

Figure 4.1: *Two dimensional illustration of the experimental setup. (1) horizontal groundwater flow, (2) pulse injection of toluene and D_2O, (3) multilevel sampling well at 4.2 m distance from the injection point, (4) observation ports F2-8 and F2-9 with spacing of 4 cm..*

that oxygen was not a limiting factor. The simulated velocity was strictly horizontal, and all model parameters were assumed spatially uniform.

Numerical methods

The domain was discretized by the cell-centered Finite Volume Method with a spatial discretization of 1 cm in the horizontal and 0.12 cm in the vertical direction. Transport and reaction were decoupled by an operator splitting approach. Integration in time was performed by the explicit Euler method for advective fluxes and the reactive sink term and by the implicit Euler method for dispersive fluxes. A time step size of 537 s was chosen to achieve a Courant number of unity. The code was written as a Matlab program and the system of linear equations for the dispersive fluxes was solved with the UMFPACK solver, implemented in Matlab (Davis and Duff, 1997).

4.3 Parameter estimation

4.3.1 Estimation of conservative transport parameters

Basic parameters describing conservative transport through the indoor aquifer model (e.g. seepage velocity, dispersion coefficients) were determined by D_2O and Br^- tracer tests performed by Qiu et al. (2013). Parameter values are presented in Table 4.1.

The seepage velocity v was chosen manually in order to match the arrival time of the D_2O peak concentration at F2-8 and F2-9 (see Fig. 4.2). The estimated velocity was

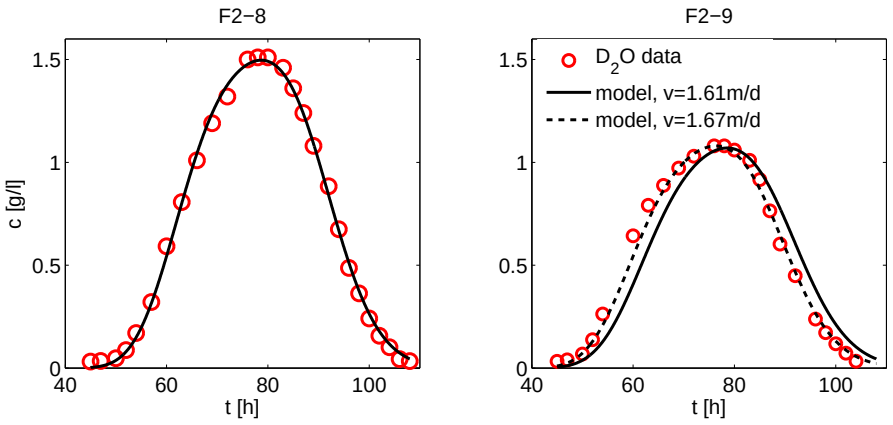

Figure 4.2: *Measured D_2O breakthrough curves for F2-8 and F2-9 and corresponding model fits.*

slightly different for F2-8 ($v = 1.61md^{-1}$) and F2-9 ($v = 1.67md^{-1}$), which indicates the presence of small-scale heterogeneity in the system (see Fig. 4.2). For the further analysis this was neglected, and a homogeneous transport velocity of $v = 1.61md^{-1}$ was assumed.

Subsequently, the longitudinal dispersion coefficient D_L was obtained by fitting the measured D_2O breakthrough curve at F2-8, which is located at a distance of x=4.2m from the horizontal injection well, with the one-dimensional analytical solution for the given injection time tin of 30 hrs:

$$c(x,t) = \frac{c_{steady}}{2}\left(erfc\left(\frac{x-vt}{2\sqrt{D_L t}}\right) - erfc\left(\frac{x-v(t-t_{in})}{2\sqrt{D_L(t-t_{in})}}\right)\right), \tag{4.1}$$

in which c_{steady} is the concentration at F2-8 that would be obtained for a continuous injection of D_2O at a sufficiently long time and D_L is the longitudinal dispersion coefficient. Both c_{steady} and D_L were fitting parameters. Fitting c_{steady} was needed to account for (1) the mass loss due to transverse dispersion and (2) the possibility that the pulse center may not necessarily hit sampling port F2-8. We estimated the flow-effective porosity n_e based on the measured groundwater flow rate Q and the fitted seepage velocity.

The transverse dispersion coefficient D_t was evaluated by fitting a bromide tracer test performed by Qiu et al. (2013), where bromide was continuously injected and vertical concentration profiles were measured (Fig. 4.3). Fitting the data with the 2-D steady-state analytical solution for continuous solute injection (with inflow concentration c_{in}) from a line source of width w, we could estimate the transverse dispersion coefficient

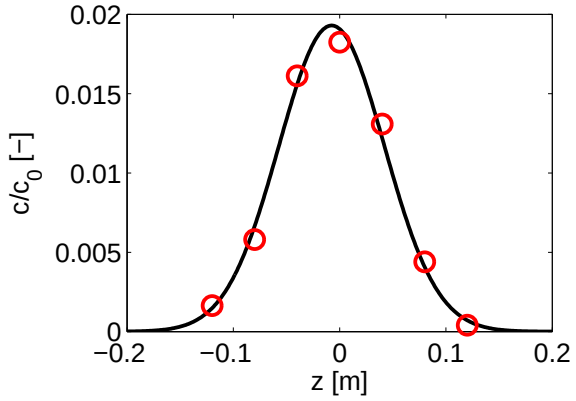

Figure 4.3: *Measured vertical profile of Br^- concentration for well F2 under steady state transport conditions during a long term injection experiment and corresponding model fit.*

of bromide:

$$c(x,z) = \frac{c_{in}}{2}\left(erf\left(\frac{z+\frac{w}{2}}{2\sqrt{D_T\frac{x}{v}}}\right) - erf\left(\frac{z-\frac{w}{2}}{2\sqrt{D_T\frac{x}{v}}}\right)\right), \tag{4.2}$$

The D_t-value determined for bromide was transferred to the transverse dispersion coefficients of D_2O and toluene based on the differences in the aqueous diffusion coefficients as reported in Table 4.1, using a non-linear parameterization of D_t that accounts for compound-dependent mechanical dispersion (Chiogna et al., 2010):

$$D_t = n_e D_{aq} + v\frac{d_{eff}}{\sqrt{\frac{vd_{eff}}{D_{aq}} + 123}}, \tag{4.3}$$

in which n_e is the effective porosity, D_{aq} is the aqueous diffusion coefficient, and d_{eff} is the effective grain size of the natural sediment used to fill the indoor aquifer model. The vertical offset z_{off} of sampling ports F2-8 and F2-9 to the pulse center was subsequently obtained by solving equation 4.2 for z, applying $c(z_{off}) = c_{steady}$, the steady-state concentrations for F2-8/F2-9 estimated by equation 4.1.

4.3.2 Parameter estimation strategy for reactive transport

Reactive-transport parameters (i.e., biokinetic parameters r_{max} and K_{tol}, the retardation factor R, isotopic enrichment factors ε_r^{kin}, ε_s^{equ} and ε_D^{kin}) and the corresponding uncertainties of the estimated parameters, were obtained by simultaneously fitting the reactive-transport model described above to the measured toluene concentration and

Table 4.1: *Fitted parameters for conservative transport.*

Transport Parameters			
v	$[ms^{-1}]$		1.86×10^{-5}
n_e	$[-]$		0.268
D_L	$[m^2s^{-1}]$		5.2×10^{-7} [e]
D_T	$[m^2s^{-1}]$	D_2O	5.7×10^{-9}
		$toluene$	4.9×10^{-9}
Intermediate Parameters			
D_{aq} at 15°C	$[m^2s^{-1}]$	Br^-	1.6×10^{-9} [a]
		D_2O	1.7×10^{-9} [b]
		$toluene$	0.8×10^{-9} [c]
D_t	$[m^2s^{-1}]$	Br^-	5.7×10^{-9}
d_{eff}	$[m]$		3.7×10^{-3}
c_{in}	$[mgL^{-1}]$	D_2O	2.1×10^5
		$toluene$	500
c_{steady}	$[mgL^{-1}]$	$F2-8$	1.56×10^3
		$F2-9$	1.13×10^3
z_{off}	$[m]$	$F2-8$	0.068
		$F2-9$	0.079

[a] Cussler (2009).
[b] D_{aq} of D_2O approximated by value for HTO reported in Mills (1973).
[c] Calculated by empirical correlation of Worch (1993).

toluene-specific $\delta^{13}C$ breakthrough curves at the two sampling ports F2-8 and F2-9 at 4.2 m distance from the horizontal injection well.

The model was fitted to the data by minimizing the sum of normalized squared errors ($SNSE$) between measured and simulated concentration and $\delta^{13}C$ breakthrough curves at both sampling ports:

$$SNSE = SNSE_{tol} + SNSE_{\delta^{13}C} \tag{4.4}$$

$$SNSE_{tol} = \frac{\sum_{i=1}^{n_c} \left(c_i^{meas} - c_i^{sim}\right)^2}{\sigma_c^2} \tag{4.5}$$

$$SNSE_{\delta^{13}C} = \frac{\sum_{i=1}^{n_\delta} \left(\delta^{13}C_i^{meas} - \delta^{13}C_i^{sim}\right)^2}{\sigma_{\delta^{13}C}^2}, \tag{4.6}$$

in which σ_c^2 is the variance in the observed toluene concentrations and $\sigma_{\delta^{13}C}^2$ the variance in the isotope ratio data, n_c is the total number of concentration measurements (i.e., at both sampling ports) and n_δ the total number of isotope ratio measurements.

The corresponding uncertainty in the fitted parameters was estimated based on linearized error propagation Press et al. (1997):

$$C_{pp} = f \times \left(J^T C_{meas}^{-1} J\right)^{-1}, \tag{4.7}$$

in which C_{pp} is the covariance matrix of the parameter uncertainties, J is the Jacobian matrix, containing the partial derivatives of the model outcome with respect to each reactive transport parameter, C_{meas} is a diagonal matrix containing the variance in the concentration (σ_c^2) and isotope ratio ($\sigma_{\delta^{13}C}^2$) measurements along the main diagonal, and $f = SNSE/(n_{obs} - n_p)$ is a scaling factor to achieve the expected value of the objective function for an accepted model, in which n_{obs} is the number of observations and n_p is the number of parameters.

4.4 Results and discussion

4.4.1 Experimental data and model fit

Figure 4.4 shows measured and simulated breakthrough curves (BTCs) of D_2O (green crosses, green dashed line), toluene (black circles, black solid line) and the toluene-specific stable-carbon isotope ratio (red squares, red solid line) at the two sampling ports F2-8 and F2-9. Simulated isotope ratios are only plotted for toluene concentrations above the detection limit for standard GC-IRMS measurements ($5 \mu g L^{-1}$). The toluene peak arrives approximately 20 hrs later than the D_2O peak and the normalized peak concentration is much lower for toluene than for the conservative tracer D_2O. We interpret these observations by toluene undergoing sorption and biodegradation while being transported through the indoor aquifer model.

Based on a comparison of the zeroth temporal moments of the toluene BTC (black solid line) and the D_2O BTC (green dashed line), the extent of biodegradation (B) was quantified for sampling ports F2-8 (B = 37%) and F2-9 (B = 44%). Similar to the Rayleigh-equation-based quantification of biodegradation from local isotope ratio measurements, this approach yields location dependent values for B. The small difference

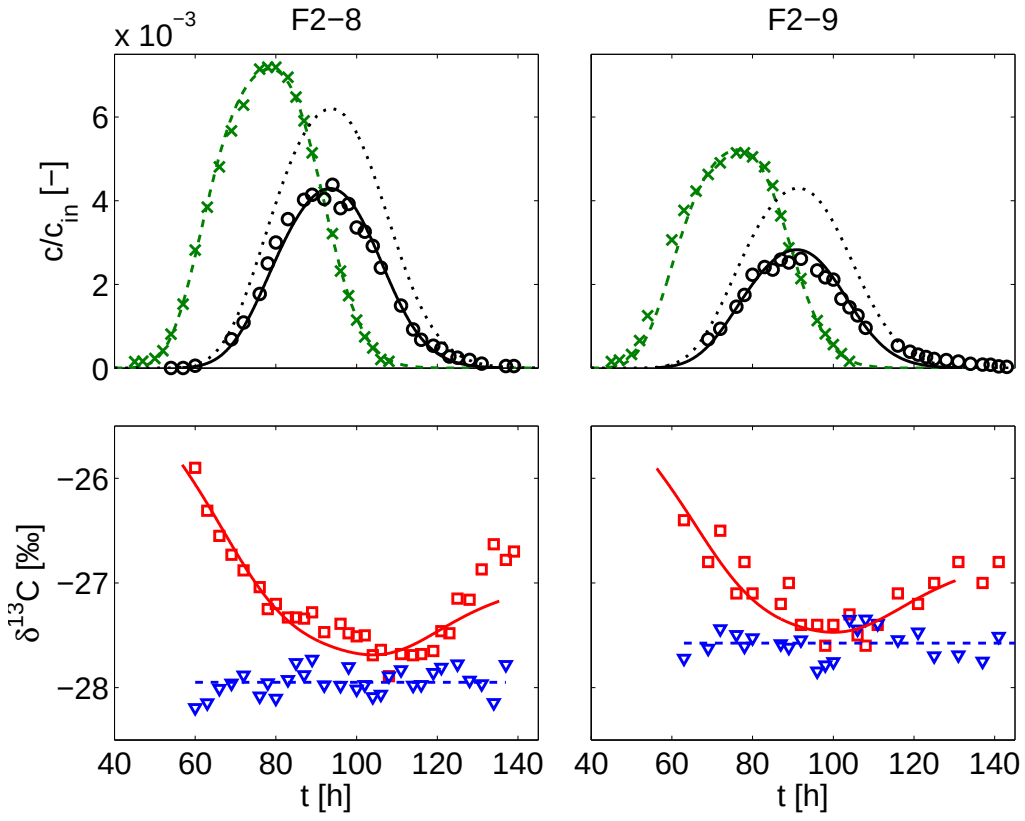

Figure 4.4: *Measured breakthrough curves of D_2O (green crosses), toluene (black circles) and toluene-specific $\delta^{13}C$ (red squares) at the two sampling ports F2-8 and F2-9 at x=4.2m, toluene-specific $\delta^{13}C$ (blue triangles) at the inflow, corresponding model fits (lines) and model prediction for conservative toluene transport (black dotted line).*

in B for the two sampling ports likely arises from the fact that in relative terms degradation is stronger for the lower toluene concentration encountered at F2-9, which is in accordance with Michaelis-Menten kinetics. Performing a mass balance on the model results, in which we compared the simulated toluene mass passing through transect F to the injected toluene mass, we estimated that 26 % of the injected toluene mass was degraded at transect F. This indicates that estimates of B, which are based on point observations (i.e. isotope measurements at individual ports of a multilevel sampling well), are not necessarily representative of the overall extent of biodegradation.

Our model is able to reproduce the asymmetric U-shape of the $\delta^{13}C$ BTCs observed at F2-8 and F2-9 (figure 4.4). The U-shape arises from the fact that in relative terms stronger degradation, and hence isotopic enrichment, is taking place at the fringes of the toluene pulse. The asymmetry of the $\delta^{13}C$ BTCs results from sorption-induced

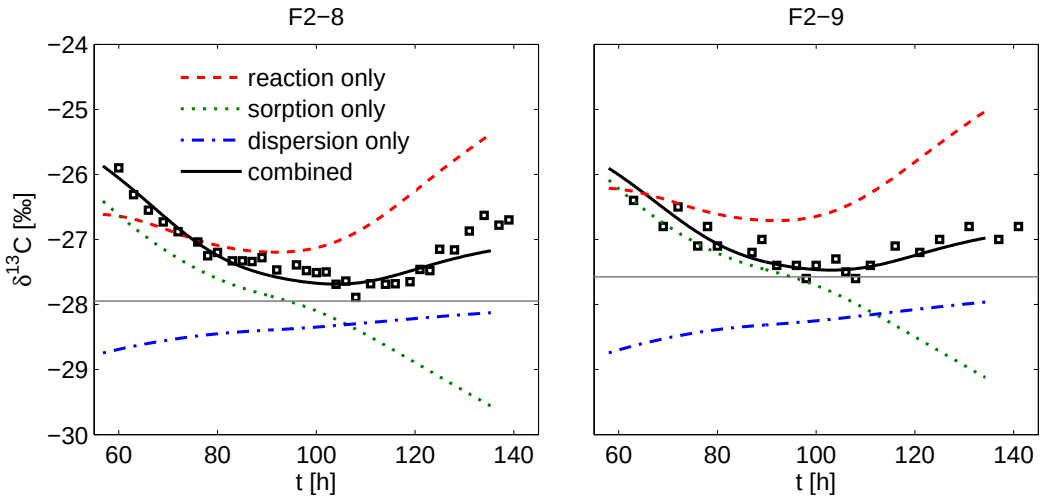

Figure 4.5: *Experimentally observed carbon isotope trends, and simulated trends resulting from the various fractionation processes. The gray horizontal line indicates the initial $\delta^{13}C$ value.*

isotope fractionation. As expected, slightly stronger sorption of the light isotopologues (Kopinke et al., 2005) increases the enrichment in $\delta^{13}C$ values due to biodegradation at the front end of the toluene pulse (early times) and reduces the enrichment at the back end (late times). The effect of transverse dispersion on the isotope signal, which is less obvious than the effect of sorption, is manifested in the fact that the general isotopic enrichment is slightly larger for F2-8 than for F2-9, which is further away from the pulse center. Due to the slightly larger aqueous diffusion coefficient of the light isotopologues (Rolle et al., 2010), transverse dispersion is leading to progressively less enriched $\delta^{13}C$-values away from the center of the toluene pulse.

Effect of individual fractionation processes

In order to visualize the effect of each individual process on the observed $\delta^{13}C$ breakthrough, additional simulations were run, in which isotope fractionation by individual processes was switched on and off. Results are shown in Figure 4.5. Except for the front end of the pulse, the effect of sorption and transverse dispersion reduces the isotope enrichment that would be expected due to biodegradation alone. At the front end of the pulse, however, the model predicts that sorption alone would almost cause the same isotope enrichment as the coupled processes do. Isotope enrichment at the invading front of a contaminant plume by sorption might, therefore, wrongly be interpreted as evidence for the occurrence of biodegradation.

Table 4.2: *Fitted reactive-transport parameters, corresponding relative uncertainties (σ/p) and correlation between individual parameter uncertainties.*

	Parameter value	**Rel. σ**	**Correlation matrix**					
			$\mathbf{r_{max}}$	$\mathbf{K_{tol}}$	$\mathbf{R_{tol}}$	ε_r^{kin}	ε_s^{equ}	ε_D^{kin}
$\mathbf{r_{max}}$ $[mgL^{-1}s^{-1}]$	1.2×10^{-5}	8%	1	0.71	0.07	-0.17	-0.22	-0.58
$\mathbf{K_{tol}}$ $[mgL^{-1}]$	2.2	12%		1	0.07	-0.75	-0.29	-0.74
$\mathbf{R_{tol}}$ $[-]$	1.25	1%			1	0.04	0.62	-0.04
ε_r^{kin} [‰]	-2.15	10%				1	0.52	0.77
ε_s^{equ} [‰]	-0.31	7%					1	0.62
ε_D^{kin} [‰]	-0.82	12%						1

Calibrated model parameters

Calibrated reactive-transport parameters and their relative uncertainties (σ_p/p) are presented in Table 4.2. The estimated isotope enrichment factor for toluene degradation with a value of -2.15‰ is in agreement with the range of values (-0.4 to -3.3‰) reported in the literature (Vogt et al., 2008). The isotope effect due to equilibrium sorption of -0.31‰, estimated by fitting the model to the data, qualitatively agrees with the values reported by Kopinke et al. (2005) and Hoehener and Yu (2012). The enrichment factor of -0.82‰ estimated for transverse dispersion is qualitatively consistent but smaller than the value of -1.4‰ calculated based on the empirical correlation for the aqueous diffusion coefficients of organic compounds of Worch (1993). As already mentioned in the last chapter, experiments of toluene diffusion/dispersion in aqueous solution without biodegradation and sorption will be necessary to further constraint this number. The relative uncertainties for the calibrated biokinetic parameters r_{max} and K_{tol} and for the isotope enrichment factors for biodegradation, equilibrium sorption, and transverse dispersion fall in the range of 7-12 %, indicating that all parameters can be determined quite uniquely based on the joint model fit to the concentration and $\delta^{13}C$ measurements.

Performance of the Rayleigh equation

To check the performance of the Rayleigh equation, I applied it with the fitted enrichment factor for biodegradation $\varepsilon_r^{kin} = -2.15$‰ . The extent of biodegradation estimated by the Rayleigh equation $B_{Rayleigh}$ and the actual extent of biodegradation B_{true} are calculated according to equations 3.6 and 3.7 and their ratio is plotted in Fig. 4.6.
The Rayleigh equation overestimates the real extent of biodegradation by almost 50%

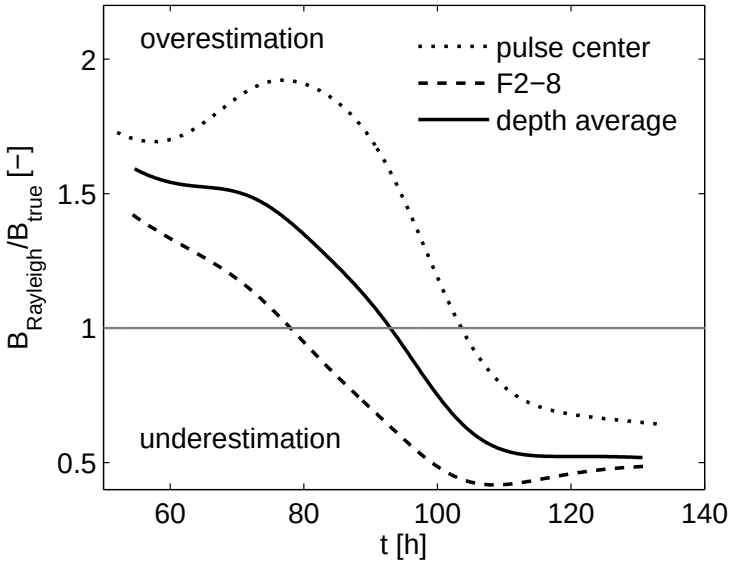

Figure 4.6: *Comparison of the extent of biodegradation estimated by the Rayleigh equation $B_{Rayleigh}$ to the actual extent of biodegradation B_{true} for point measurements (pulse center and port F2-8) and depth-integrated sampling.*

if the invading front of the pulse is sampled at port F2-8, whereas biodegradation is underestimated at the tail of the pulse. Due to isotope enrichment by transverse dispersion, overestimation of biodegradation by the Rayleigh equation is stronger if samples are taken from the center of the pulse, than for depth integrated (fully-screened well) samples and samples taken at the fringes of the pulse (e.g., port F2-8).

4.4.2 Consistency check with oxygen data

Under the conditions of the toluene-pulse experiment, i.e., a pulse injection into an aerobic aquifer, oxygen is considered to be the predominant electron acceptor for microbial respiration. The fact that 26 % of the incoming toluene mass flux was degraded at transect F should therefore be reflected in the consumption of dissolved oxygen. Dissolved oxygen concentrations recorded at sampling port F2-8 show a slight depletion during the course of the experiment (Figure 4.7, red squares). In order to test whether this depletion in dissolved oxygen concentrations is sufficient to explain the observed extent of toluene degradation, oxygen was included as an additional species

in the reactive-transport model. The rate of oxygen consumption due to toluene degradation, r_{ox} $[MT^{-1}L^{-3}]$, was calculated by:

$$r_{ox} = f_{ox} \times r. \tag{4.8}$$

Measured (red squares) and simulated oxygen profiles (red lines) at the sampling port F2-8 are presented in figure 4.7. The measured depletion in oxygen is significantly retarded compared to the toluene pulse (black crosses). If the model does not account for the retardation of oxygen (red dashed line), the maximum depletion in dissolved oxygen observed at sampling port F2-8 is strongly over predicted. Oxygen retardation is most likely caused by entrapped gas in the indoor aquifer model. Due to the high tendency of oxygen to partition into the gas phase, a small amount of entrapped gas can lead to significant retardation. Retardation of oxygen due to water-gas partitioning can be described by the retardation factor R_{ox} (Fry et al., 1995):

$$R_{ox} = 1 + \frac{S_g H}{1 - S_g}, \tag{4.9}$$

in which S_g [-] is the residual gas saturation in the pore space and H [-] is the dimensionless Henry's Law constant ($H = c_g/c_w$) with a value of 28 for oxygen at $15°C$ (Fry et al., 1995). It turned out that a retardation factor of approximately 4 is needed in order to match the arrival time of the oxygen depletion in sampling port F2-8 (red solid curve in 4.7). This retardation factor implies a residual gas saturation of 10 % in the indoor aquifer model, which compares well with literature values for gas entrapment due to water level fluctuations and when filling porous media (Fry et al., 1997). Retardation of toluene due to gas-water partitioning ($H_{tol} = 0.163$ [-] at $15°C$) was found to be insignificant for a gas saturation of 10 %.

Even when oxygen retardation is accounted for in the model (red dash-dotted line in figure 4.7), the observed depletion in dissolved oxygen at sampling port F2-8 is slightly overestimated if the stoichiometric coefficient for complete toluene mineralization ($fox = 3.1\ mg_{O_2}/mg_{tol}$) is assumed. A good fit is achieved with $f_{ox} = 1.5$, suggesting that toluene might have been not completely mineralized to carbon dioxide and water during the course of the pulse experiment. In Appendix B, we speculate on possible metabolites and the degree of incomplete degradation.

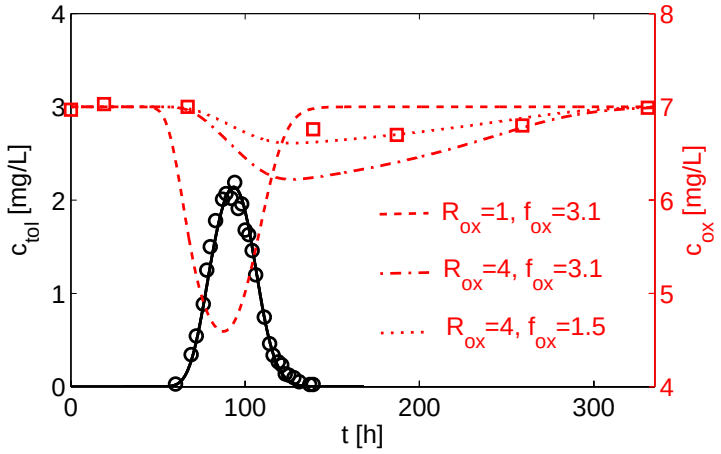

Figure 4.7: *Measured and simulated breakthrough curves of toluene and oxygen at port F2-8. Black circles: measured toluene; black solid line: simulated toluene; red squares: measured oxygen; red dashed line: simulated oxygen assuming no oxygen retardation ($R_{ox} = 1$) and complete toluene mineralization ($f_{ox} = 3.1$); red dash-dotted line: simulated oxygen assuming oxygen retardation ($R_{ox} = 4$) and complete toluene mineralization ($f_{ox} = 3.1$); red dotted line: simulated oxygen assuming oxygen retardation ($R_{ox} = 4$) and incomplete toluene mineralization ($f_{ox} = 1.5$).*

4.4.3 Which model complexity is needed?

The high-resolution data set of toluene concentrations and isotope ratios ($\delta^{13}C$) from the toluene pulse experiment enabled us to develop and calibrate a reactive-transport model representing a certain degree of complexity. With this model we could uniquely quantify toluene degradation and sorption and separate the effects of degradation-, sorption- and transverse-dispersion-induced isotope fractionation on the isotopic signal of toluene. For field-scale contaminant plumes, however, concentration and especially isotope-ratio data with a high temporal and/or spatial resolution are only available for a very limited number of research sites (Anneser et al., 2008; Hunkeler et al., 2004). Quantifying intrinsic biodegradation at contaminated sites by CSIA is commonly performed by applying the Rayleigh equation to individual $\delta^{13}C$ point measurements (Richnow et al., 2003; Sherwood Lollar et al., 2001). The lack in highly resolved data for most contaminated sites might make it impossible to calibrate reactive-transport models accounting for the same complexity as outlined here. Too simplistic reactive-transport models and/or analytical tools such as the Rayleigh equation, however, might in turn fail in giving reliable

predictions if they do not at least capture the dominant processes.

In this section, we systematically investigate the error introduced in the interpretation of the toluene-pulse experiment if individual processes are neglected or simplified in our model. Therefore, we refit the experimental data of Qiu et al. (2013) with four successively simplified reactive-transport models, and compare the results to the full model. Table 4.4 shows the fitted toluene concentration and $\delta^{13}C$ BTCs, estimated parameter values and relative parameter uncertainties of the full model A and the four simplified models B-E together with the sum of normalized squared errors (SNSE) as measure for the goodness of fit for each model. The SNSE measures are split into the part representing the fit of the concentration BTC and the isotope ratios, respectively.

The full model (model A) accounts for Michaelis-Menten reaction kinetics and equilibrium sorption as well as reaction-, sorption- and transverse- dispersion-induced isotope fractionation. In the following description of the four successively simplified models, only additional simplifications introduced in the current model are mentioned. In model B, isotope fractionation is neglected at all and the model was fitted solely to the toluene concentration data. This scenario is representative for most field applications of reactive transport modeling. Isotope measurements are only available for a limited number of sites and hence commonly the quantification of biodegradation is based on concentration measurements only. In model C, biodegradation and sorption but not transverse dispersion are considered to fractionate between light and heavy toluene isotopologues. In Model D, biodegradation is assumed to be the only fractionating process as it is frequently assumed in Rayleigh-based analysis of isotopic signatures (Richnow et al., 2003; Sherwood Lollar et al., 2001; Fischer et al., 2007). In model E, the concentration-dependence of biodegradation kinetics is neglected and biodegradation is described as first-order process.

The strong correlation between the biokinetic parameters r_{max} and K_{tol} makes it generally difficult to obtain a unique and reliable set of parameter values from concentration measurements alone. This is manifested in the large uncertainties for the estimates of r_{max} (33%) and K_{tol} (51%) by model B. In batch biodegradation experiments, this problem may be overcome by performing experiments with different initial contaminant concentration (Schirmer et al., 1999), which is not possible for the calibration of field-scale models. However, using isotope data in addition to concentration data for model calibration (model A) has a similar effect and leads to more reliable parameter values. This is reflected in significantly reduced parameter uncertainties (r_{max} : 8%, K_{tol} : 12%).

The U-shape of the $\delta^{13}C$ BTCs results from the transition between zero-order degradation kinetics in the pulse center (high toluene concentration) and first-order kinetics at the fringes (low toluene concentration) of the pulse, and hence is very sensitive to the actual parameter values of r_{max} and K_{tol}. Note that the goodness of fitting the concentration BTC is somewhat better for model B, neglecting the isotope data (*SNSE* for toluene 0.63), than for model A (*SNSE* for toluene 0.8), indicating trade-off effects in fitting both concentrations and isotope ratios.

Assuming transverse dispersion to be insensitive to the isotopic composition of toluene (model C), the asymmetric U-shape of the $\delta^{13}C$ BTCs can still be reproduced, while the observed overall isotopic enrichment at sampling port F2-9 is slightly overestimated. With a total *SNSE* value of 14.2, the goodness of fit is less satisfying than for model A (total *SNSE*: 9), in which isotopologue-specific transverse dispersion is accounted for. The decline in model performance is mainly attributed to fitting the $\delta^{13}C$ BTCs less accurately (*SNSE* for $\delta^{13}C$ of 13.1 rather than 8.2). Even though the effect of isotope fractionation by transverse dispersion is not directly visible from the $\delta^{13}C$ BTCs at F2-8 and F2-9, it has a strong effect on the estimated value of the enrichment factor for biodegradation (ε_r^{kin}), whose value for model A ($-2.15‰$) is more than two times larger than for model C ($\varepsilon_r^{kin} = -1‰$). While having no effect on the shape of the individual $\delta^{13}C$ BTCs at sampling ports F2-8 and F2-9, isotope fractionation by transverse dispersion is shifting the profiles towards smaller $\delta^{13}C$ values with increasing distance to the pulse center. Due to the small effective distance of 1.1 cm between the two sampling ports F2-8 and F-9 the shift in $\delta^{13}C$ BTCs between F2-8 and F2-9 is small.

Neglecting the fractionating effect of sorption in addition to the one of transverse dispersion (model D), the observed asymmetry in the $\delta^{13}C$ BTCs can no more be reproduced, and the overall goodness of the fit is poor (value of 56.4 for the total SNSE, mainly attributed by a bad fit of the $\delta^{13}C$ BTCs). In contrast to the data, simulated $\delta^{13}C$-profiles show a minimum at the toluene peak concentration. The simulated isotopic enrichment at the front end of the pulse is strongly underestimating the measured extent of isotopic enrichment, which clearly shows that sorption-induced isotope fractionation has to be considered in the model to adequately describe the system. The inability of model D to capture the shape of the observed $\delta^{13}C$ BTCs is also reflected in the overestimation of toluene retardation by the model.

Finally, model E describes biodegradation as a first-order process. This model can no more reproduce the observed U-shape of the $\delta^{13}C$ BTC. By neglecting the non-linear dependence of the degradation rate on concentration, model E cannot reproduce the

observed difference in isotopic enrichment between the pulse center and the fringes. Consequently, the simulated isotopic enrichment increases linearly with the time that toluene has stayed in the system and undergone degradation with constant isotope fractionation. In contrast to the $\delta^{13}C$ BTCs (SNSE for $\delta^{13}C$ of 62), the toluene concentration BTCs are matched even slightly better by the first-order model E than by the full model (*SNSE* for toluene of 0.7 versus 0.8). Therefore, it might be sufficient to use first-order kinetics to describe the reduction in contaminant concentration by biodegradation if the total loss of toluene is the primary target of the model.

4.4.4 Continuous toluene injection

After completion of the pulse experiment, a second experiment, in which toluene was continuously introduced into the indoor aquifer model, was performed at the Institute of Groundwater Ecology in Munich. In this second experiment, toluene was injected at a concentration of 500 mgL^{-1} over a period of 133 days. On the last day, 200 *ml* of pure phase toluene were introduced within six hours and toluene injection was switched of afterwards. Four days after injection of the pure-phase toluene, vertical profiles of toluene and oxygen concentrations as well as the toluene-specific $\delta^{13}C$ signature were measured at four different transects of the indoor aquifer, at a vertical spatial resolution of 4 *cm*. Further information on the indoor aquifer model can be found in Hünniger (2011). The continuous toluene-injection experiment was performed and analyzed in detail by Dr. Agnieszka Monika Herzyk as part of her PhD thesis (Herzyk, 2013).

In contrast to the toluene-pulse experiment, oxygen was a limiting factor for toluene degradation during the continuous-injection experiment and biodegradation activity was focused at the fringe of the toluene plume. Toluene degradation was simulated by dual Michaelis-Menten kinetics to account for the presence of oxygen as limiting factor. The presence and the dissolution of pure-phase toluene was not explicitly considered in the model. To obtain the correct toluene mass flux leaving the source zone, the effective source width was increased in the model from 2.4 (pulse experiment) to 7 *mm*, in order to match the toluene concentration profile at the first transect (A) at a distance of $x = 0.2m$.

Figure 4.8 depicts the measured and simulated depth-profiles of toluene and oxygen concentrations (upper and mid panel) and toluene-specific ^{13}C enrichment (lower panel) for four different distances from the inflow. Simulations were performed with the isotope enrichment factors for biodegradation ($\varepsilon_r^{kin} = -2.15‰$) and transverse dispersion

($\varepsilon_D^{kin} = -0.82‰$) obtained from the pulse experiment. Sine the toluene plume could be expected to have reached a steady state after toluene injection for 133 days, sorption was not expected to affect the toluene concentration and $\delta^{13}C$ distributions. Parameter values applied in the model are listed in Table 4.3. The maximum reaction rate r_{max} had to be increased by a factor of 20, as compared to the pulse experiment, in order to match the toluene, oxygen and $\delta^{13}C$ profiles.

Simulations were run for three different scenarios: isotope fractionation by biodegradation and transverse dispersion (solid black line), isotope fractionation by biodegradation only (blue dotted line) and isotope fractionation by dispersion only (green dashed line). The maximum observed isotope enrichment was around $1‰$. The simulation results predict steep isotope-ratio profiles at the plume fringe. This suggests that even for the high spatial sampling resolution (port spacing of 4 *cm*), observed isotope ratios might be strongly effected by dilution due to non-point sampling.

Comparing the simulation results for toluene and a hypothetical conservative tracer with the same physical properties as toluene (upper panel of figure 4.8), it is clear that toluene concentration measurements alone do not give any indication for the occurrence of biodegradation. The strong oxygen depletion in the plume core (mid panel) and the observed isotope enrichment at the fringe (lower panel), in contrast, show strong evidence for the occurrence of fringe-controlled toluene degradation.

A visual comparison of observed and simulated isotope ratios indicates that isotope fractionation in the indoor aquifer model was mainly dominated by fringe-controlled biodegradation, which leads to isotope enrichment at the plume fringe, rather than transverse dispersion, which would lead to the depletion of ^{13}C at the plume fringe. Similar isotope ratio profiles for toluene, i.e. isotopic enrichment at the plume fringe of around 3 to $4‰$ and almost no enrichment in the plume core, were observed at a BTEX contaminated field site (Prommer et al., 2009). While overall isotope fractionation might be dominated by transverse dispersion close to the inflow (transect A), as suggested by the simulation results, its effect on the isotope signal of toluene decreases with travel distance.

Figure 4.9 shows a comparison of the extent of biodegradation estimated by the Rayleigh approach and the extent of biodegradation obtained from the model (left subplot) as well as the extent of over-/underestimation of biodegradation by the Rayleigh approach (right subplot). Results are given for depth-integrated sampling by a fully screened monitoring well. The model predicts that about 20% of the toluene mass flux leaving

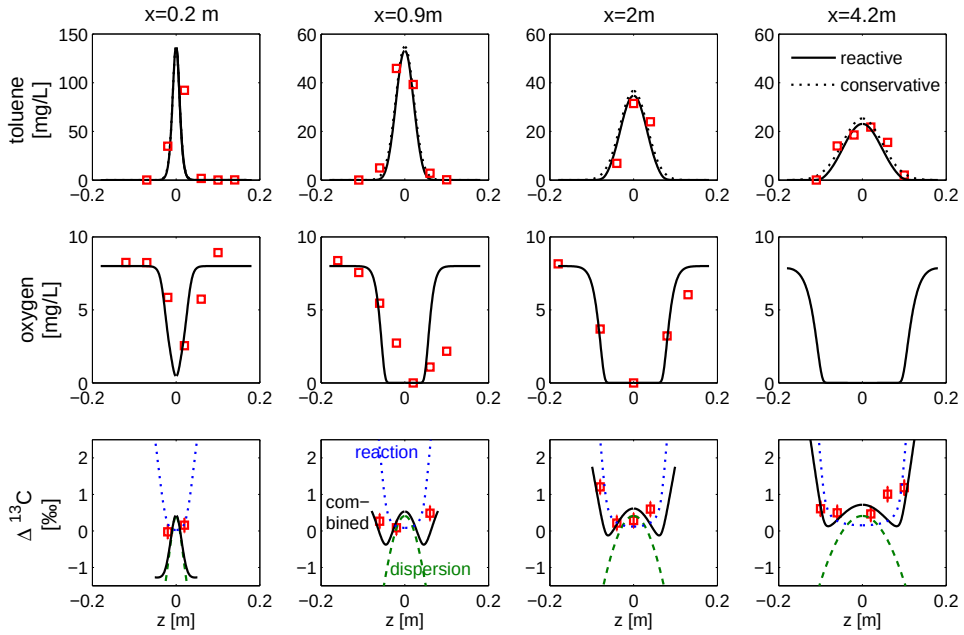

Figure 4.8: *Measured and simulated depth profiles of toluene concentration (upper panel), oxygen concentration (mid panel) and toluene-specific ^{13}C enrichment ($\Delta^{13}C$) at different distances from the inflow (lower panel).*

the source zone is degraded withing a travel distance of $4.2m$. The extent of biodegradation is overestimated by the Rayleigh equation between 15 and 30%, depending on the distance from the source zone. The overestimation decreases with increasing travel distance. Simulation results for the scenario where isotopologue independent transverse dispersion was considered (right subplot) indicate that the overestimating effect due to isotope fractionation by transverse dispersion is balanced to a large extent by the effect of mass-transfer limitations in fringe-controlled biodegradation on the isotope signal, so that the Rayleigh equation in the end gives a reasonable prediction. For a detailed analysis on the effect of mass-transfer limitations on isotope fractionation in fringe-controlled biodegradation please see chapter 3.

Table 4.3: *Parameters used to simulate the continuous toluene-injection experiment.*

r_{max} $[mgL^{-1}s^{-1}]$	K_{tol} $[mgL^{-1}]$	K_{ox} $[mgL^{-1}]$	ε_r^{kin} [‰]	ε_D^{kin} [‰]
2.4×10^{-4}	2.2	0.32[a]	−2.15	−0.82

[a] Bauer et al. (2009a)

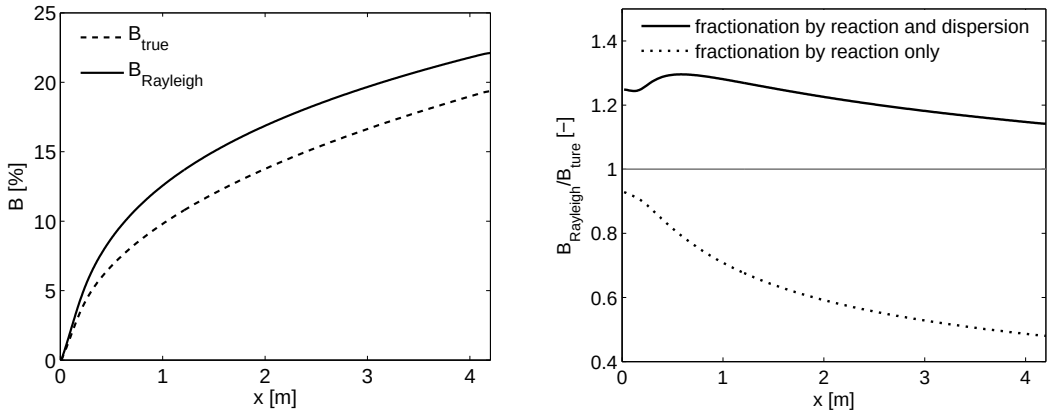

Figure 4.9: *Left subplot: comparison of the extent of biodegradation B estimated by the Rayleigh equation ($B_{Rayleigh}$) and the extent of biodegradation (B_{true}) obtained from the model; right subplot: extent of over-/underestimation of the actual extent of biodegradation by the Rayleigh equation.*

4.5 Chapter summary and conclusions

Isotope fractionation by sorption and transverse dispersion

A number of studies has shown that not only biodegradation, but also physical processes such as sorption and diffusion can affect the isotope signature of organic contaminants in groundwater systems (e.g., Kopinke et al., 2005; Rolle et al., 2010; Jin et al., 2014). The vast majority of studies, however, was conducted as laboratory-scale experiments and the influence of physical processes on isotope fractionation on the field scale, and hence the bias in the estimation of biodegradation by the Rayleigh equation, remains unclear. The experiments in the intermediate-scale indoor aquifer model and the model-based analysis of the data were conducted to bridge this gap.

Sorption ($R = 1.25$ $[-]$) significantly affected the isotope signature of toluene under transient conditions, and led to the overestimation of the extent of biodegradation by the Rayleigh equation at the invading front the toluene pulse of almost 50% at sampling point F2-8 and of almost 100% in the pulse center (model prediction). The increased overestimation in the pulse center arises from the fractionating effect of transverse dispersion and should be treated with caution, since the effect of transverse dispersion could not be determined accurately by the current experimental design (see results of Model C in table 4.4). To ultimately constraint the effect of transverse dispersion on the $^{13}C/^{12}C$ isotope signature of toluene, diffusion/dispersion experiments, as conducted

for deuterated BTEX compounds and *Cl* isotope fractionation of PCE and TCE (Rolle et al., 2010; Jin et al., 2014), should be conducted.

While sorption can affect the isotope signature under transient conditions this effect vanishes for steady-state contaminant plumes (Kopinke et al., 2005). The experiment and the reactive-transport simulations for a steady-state toluene plume (continuous toluene injection) suggest that isotope fractionation by transverse dispersion can lead to an overestimation of biodegradation by the Rayleigh equation of up to 30% close to the source zone and that the effect of transverse dispersion on the isotope signal is decreasing with travel distance (15% overestimation at $x = 4.2m$).

Isotopes and reactive-transport modeling

In recent years, reactive-transport modeling has proven to be a helpful tool for the interpretation of complex isotope signatures, resulting from coupled biogeochemical and physical processes, which can no more be analyzed with simple analytical tools like the Rayleigh equation (e.g., Rolle et al., 2010; Bouchard et al., 2008; van Breukelen and Rolle, 2012), and isotope data have been shown to provide useful information in addition to concentration measurements for model calibration (Atteia et al., 2008; D'Affonseca et al., 2011; Prommer et al., 2008).

This study emphasizes that individual snapshots of concentrations and isotope signals in time and/or individual point measurements in space are not sufficient for process identification. Concentration and isotope ratio data with high temporal and/or spatial resolution are needed for detailed system understanding, model calibration and hence reliable predictive simulations. Furthermore, using isotope data as additional constraints for model calibration demands more complex reactive transport models, which explicitly account for both reactive and physical processes affecting the isotope signal of organic contaminants in groundwater systems.

This study also exemplifies that isotope data facilitate the simultaneous identification of the maximum reaction rate r_{max} and the half-saturation concentration K_{tol} of the Michaelis-Menten rate law for toluene degradation. However, accounting for CSIA data also demands this more complex rate law over simple first-order decay, which may describe concentration time series or profiles sufficiently well. Thus, adding isotope data to better constrain parameter values of simple models (assuming first-order decay and fractionation only by the reaction) will likely not work out.

Table 4.4: *Comparison of the complex reactive transport model A to four simplified models B-E, where individual processes are simplified or neglected (SNSE is the sum of normalized squared errors and indicates the goodness of fit).*

	Model A Full model fitted with isotope data	**Model B** Full model fitted w/o isotope data	**Model C** Model A w/o fractionation by dispersion	**Model D** Model C w/o fractionation by sorption	**Model E** Model D with firs-order degradation
F2-8	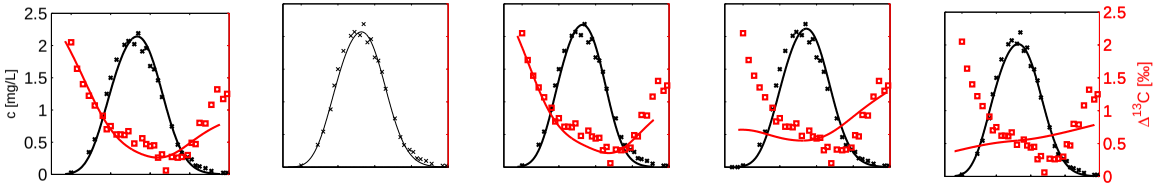				
F2-9	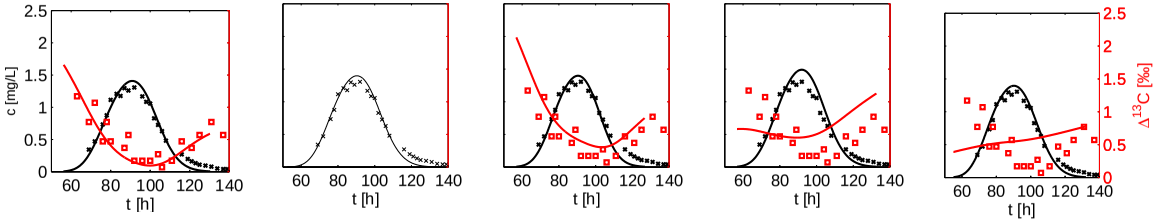				
Estimated parameters and relative parameter uncertainties					
$\mathbf{r_{max}}$ $[10^{-5} mgL^{-1}s^{-1}]$	$1.2 \pm 8\%$	$2.3 \pm 33\%$	$0.83 \pm 7\%$	$1.4 \pm 26\%$	n.a.
$\lambda_{\mathbf{reac}}$ $[10^{-5} s^{-1}]$	n.a.	n.a.	n.a.	n.a.	$1.9 \pm 16\%$
$\mathbf{K_{tol}}$ $[mgL^{-1}]$	$2.2 \pm 12\%$	$6.8 \pm 51\%$	$0.8 \pm 13\%$	2.7 ± 45	n.a.
$\mathbf{R_{tol}}$ $[-]$	$1.25 \pm 1\%$	$1.24 \pm 1\%$	$1.25 \pm 1\%$	$1.28 \pm 2\%$	$1.24 \pm 2\%$
$\varepsilon_{\mathbf{r}}^{\mathbf{kin}}$ [‰]	$-2.15 \pm 1\%$	n.a.	$-1.00 \pm 9\%$	$-0.93 \pm 19\%$	$-1.29 \pm 17\%$
$\varepsilon_{\mathbf{s}}^{\mathbf{equ}}$ [‰]	$-0.31 \pm 7\%$	n.a.	$-0.22 \pm 8\%$	n.a.	n.a.
$\varepsilon_{\mathbf{D}}^{\mathbf{kin}}$ [‰]	$-0.82 \pm 12\%$	n.a.	n.a.	n.a.	n.a.
SNSE toluene	0.8	0.63	1.1	3.3	0.7
SNSE δ^{13}C	8.2	n.a.	13.1	53.1	62
SNSE total	9.0	0.63	14.2	56.4	62.7

Chapter 5

Fringe-controlled biodegradation under dynamic conditions[1]

While fringe-controlled biodegradation has been extensively studied for steady-state flow and transport, so far little is known on the effects of changing hydraulics. Schirmer et al. (2001) and Prommer et al. (2002) studied the effect of transient flow conditions on fringe-controlled biodegradation. Both authors came to the conclusion that biodegradation is enhanced by transient flow conditions, due to enhanced effective transverse mixing of contaminants and dissolved electron acceptors. Cirpka (2005) showed that a large contribution of transverse-mixing enhancement by transient flow is related to sorption differences, which lead to a single enhancement event in the first fluctuation cycle, whereas Cirpka and Attinger (2003) performed a rigorous analysis of mixing enhancement by transient flow in heterogeneous media using first-order theory. However, none of these studies considered beneficial or adverse effects of flow dynamics on microbial degradation linked to initial acclimatization or periods of starvation caused by spatial relocation of the plume fringe.

Anneser et al. (2008) recorded vertical bio-geochemical profiles across a BTEX plume at a former gasworks in Düsseldorf-Flingern (Germany) with a spatial resolution of 2.5 cm at time intervals of three to five months over many years. In addition to the finding that microbial activity is most pronounced at the fringe zone of the BTEX plume (Anneser et al., 2008, 2010; Jobelius et al., 2011), the authors observed vertical expansion

[1]The content presented in this chapter is modified from *D. Eckert, P. Kürzinger, R. Bauer, C. Griebler and O. A. Cirpka (2015). Fringe-controlled biodegradation under dynamic conditions: Quasi 2-D flow-through experiments and reactive-transport modeling. Journal of Contaminant Hydrology, 172, pp 100-111* (Eckert et al., 2015).

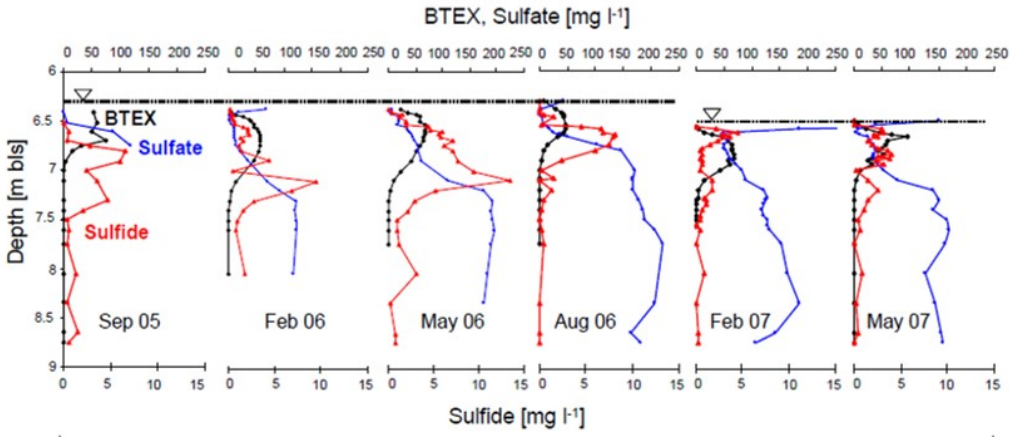

Figure 5.1: *Vertical profiles of BTEX, sulfate (major electron acceptor at the site) and sulfide (reaction product) concentration across a BTEX plume at a former gasworks in Düsseldorf-Flingern. This figure is taken from Anneser (2008).*

and shrinkage of the plume between individual sampling campaigns for time periods of constant groundwater table and a vertical relocation of the entire BTEX plume in the decimeter range accompanied by a falling groundwater table (see Fig. 5.1) (Anneser et al., 2007).

Thus, even though transient flow and transport conditions might increase the potential for biodegradation due to increased transverse mixing of the contaminant and the electron acceptor, the findings of Anneser et al. (2007) and the fact that 99% of the microbial biomass lives attached to the sediment surfaces (Anneser et al., 2010) rise the question how these dynamics affect the microbial activity in the narrow mixing zone along the plume fringe.

In this study, I quantitatively investigated the effects of temporal dynamics in groundwater systems, e.g., the spatial alteration of a contaminant plume due to fluctuating groundwater levels, on in situ biodegradation in contaminated aquifers. Towards this end, quasi two-dimensional flow-through microcosm experiments were performed by Kürzinger (2007), in which she introduced toluene and the aerobic toluene degrader *Pseudomonas putida F1*. The toluene plume was alternated in its vertical position several times. The geochemical and microbial data were analyzed by reactive-transport modeling.

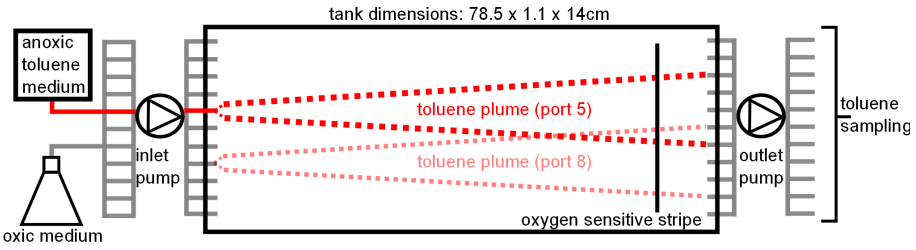

Figure 5.2: *Experimental set up.*

5.1 Experimental setup

The experiment was performed in a quasi two-dimensional flow-through microcosm with inner dimensions (length $\times$ width $\times$ height) of $78.5 \times 1.1 \times 14cm$. The flow-through microcosm was homogeneously filled with sterile medium-sized quartz sand with a grain diameter of 212-300 μm. The system was equipped with eleven in- and outflow ports each, where the spacing between neighboring ports was 1.2 cm. Flow rates at individual ports were adjusted to obtain a uniform seepage velocity of 1.2 md^{-1}. A detailed description of the flow-through microcosm set up can be found in Bauer et al. (2008). Nine inlet ports were continuously supplied with an oxygen saturated, bicarbonate-buffered freshwater medium (Widdel and Bak, 1992). Depending on the experimental phase, either port five or port eight was fed by an anoxic freshwater medium containing toluene (carbon source and electron donor) and bromide as conservative tracer at concentrations of $24 \pm 2.1\ mgL^{-1}$ and $56 \pm 2.7\ mgL^{-1}$, respectively (see Figure 5.2). During the course of the experiment the synchronous injection of toluene and bromide was switched between injection ports five and eight three times. For a detailed description of the different experimental phases see Table 5.1.

Toluene and bromide concentrations were measured by GC-MS (DSQ, Thermo Electron, Dreieich, Germany) and ion chromatography (Dionex AS3500, Idstein, Germany), respectively, at the inlet and all outlet ports to obtain a mass balance. Oxygen concentrations were monitored via a non-invasive optode-array technique (Microx 1/FIBOX, PreSens, Regensburg, Germany) along a vertical cross-section at a distance of 74 cm from the inlet (Bauer et al., 2009a; Haberer et al., 2011).

After establishment of steady-state abiotic transport, the flow-through microcosm was inoculated with the aerobic toluene degrader *Pseudomonas putida F1* at day 16 of the experiment with a cell density of approximately $7 \times 10^7\ cells/ml$ for a period of four

Table 5.1: *Experimental phases*

Phase I	day 1-26	toluene injected at port 5
	day 16	inoculation of *P. putida F1* at ports 4 and 6
Phase II	day 26-39	toluene injected at port 8
Phase III	day 39-59	toluene injected at port 5
Phase IV	day 59-88	toluene injected at port 8

hours. Inoculation was performed via inlet ports four and six, which, were at that time adjacent to the inlet port of the toluene medium (port five).

Cell abundance in pore water was measured at specified time points at the outlet ports and additionally sediment samples were taken at distances of 14.5, 36.5 and 58 cm from the inlet to quantify the amount of attached cells at the end of the experiment. Cell numbers were measured by an LSR II flow cytometer (Becton Dickinson, NJ, USA).

The experiment was performed by Petra Kürzinger and Dr. Robert Bauer under the supervision of Dr. Christian Griebler at the Institute of Groundwater Ecology at the Helmholtz Center Munich. Further information on the experiment and the microbial and chemical analysis can be found in Bauer et al. (2008) and Kürzinger (2007).

5.2 Model description

Microbial dynamics in the flow-through system were descried by the following set of equations:

$$\frac{\partial X_{mob}}{\partial t} = -\mathbf{v}\cdot\nabla X_{mob} + \nabla\cdot(\mathbf{D}_X \nabla X_{mob}) - r_{att}, \tag{5.1}$$

$$\frac{\partial X_{att}^{act}}{\partial t} = r_{gr} - r_{dec} + \frac{n}{(1-n)\rho_s} r_{att} - r_{deac} + r_{reac}, \tag{5.2}$$

$$\frac{\partial X_{att}^{inact}}{\partial t} = r_{deac} - r_{reac}, \tag{5.3}$$

in which X_{mob} [ML^{-3}] is the concentration of mobile microorganisms, X_{att}^{act} [MM^{-1}] is the concentration of attached active microorganisms, X_{att}^{inact} [MM^{-1}] is the concentration of attached inactive microorganisms, $\mathbf{v}$ [LT^{-1}] is the seepage velocity, $\mathbf{D}_X$ [L^2T^{-1}]

is the local dispersion tensors for mobile microorganisms, r_{att} [$ML^{-1}T^{-1}$] is the rate of microbial attachment, $n/((1-n)\rho_s)$ [L^3M^{-1}] is the ratio of water volume to mass of solids in the porous medium with n [-] denoting porosity and ρ_s [ML^{-3}] the mass density of the solids, r_{gr} [$MM^{-1}T^{-1}$] is the growth rate, r_{dec} [$MM^{-1}T^{-1}$] is the rate of biomass loss due to endogenous respiration, r_{deac} [$MM^{-1}T^{-1}$] is the deactivation rate for active microorganisms and r_{reac} [$MM^{-1}T^{-1}$] is the reactivation rate for dormant microorganisms.

Irreversible attachment of mobile bacteria X_{mob} was considered to simulate the inoculation of the flow-through microcosm with *Pseudomonas putida F1* on day 16 of the experiment. Microbial attachment is described as a first-order process under consideration of a maximum carrying capacity for attached cells X_{att}^{max} [MM^{-1}] (Ding, 2010):

$$r_{att} = k_{att} X_{mob} \left(1 - \frac{X_{att}^{act} + X_{att}^{inact}}{X_{att}^{max}}\right), \tag{5.4}$$

in which k_{att} [T^{-1}] is the the first-order attachment rate coefficient. Since the majority of bacterial cells, and therefore biodegradation capacity, in porous media were shown to be attached to the sediments (e.g., Anneser et al., 2010; Holm et al., 1992; Griebler et al., 2002), detachment and further transport of cells was neglected in the model.

Microbial growth was simulated by dual Monod kinetics, under consideration of a maximum biomass carrying capacity (see Eq. 2.14).

While a non-mechanistic lumped decay term (see Eq. 2.17) is applied in standard reactive-transport models to account for any kind of biomass loss over time (e.g., Barry et al., 2002; Cirpka and Valocchi, 2007; Prommer et al., 2009) we hypothesize that the dominant contribution to loss in cellular material in the flow-through microcosm was endogenous respiration, i.e., the oxidation of cell reserves in the absence of external substrates (Mason et al., 1986; Murphy and Ginn, 2000). The rate of biomass loss due to endogenous respiration r_{dec} was described by a linear reaction rate law and a Monod term to account for the presence of oxygen as a limiting factor:

$$r_{dec} = k_{dec} \left(\frac{c_{ox}}{c_{ox} + K_{ox}}\right) X_{att}^{act}, \tag{5.5}$$

with the maximum endogenous-respiration rate coefficient k_{dec} [T^{-1}].

Dormancy, i.e., the ability to switch between an active and inactive state of low metabolic activity was shown by numerous studies to be an effective strategy for microorganisms

Table 5.2: *Basic transport and reaction parameters. All parameter values listed in this table are similar for model 1 and model 2.*

Geometric Parameters		
domain dimensions (L×H)	$[m]$	0.78×0.14
number of cells	$[-]$	78×140
Transport Parameters		
v	$[ms^{-1}]$	1.39×10^{-5}
n	$[-]$	0.48[a]
ρ_s	$[KgL^{-1}]$	2.65
d	$[m]$	2.5×10^{-4}
D_l	$[m^2s^{-1}]$	1.95×10^{-8}[a]
D_{aq}^{tol} at 20°C	$[m^2s^{-1}]$	0.96×10^{-9}[b]
$D_{aq}^{O_2}$ at 20°C	$[m^2s^{-1}]$	2.1×10^{-9}
D_{aq}^{X} at 20°C	$[m^2s^{-1}]$	2.0×10^{-9}[c]
k_{att}	$[s^{-1}]$	2.2×10^{-4}[d]
Inflow Conditions		
source width	$[m]$	0.012
c_{tol}^{in}	$[mgL^{-1}]$	24
$c_{O_2}^{in}$	$[mgL^{-1}]$	8
X_{mob}^{in}	$[cells/L]$	7×10^{10}
inoculation time	$[h]$	4
Biokinetic Parameters		
K_{tol}	$[mgL^{-1}]$	1.3[a]
K_{ox}	$[mgL^{-1}]$	0.3[a]
Y	$[cells/mg_{tol}]$	2.9×10^{9}[e]
X_{att}^{max}	$[cells/g_{sed}]$	3×10^{9}[f]
f_{gr}	$[mg_{ox}/mg_{tol}]$	2[g]
f_{dec}	$[mg_{ox}/mg_{tol}]$	1.1[g]

[a] Bauer et al. (2009a)
[b] Calculated by empirical correlation of Worch (1993).
[c] Estimated from D_T given in Strobel et al. (2011).
[d] Chrysikopoulos et al. (2012)
[e] Obtained from batch experiments.
[f] Maximum cell abundance observed in experiment.
[g] Assuming an electron transfer fraction of 0.35 from toluene to biomass synthesis (see Appendix A).

to survive unfavorable environmental conditions (Mason et al., 1986; Roszak and Colwell, 1987; Kaprelyants et al., 1993; Lennon and Jones, 2011). Deactivation of active microorganisms under unfavorable conditions, i.e., in the absence of toluene as carbon and energy source, was implemented in the model as a first-order kinetic process as outlined in Stolpovsky et al. (2011):

$$r_{deac} = (1-\theta) k_{deac} X_{att}^{act}, \tag{5.6}$$

in which k_{deac} $[T^{-1}]$ is the first-order deactivation rate coefficient and θ $[-]$ is a switch function describing the transition between the active and the dormant state of the microorganisms. The switch function θ [-] is adapted from Stolpovsky et al. (2011):

$$\theta = \frac{1}{\exp((-r_{gr} + r_{dec})/(0.1 \cdot r_{gr})) + 1}. \tag{5.7}$$

θ is approaching a value of 1 under favorable conditions, when the growth rate has been larger than the decay rate for some time, and a value of 0 under long-lasting unfavorable conditions. Reactivation of dormant microorganisms was described by:

$$r_{reac} = \theta k_{reac} X_{att}^{inact}, \tag{5.8}$$

with the reactivation rate coefficient k_{reac} $[T^{-1}]$.

The rate of toluene degradation r_{tol} $[\mathrm{ML^{-3}T^{-1}}]$ is related to microbial growth by the cell yield Y $[\mathrm{MM^{-1}}]$:

$$r_{tol} = -\frac{(1-n)}{n} \rho_s \frac{r_{growth}}{Y}. \tag{5.9}$$

The rate of oxygen consumption r_{ox} $[\mathrm{ML^{-3}T^{-1}}]$ is given by:

$$r_{ox} = -f_{gr} r_{tol} - f_{dec} \frac{(1-n)}{n} \rho_s \frac{r_{dec}}{Y}, \tag{5.10}$$

in which f_{gr} and f_{dec} are the stoichiometric coefficients for oxygen consumption due to microbial growth and endogenous respiration, respectively. The parameter values applied in the model are listed in Table 5.2.

Numerical methods

The coupled system of two-dimensional reactive transport equations was discretized by the cell-centered Finite Volume Method with upwind differentiation of the advective term and the global-implicit approach was adopted for the coupling of transport and

reaction terms. The resulting system of coupled non-linear algebraic equations was linearized by the Newton-Raphson method, and the UMFPACK solver, implemented in Matlab (Davis and Duff, 1997), was used to solve the linear system of equations. An adaptive time-stepping scheme, with small time steps when a front moves through the system and large time steps when steady state is approached, was applied in order to keep the balance between computational costs and numerical accuracy. The code was written as a Matlab program.

The model was verified by comparison to the measured vertical concentration distribution of the conservative tracer bromide at the outflow of the flow-through microcosm under stable plume conditions (see Fig. 5.3). We also compared the simulation results for a simplified version of the reactive-transport model, in which dormancy and endogenous respiration were neglected, to the analytical solution of Cirpka and Valocchi (2009) for steady-state plumes, which showed a perfect agreement for toluene and oxygen concentrations and a good agreement for the concentration of attached bacteria (data not shown).

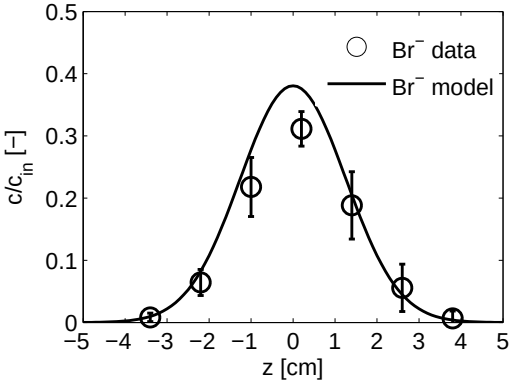

Figure 5.3: *Vertical concentration profile of the conservative tracer bromide at the outlet of the flow-through microcosm, averaged over all phases of stable plume conditions, and simulated profile with the transverse dispersion coefficient calculated by Eq. 2.6*

5.3 Results and discussion

5.3.1 Mass balance of toluene and bromide

Figure 5.4 depicts the mass flux of toluene and the conservative tracer bromide leaving the flow-through chamber via all eleven outlet ports in % of the incoming mass flux.

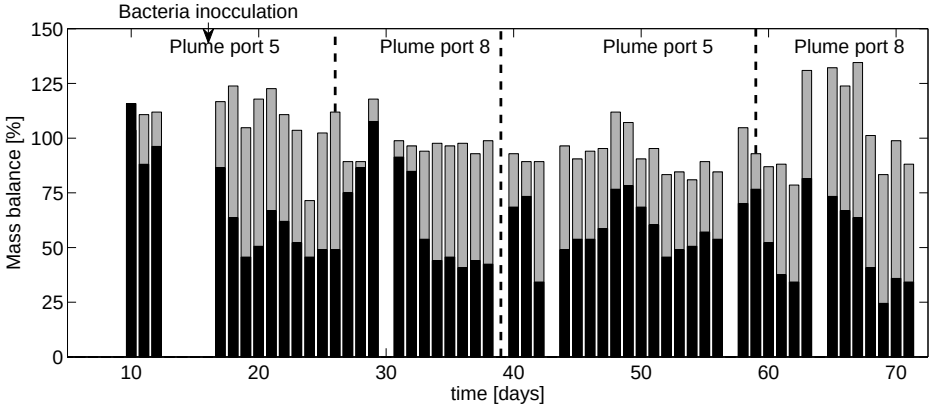

Figure 5.4: *Observed mass balance for toluene (black bars) and the conservative tracer bromide (gray bars), vertical dashed lines indicate the time points of plume alteration.*

The mean mass recovery for the conservative tracer bromide and toluene (abiotic phase of experiment) at the outflow of the flow-through chamber was 84 $\pm$ 12 % and 71 $\pm$ 8 % respectively. The incomplete mass recovery for the tracer most likely arises from the difficulty to maintain equal flow rates at all outflow ports. The somewhat lower mass recovery for toluene during the abiotic phase is pointing towards some additional loss of toluene mass during the sampling procedure.

In comparison to bromide, the mass balance for toluene shows a clear temporal trend. Two days after inoculation of the flow-through chamber with the aerobic toluene degrader *Pseudomonas putida F1* (day 16) the mass flux of toluene at the outlet leveled at approximately half the value observed under abiotic conditions (day 1 to 16). This indicates that, taking into account the inoculation with a comparably high density of fully active cells, the system achieved its full biodegradation potential already two days after inoculation.

When the toluene plume was relocated for the first time from port five to port eight on day 26, the mass flux of toluene leaving the flow-through chamber increased to reach values similar to those observed under abiotic conditions (day 1-16). It took approximately one week until the system recovered its full biodegradation potential on day 33. The observed lag phase in toluene degradation after the first plume alteration was most likely determined by the time the bacteria in the 'new' fringe region needed to grow to a cell density large enough to substantially affect the toluene concentration. Since bacteria were inoculated via ports four and six, adjacent to the initial port of toluene injection, the initial abundance of *Pseudomonas putida F1* at the 'new' fringe region was very low.

When toluene injection was switched back from port eight to port five on day 39, the system recovered its full degradation potential within less than three days, which is approximately twice as fast as after the first plume shift. This most likely can be explained by bacteria having remained on the sediment from experimental phase I were now again located at the plume fringe where toluene and oxygen mixed.

Following the last plume relocation of the experiment on day 59 no increase in toluene mass flux could be observed. A short-term failure of the ceramic piston pump maintaining the supply of the toluene medium, and therefore the disappearance of the contaminant plume during the night between day 61 and 62, however, led to an increase in the mass flux of toluene and bromide on day 63. After this technical disturbance of the system, toluene degradation stabilized again on day 68.

5.3.2 Vertical oxygen and toluene profiles

Figure 5.5 shows vertical profiles of dissolved oxygen (upper panel) measured at a distance of 74 cm from the inflow boundary and vertical profiles of toluene concentration (lower panel), measured at the outlet ports of the flow-through chamber and normalized by the toluene concentration at the inlet.

The strong decrease in the toluene degradation capacity after relocating the toluene plume for the first time (day 26), is manifested in the oxygen profiles. The total extent of depletion in dissolved oxygen was much smaller for day 28 (green squares) and day 31 (blue "+" symbols), two and five days after plume alteration, respectively, than it was at day 26 (black "$\times$" symbols), the day of the plume relocation. Only at day 35 (red circles) full depletion in dissolved oxygen at the current plume position had developed. The oxygen profile for day 28 (green squares) indicates that microbial activity started earlier at the upper fringe of the plume than at the lower fringe at that time, which suggests that the upper fringe of the plume being injected at port eight and the lower fringe of the plume being injected at port five might have partially overlapped.

Interestingly, the measured oxygen profile for day 28 showed a slight depletion in dissolved oxygen (25%) at the 'old' location of the toluene plume, even though the toluene plume had already disappeared at this location on day 28 (see corresponding toluene profile in lower panel of Figure 5.5), two days after injection at port five had been stopped. This suggests that the attached microbial population was still actively respiring, even in the absence of fresh toluene as external substrate. The consumption of

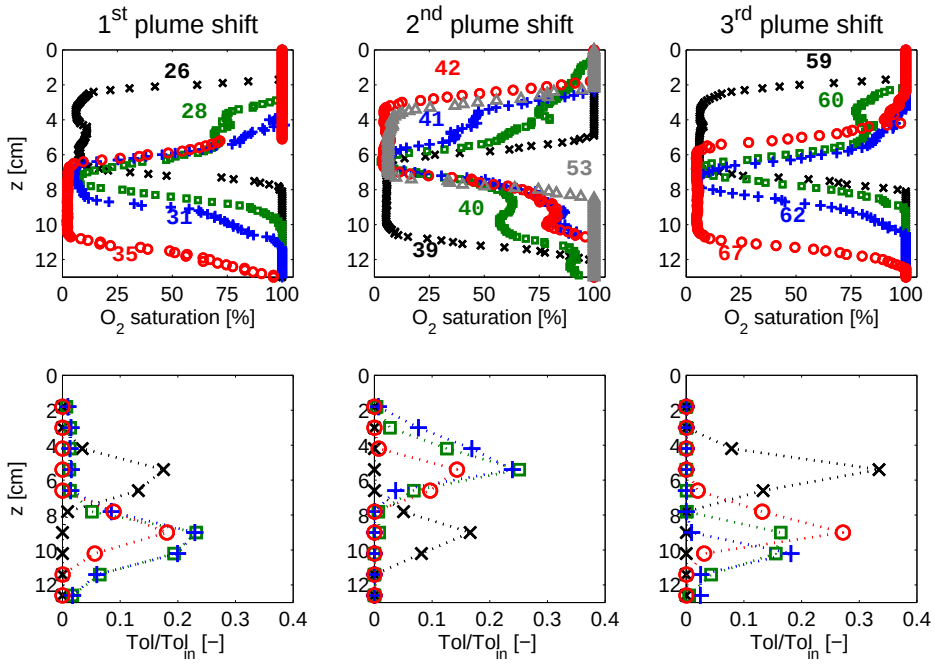

Figure 5.5: *Vertical profiles of oxygen saturation (x=74cm) and normalized toluene concentration (x=78.5cm) for selected days of the experiment. Oxygen profiles are given in the upper panel and toluene profiles in the lower panel. The separate columns of sub-plots indicate the development of concentration profiles following each of the three plume shifts. Numbers next to the profiles indicate the day of the experiment.*

oxygen in the absence of an external energy source has been observed in previous flow-through experiments (Murphy et al., 1997b) and might be attributed to the respiration of endogenous carbon storage products, i.e., cell reserves produced under favorable conditions, or even the oxidation of an excess of macromolecules (such as RNA) (Mason et al., 1986).

The oxygen profiles for the second plume relocation (back from port eight to port five) show a similar picture than those of the first plume shift. This time, however, complete depletion in dissolved oxygen at the new plume position (port five) was achieved more than twice as fast. This observation is in agreement with the toluene mass balance and indicates that bacteria stayed attached to the sand matrix for two weeks, even though there was no toluene present, and regained activity within two days.

Oxygen profiles for the third plume shift show a similar pattern to the first two shifts. Due to the pump failure in the night between day 61 and 62, however, it took until day 67 to reach stable oxygen profiles.

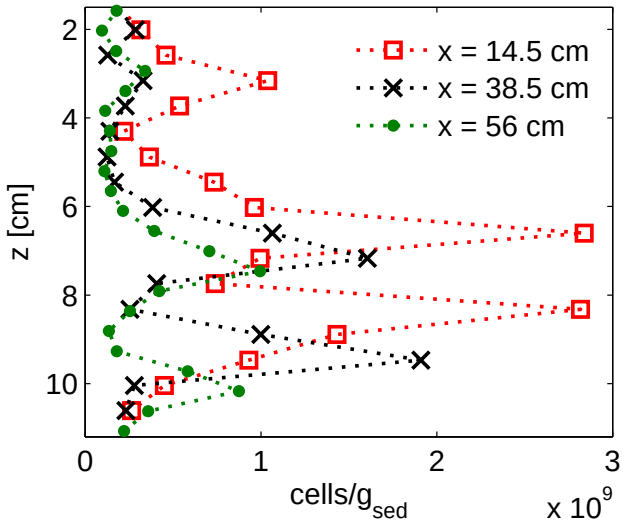

Figure 5.6: *Vertical profiles of attached cells at the end of the experiment for different distances from the inlet.*

5.3.3 Cell counts

Figure 5.6 depicts the vertical distribution of attached microbial cells for three different distances from the inflow boundary at the end of the experiment (day 88). Each profile shows two distinct peaks at the fringes of the toluene plume, which was supplied at port eight during the last experimental phase. The highest cell abundance (3×10^9 $cells/g_{sed}$) was found at the vertical profile closest to the inlet (x=14.5cm, red squares) and maximum abundance decreased with increasing distance from the inlet. This is in accordance with previous findings under steady-state injection conditions (Bauer et al., 2009b).

Another distinct but smaller peak in cell abundance was present at $z = 3$ cm, with a maximum value of 1×10^9 $cells/g_{sed}$. This peak indicates the position of the upper plume fringe during experimental phases I and III, when toluene was injected at port five.

Assuming the same maximum cell abundance for the fringes of the previous plume position (port five) as for the plume position at the end of the experiment (port eight), the total number of attached cells would have decreased by a factor of three during a period of 29 days (time between last plume alteration and end of experiment). Further assuming exponential decay of microbial cells over time ($X_{att}/X^0_{att} = e^{-k_{dec}t} = 1/3$), as

it is done in standard reactive-transport models (e.g., Barry et al., 2002; Prommer et al., 2009) , a first-order decay coefficient k_{dec} of $\approx 0.04\ d^{-1}$ is obtained.

Figure 5.7 shows the total amount of cells flushed out of the flow-through microcosm (upper panel) and the cell density observed at individual outflow ports for the time of the second plume shift (lower panel). Due to technical problems during the first phase of the experiment, cell counts could only be performed from day 35 onwards.
An increase in the total amount of cells washed out can be observed after the second (day 39) as well as the third plume shift (day 59), indicating that the microbial community in the flow-through chamber is adapting to the altered conditions. In both cases it takes ≈10 days until the amount of cells flushed out decreases to the same level as before the plume shift. The number of cells flushed out at individual outlet ports (Figure 5.7, lower panel) shows an increase in washed out cells for the time after the 2^{nd} plume shift (day 41, 42 and 43) at the ports adjacent to port five, the toluene injection port during experimental phase III (day 39 to 59) and a general increase in the number of cells washed out for day 45.

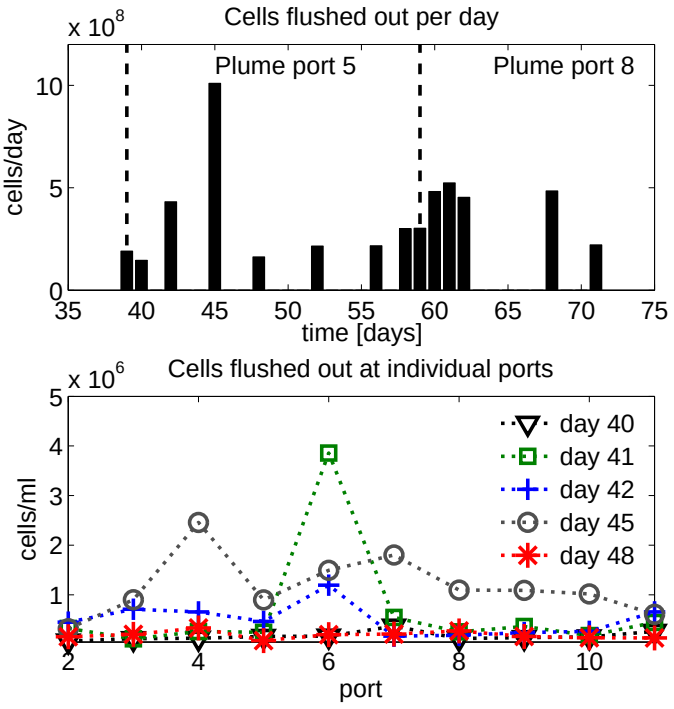

Figure 5.7: *Upper panel: cumulative flux of cells per day at the outflow; lower panel: cell densities at individual outlet ports.*

5.3.4 Reactive-transport modeling

The finding that the number of cells attached to the sediment was reduced only by a factor of three during a starvation period of almost one month (Fig. 5.6), indicates that microbial biomass did neither decay nor detach in large amounts but mainly stayed attached to the sediment, even in the absence of toluene as the sole carbon and energy source. While microbial growth is most likely the factor governing the observed lag in toluene degradation after the first shift of the plume to a location where it has not been present before (day 26), factors other than cell growth have to be responsible for the observed lag in toluene degradation after the 2^{nd} plume relocation on day 39, when the plume was shifted to a position where it had already been before.

To quantitatively analyze the experimental data, we set up and calibrated a reactive-transport model, and compared the model outcome to the toluene and oxygen data. Simulation runs were performed under two different assumptions. Model 1 accounts for microbial growth, endogenous respiration of active bacteria, and the ability of bacteria to switch to an inactive (dormant) state of minimum metabolic activity in order to survive unfavorable conditions (e.g., Bär et al., 2002; Wirtz, 2003; Stolpovsky et al., 2011). Model 2 assumes that the bacteria are always active, and accounts only for microbial growth and a non-mechanistic, lumped decay term, as it is done in standard bioreactive transport models (e.g., Barry et al., 2002; Cirpka and Valocchi, 2007; Prommer et al., 2009).

In order to compare the observed and simulated recovery of toluene mass for the biotic phase of the experiment, the measured toluene mass recovery was corrected for variations in flow rates between individual ports and toluene loss during sampling by normalizing it to the measured mass recovery for the conservative tracer bromide and the measured mass recovery for toluene under abiotic conditions.

Figure 5.8 shows the measured and simulated (model 1) toluene mass balance in the upper panel and the measured and simulated (model 1) oxygen profiles for the 1^{st} and 2^{nd} plume relocation in the mid and lower panel, respectively. The observed extent of toluene degradation at the outflow under stable conditions (e.g., from day 20 to 26) of 30-50 %, which is controlled by transverse mixing, is well reproduced by the simulated removal of 35 % of the incoming toluene mass flux.

While the main characteristics of the dynamic phases, i.e. after switching the plume injection port, are also captured by the model, the length of the observed lag phase in

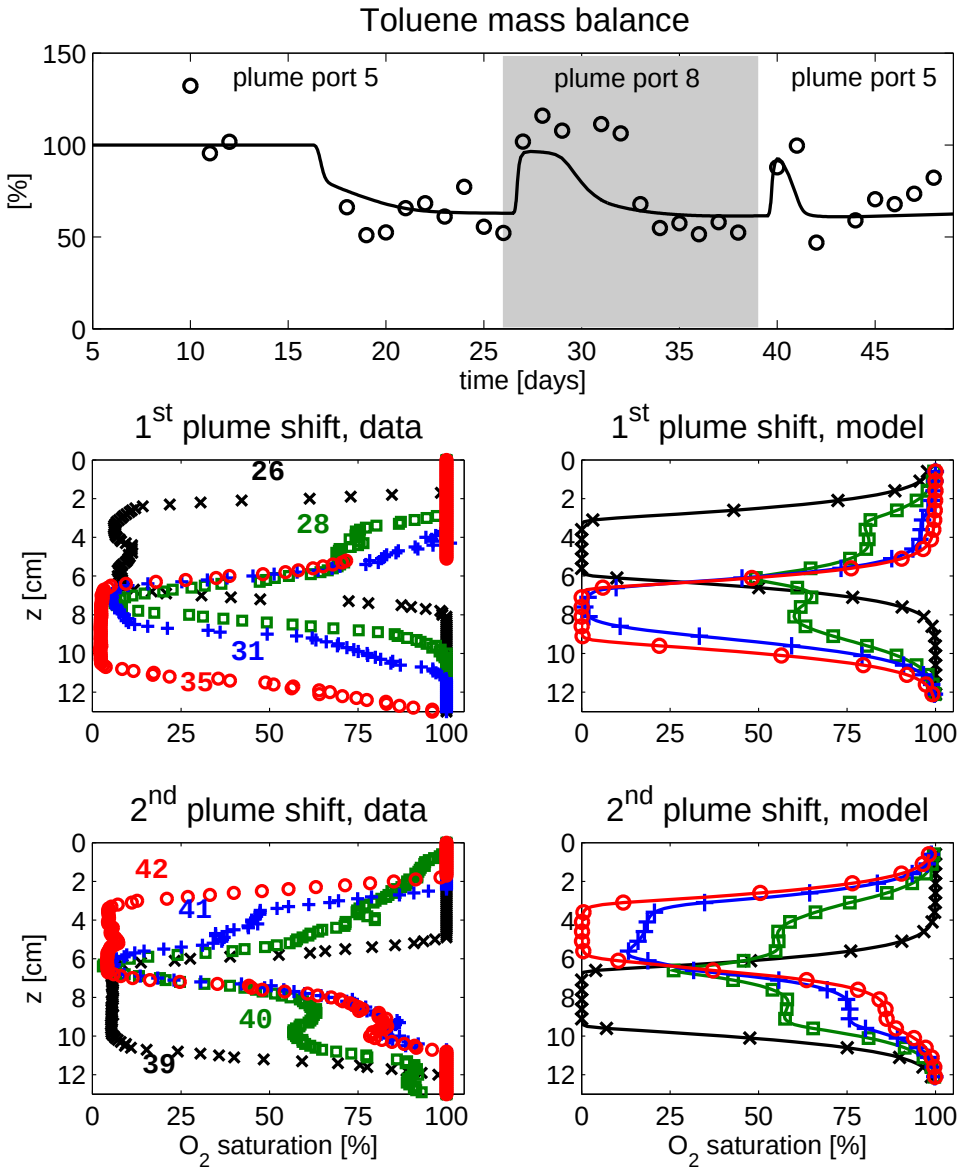

Figure 5.8: *Comparison of experimental data for the toluene mass balance (upper panel) and profiles of dissolved oxygen at x=74 cm (mid and lower panel) to the model outcome of model 1, in which the microorganisms switch between an active and an inactive (dormant) state, and consume oxygen in the absence of toluene by endogenous respiration.*

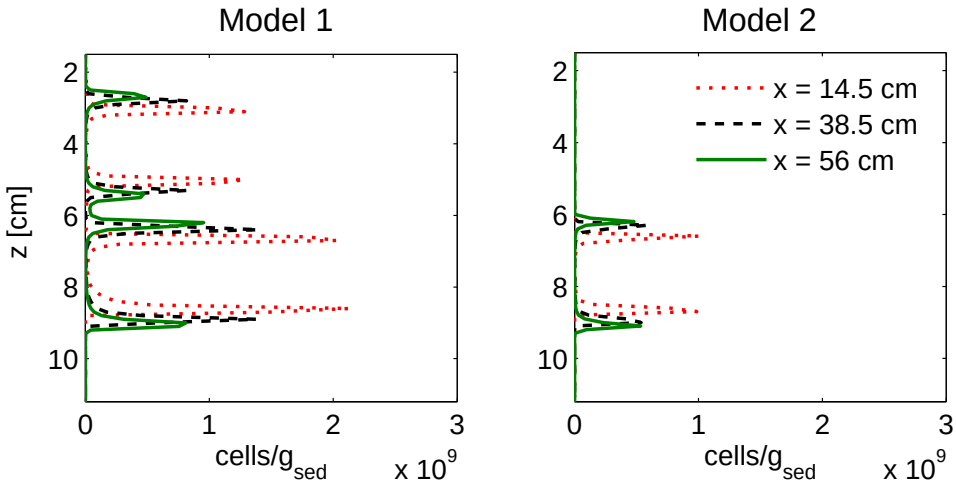

Figure 5.9: *Simulated distribution of attached microorganisms at the end of the experiment (day 88). Left figure: model 1, which considers microbial growth, endogenous respiration and microbial dormancy. Right figure: model 2, which considers only microbial growth and a lumped decay term.*

toluene degradation after the first plume relocation is underestimated, which might suggest that the initial microbial density at the 'new' fringe location, when the plume was injected at port eight, was lower than predicted by the model. In addition to the dynamics in toluene mass recovery at the outflow, the temporal dynamics in oxygen consumption are also matched reasonably well by the model accounting for microbial dormancy and endogenous respiration. The vertical expansion of the anoxic plume core, and consequently the degree of overlap between the anoxic zones resulting from the alternating toluene injection at ports five and eight, however, is systematically underestimated by the model. The same discrepancy between measured and simulated oxygen concentration profiles was reported by Ballarini et al. (2014), who simulated fringe-controlled toluene/ethylbenzene degradation under alternating aerobic and nitrate-reducing conditions. Ballarini et al. (2014) saw a possible explanation for the mismatch in observed and simulated oxygen profiles in the distortion of the optical oxygen measurements by the formation of N_2 gas bubbles. While the formation of N_2 gas bubbles can be definitely ruled out for the current purely aerobic system, we can currently not provide an explanation for the discrepancy between the observed and the simulated expansion of the anoxic zone.

The experimentally observed and simulated depletion in dissolved oxygen for regions where toluene had already been washed out support the finding of Murphy et al. (1997b)

that attached bacteria may affect groundwater redox conditions even after the disappearance of external substrates by endogenous respiration. Furthermore, observed and simulated oxygen profiles indicate a decrease in oxygen consumption and hence endogenous respiration rates with ongoing toluene starvation.

Model 1 and model 2 (results for model 2 are shown in Appendix C) reproduce the observed toluene mass balance equally well. Model 2, which neglects endogenous respiration as well as microbial dormancy, however, is neither able to capture the time lag between disappearance of the toluene plume and stop of oxygen consumption, nor the observed profiles of attached bacteria at the end of the experiment at all.

A comparison of the simulated distribution of attached bacteria for both models is given in Figure 5.9. Considering the calibrated decay coefficient k_{dec} of 0.5 d^{-1} for model 2 (fitted biokinetic parameters are listed in Table 5.3), which was necessary to reproduce the observed toluene mass balance with a model that fully attributes any lag in toluene degradation to microbial growth, the amount of attached cells would be expected to decrease by more than six orders of magnitude within 29 days ($X_{att}/X^0_{att} = e^{-k_{dec}t} = 5 \times 10^{-7}$). Obviously this was not the case in the experiment (Fig. 5.6). Model 1, which accounts for microbial dormancy, in contrast, captures the distribution of attached bacteria at the end of the experiment reasonably well.

The simulation results for model 1 show four distinct, rather narrow peaks in the abundance of attached cells at the fringes of the toluene plume, which was injected at port eight during the last phase of the experiment, and the fringe region of the 'previous' plume, which was injected at port five during experimental phase three (Fig. 5.9). In the experiment, in contrast, only three but somewhat wider peaks in bacterial abundance were observed. Partially this discrepancy might be attributed to the spatial resolution of the sediment sampling. Another possible explanation for the discrepancy between experimentally observed and simulated depth profiles of cell abundance might be chemotactic migration of *P. Putida* F1 cells (e.g., Strobel et al., 2011) between the adjacent plume fringes of the toluene plumes injected at ports five and eight, which was not considered in the model.

The estimated first-order rate coefficient for reactivation of dormant bacteria (model 1) with a value of 0.01 d^{-1} is much smaller than the value of 24 d^{-1} estimated by Stolpovsky et al. (2011) for a batch toluene degradation experiment. In the batch experiment simulated by Stolpovsky et al. (2011) a *Pseudomonas putida* culture was amended with toluene and pulses of oxygen, leading to a temporal depletion of oxygen in the

Table 5.3: *Fitted biokinetic parameters for the reactive-transport model accounting for microbial growth, dormancy as well as endogenous respiration (model 1), and the model considering only microbial growth and a lumped decay term (model 2).*

Parameter		**Model 1**	**Model 2**
μ_{max}	$[d^{-1}]$	2.9	2.9
k_{dec}	$[d^{-1}]$	0.2	0.5
k_{deac}	$[d^{-1}]$	0.4	-
k_{reac}	$[d^{-1}]$	0.01	-

batch system for around 12 hours. Even though it is difficult to directly compare the two values, because of the different experimental setups (e.g., flow-through vs batch experiment, toluene vs oxygen starvation), and a slightly different model formulation in both studies, the comparison of the reactivation rate parameters indicates that the time dormant *Pseudomonas putida* cells needed to become metabolically active again increased with increasing starvation time. An increase in time needed for reactivation of dormant cells with starvation time has also been reported by Kaprelyants and Kell (1993), who performed batch scale starvation experiments with the bacterial strain *Micrococcus luteus*.

5.4 Chapter summary and conclusions

The key objective of the present study was to quantify the effects of changing hydraulic conditions on the efficiency of fringe-controlled biodegradation. Towards this end, the position of a toluene plume was altered in flow-through microcosm experiments in a steady-state flow field. This caused alternating periods of good and bad growth conditions at the fringe locations of the two plumes. The hypothesis was that intermittent starvation reduces the overall efficiency of biodegradation. However, the short- term plume dynamics applied in the experiments ($frequency \approx 2/month$) did not lead to a drastic reduction in the biodegradation potential of the system. Once a stable degrading community had been established at a plume fringe, the majority of cells stayed attached to the sediment even in the subsequent absence of toluene as carbon and energy source. Attached bacteria regained their full biodegradation potential within two days after reappearance of the toluene plume.

The comparison between model simulations and experimental data indicated that this behavior can be explained by dormancy of the bacteria, i.e. the ability of bacteria to switch to a state of low metabolic activity (dormant state), in order to survive periods of unfavorable environmental conditions, such as the temporary lack of growth substrates (e.g., Mason et al., 1986; Roszak and Colwell, 1987; Kaprelyants et al., 1993; Lennon and Jones, 2011). The results of Kaprelyants and Kell (1993) indicated that the time dormant microorganisms need for reactivation is increasing with the length of the starvation period. Therefore longer lag phases in contaminant degradation might be expected for plume dynamics with lower frequencies, such as in the case of seasonal fluctuations. Performing well-controlled flow-through experiments on longer-term starvation and its effects on the capability of biomass to be reactivated, however, may be very difficult as the probability of some kind of experimental failure increases with the duration of the experiment.

A second insight from reactive-transport modeling was that endogenous respiration is needed to explain the time lag between toluene disappearance and stop of oxygen consumption. In the experiment, apparently, oxygen consumption continued even after the electron donor toluene had already been flushed out. This effect, most likely, is less relevant in most field applications because it only lasts for a short period of time.

Overall, spatial plume shifts will definitely change the prevailing geochemical conditions for microbes attached to the sediment matrix, and thus transiently impair biodegradation activity. However, the results of the current study suggest that aerobic biodegradation systems fairly quickly regain their full degradation capacity after disturbance.

Chapter 6

Effect of heterogeneity on biodegradation in dynamic plumes

Aquifer heterogeneity was shown to enhance fringe-controlled biodegradation if the plume fringe is focused in high conductivity zones, since mixing of contaminated and ambient groundwater, carrying 'fresh' dissolved electron acceptors, is enhanced (e.g., Werth et al., 2006; Rolle et al., 2009; Bauer et al., 2009a; Chiogna et al., 2011b; Cirpka et al., 2011, 2012). As pointed out in chapter 5, in-situ biodegradation in porous aquifers might be hampered by fluctuations in plume position, since the vast majority of contaminant degraders was found to reside attached to the sediment matrix (e.g. Hazen et al., 1991; Griebler et al., 2002; Anneser et al., 2010). In addition to mixing and hence biodegradation enhancement, flow-focusing might also reduce the effect of plume fluctuations on biodegradation performance, if the plume fringe is focused in the same high-conductivity zone before and after the fluctuation. To test this hypothesis, a further experiment in the quasi two-dimensional flow-through microcosm, with heterogeneous sand filling, was performed by Kürzinger (2007).

6.1 Laboratory-scale experiments

Experimental set up

Two rectangular high conductivity inclusions of a length of 20 *cm* and a height of 1.2 *cm* were introduced into the flow-through microcosms. The inclusions were placed exactly at the height of port five, at which the toluene plume had initially been injected

initially. The hydraulic conductivity of the inclusions was 20 times larger than the conductivity of the matrix. Except for the inclusions, the experimental setup is the same as describe in section 5.1. The experiment was performed by the former master student Petra Kürzinger and the former PhD student Dr. Robert Bauer under the supervision of Dr. Christian Griebler at the Institute of Groundwater Ecology at the Helmholtz Center Munich. Further details on the experimental set up can be found in Kürzinger (2007).

Experimental observations

Figure 6.1 depicts the observed mass balance for toluene (black bars) and the conservative tracer bromide (gray bars) during the experiment with two high-conductivity inclusions. The toluene data indicate an immediate start in biodegradation after inoculation of the flow-through microcosm with *P. putida* F1 on day 17 of the experiment. After an initial drop to almost zero, the toluene mass flux at the outlet leveled at approximately 25% of the incoming mass flux for the rest of the experiment. In contrast to the experiment in the homogeneous tank (see Fig. 5.4), the plume shift at day 30 did not affect the biodegradation performance of the heterogeneous system.

Conservative-transport modeling

Figure 6.2 depicts simulated plumes for the conservative tracer, injected at port five (solid line) and port eight (dotted line), for the experimental setup with a homogeneous quartz-sand filling (left subplot) and the one with two high-conductivity inclusions (right subplot). The conservative transport simulations show that both plumes are focused in the high conductivity inclusions, which are indicated by the focused streamlines (horizontal gray lines) in the right subplot.

The degree of mixing of contaminated and ambient groundwater can be quantified by the mixing ratio X (Cirpka and Valocchi, 2007), i.e., the ratio of contaminated water and ambient groundwater at a certain location. X is given by the concentration of a hypothetical conservative tracer, introduced with the contaminated water, normalized by the injected concentration. X equals one in regions where all water stems from the contaminant plume and zero where the contribution of contaminated water is zero. Figure 6.3A shows the vertical distribution of the mixing ratio X across a contaminant plume in a homogeneous domain.

If contaminant degradation depends on the presence of dissolved electron acceptors, biodegradation can be expected to take place predominantly in a narrow region where

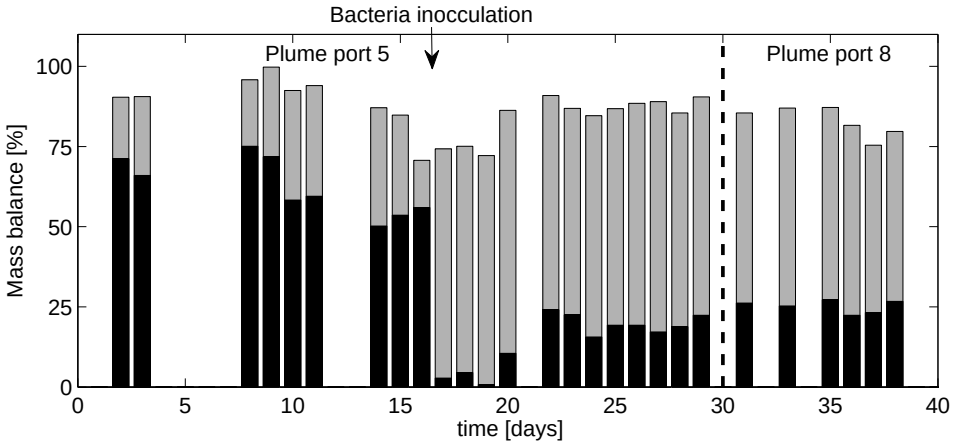

Figure 6.1: *Mass balance for toluene (black bars) and the conservative tracer bromide (gray bars) for the degradation experiment in the quasi two-dimensional flow-through microcosm with two high-conductivity inclusions.*

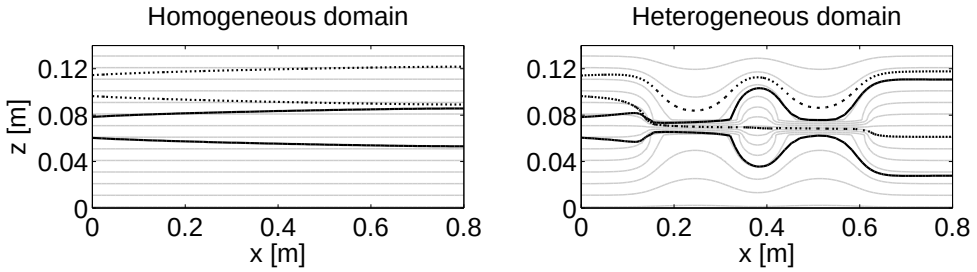

Figure 6.2: *Simulated contour lines ($c/c_{in} = 0.1$) for the plume injected at port five (solid line) and port eight (dotted line) of the flow-through microcosm depicted in figure 5.2 for the homogeneous and heterogeneous tank filling. The horizontal gray lines represent the stream lines.*

the product S $[-]$:

$$S(x,z) = X(x,z) \circ (1 - X(x,z)) \cdot 4, \tag{6.1}$$

and hence the product of contaminant and electron acceptor concentrations, has its maximum (see Fig. 6.3A). The '$\circ$' in Eq. 6.1 indicates an element-wise matrix multiplication. The values of S can range from zero to one. It has to be noted here, that this approach to localize the reactive fringe-zone of a contaminant plume assumes a $1:1$ reaction stoichiometry and similar concentrations of electron donor and acceptor.

Since the vast majority of contaminant degraders in porous media can be found attached to the sediment surface rather than freely floating in the aqueous phase (e.g., Anneser et al., 2010; Holm et al., 1992; Griebler et al., 2002), a shift in the spatial position of the

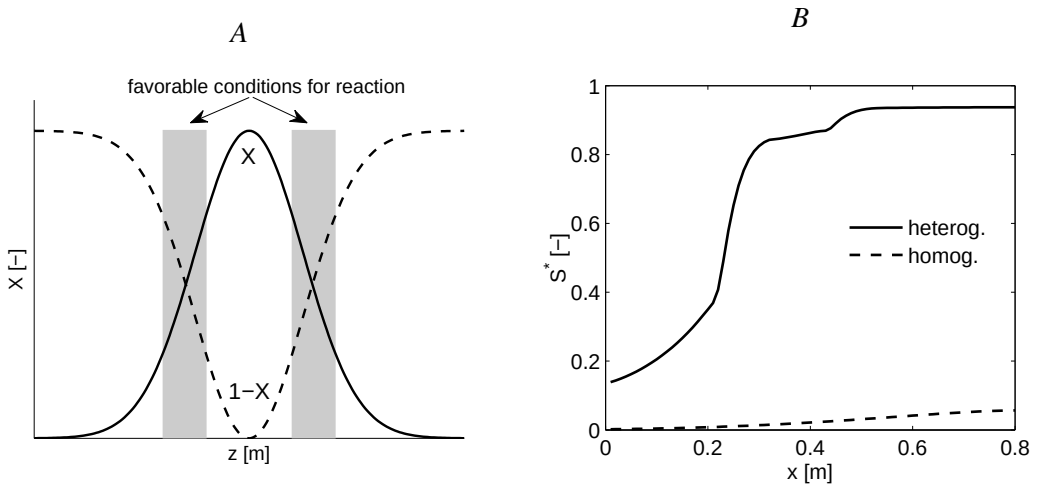

Figure 6.3: *A: Vertical profile of the mixing ratio X [-] across a plume; B: Simulated spatial evolution of S^* in the flow-through microcosm experiments with homogeneous and heterogeneous filling.*

plume fringes, i.e. the zones of favorable conditions for microbial activity, might temporally impair biodegradation. While the relocation of the source zone will definitely result in a spatial shift of the reactive plume fringe zones in a homogeneous domain, flow focusing in heterogeneous domains, however, can potentially enforce the plume fringes to stay at the same location (see Fig. 6.2).

To quantify if the plume-fringe zones overlap before and after a shift in source zone position, the depth-integrated measure S^* $[-]$ is defined:

$$S^*(x) = \frac{\int_0^z (S_{old}(x,z) \circ S_{new}(x,z))\, dz}{\int_0^z (S_{old}(x,z) \circ S_{old}(x,z))\, dz}, \tag{6.2}$$

in which '*old*' refers to the time before the plume shift and '*new*' to the time afterwards. The values of S^* can range from zero to one. While a value of zero implies that the reactive fringe-zones do not overlap at all before and after source zone relocation, a value of one would be obtained if both fringes stay at exactly the same location.

To illustrate the meaning of S^*, this measure is applied to the laboratory experiment described above. Figure 6.3B depicts the evolution of S^* with increasing distance from the inflow. For the homogeneous setup, S^* slightly increases with travel distance. However, it stays well below 0.1. This means that the reactive zones are at different vertical locations before and after toluene injection is switched from port five to port eight (see

Fig. 6.2). For the setup with the two high-conductivity inclusions, S^* strongly increases with travel distance and reaches a value of 0.8 already at the distance of the first high-conductivity inclusion. This implies that the plume fringes are located at more or less the same location, before and after changing the port of toluene injection from five to eight.

6.2 Extrapolation to the field scale

In the flow-through microcosm experiment, two well defined high-conductivity inclusions were placed into an otherwise homogeneous sand filling. Patterns of heterogeneity in hydraulic conductivity encountered in real aquifers, however, are much more complex (e.g., Heinz et al., 2003; Bayer et al., 2011) and therefore difficult to mimic with laboratory-scale experiments. In order to explore possible effects of aquifer heterogeneity on biodegradation in fluctuating contaminant plumes, Monte Carlo simulations of heterogeneous domains were performed for the steady-state distribution of the mixing ratio X in a two-dimensional domain.

Model setup

Random binary conductivity fields, consisting of a low-conductivity matrix and high-permeability inclusions, which make up $\approx 20\%$ of the domain, were constructed as outlined in Werth et al. (2006). Simulations were performed for conductivity contrasts between the matrix and the inclusions of ten and fifty. Figure 3.9 shows the streamlines for a binary conductivity field with a K_{ratio} of 10 and the contour line of an ethylbenzene plume.

The relatively homogeneous sandy aquifer at the BTEX/PAH contaminated site in Düsseldorf-Flingern (e.g. Anneser, 2008; Prommer et al., 2009) was considered as homogeneous reference scenario. Anneser et al. (2007) observed vertical expansion, shrinkage and relocation of the BTEX plume between individual sampling campaigns in the decimeter range (see Fig. 5.1). The source zone is located at the height of the water table and its thickness was estimated to be approximately 30 *cm* in the two-dimensional reactive transport simulations of Prommer et al. (2009). The average hydraulic gradient at the site is 6‰, the mean hydraulic conductivity $1 \times 10^{-3}\ ms^{-1}$ and the mean seepage velocity 1.5 md^{-1} (Anneser, 2008).

Two-dimensional simulations for 100 conductivity-field realizations were performed for a constant hydraulic gradient of 6‰. The source zone was approximated by a line source of 30 *cm* thickness. The mass flux of contaminants emitted from the line source was kept constant between the homogeneous reference scenario and all heterogeneous realizations. This led to a smaller source thickness, for realizations in which the line source was located in a high-conductivity inclusion, as compared to the homogeneous reference scenario. The $25 \times 5m$ two-dimensional domain was discretized by 500 cells in flow direction, and 500 cells perpendicular to the flow direction by a streamline-oriented grid. The linear system of algebraic equations resulting from spatial discretization of the steady-state transport equation was solved by the UMFPACK solver implemented in Matlab (Davis and Duff, 1997).

Simulation results

Figure 6.4 depicts the evolution of S^* with increasing distance from the line source for the homogeneous reference scenario (upper panel), as well as the median and the $10th$ and $90th$ percentile of 100 simulations on random binary conductivity fields (lower panel) with a conductivity contrast of 10 (left subplot) and 50 (right subplot) between the matrix and the inclusions. Simulations were performed for vertical shifts of the line source ranging from 5 to 50 *cm* in the homogeneous scenario. For each individual heterogeneous realization, the line source was shifted over the same water flux, which resulted in a mean spatial displacement for all realizations comparable to the one in the homogeneous reference scenario, but differing spatial displacements of the source zone for individual realizations.

Fort the smallest source zone displacement considered ($5cm$), S^* approaches values of 0.8 and larger for the homogeneous as well as for both heterogeneous scenarios. Flow focusing in high-conductivity zones, however, leads to a much faster increase of S^* with travel distance in the heterogeneous domains. The increasing trend of S^* with travel distances arises from increasing mixing by transverse dispersion, and the increasing probability for the fringe to get focused in the same high-K inclusions, before and after source zone displacement, in the heterogeneous domains. Even though the increase in conductivity contrast between the matrix and the inclusions from 10 to 50 leads to a more rapid increase in S^*, the overall effect on the overlap of the plume fringe zones, before and after line source displacement, seems to be small.

While the shift in line source position by $10cm$ leads to a drastic reduction of S^* for the homogeneous domain, flow focusing in the heterogeneous domains still buffers the

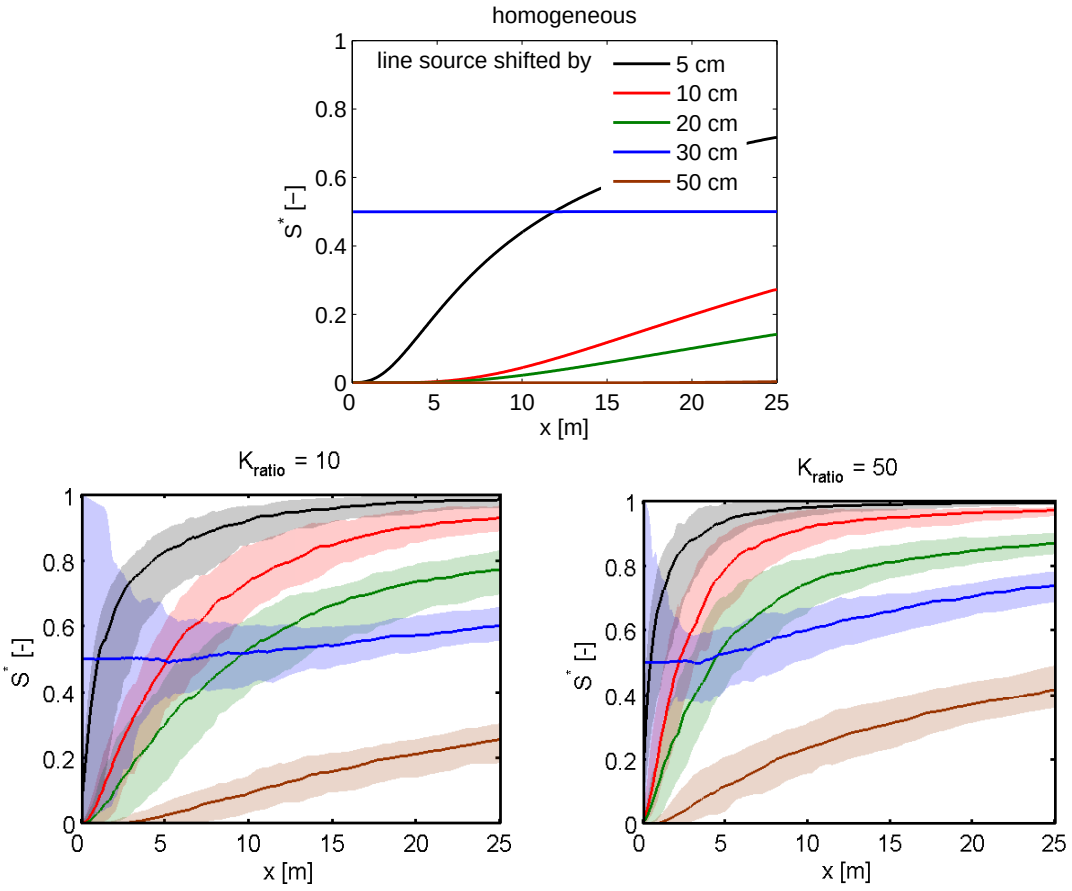

Figure 6.4: *Simulated spatial evolution of S^* for a homogeneous domain (upper panel) with the properties of the BTEX/PAH contaminated aquifer at Düsseldorf Flingern (Anneser, 2008), and binary conductivity fields (lower panel) with conductivity contrasts of* 10 *and* 50. *The solid lines indicate the median, and the dotted lines the* 10*th and the* 90*th percentiles, for 100 simulations on random binary K-fields. Simulations were performed for different magnitudes of vertical source zone displacement between* 5 *and* 50 *cm.*

effect of source zone displacement by 10*cm* to a large extent.

A constant value for S^* of 0.5 in the homogeneous domain is achieved, if the line source is shifted exactly by its height of 30*cm*, and one plume fringe is located at the same position before and after the perturbation. In this case the effect of heterogeneity is much less pronounced and leads only to a slight increase of S^* with travel distance.

While the effect of source zone displacement seems to be compensated to a large extent for small scale fluctuations of about 10 *cm*, a relocation in the vertical position of the line source by 50*cm* leads to much smaller S^*-values, suggesting that this magnitude in vertical line source displacement can no more be compensated for by flow focusing in heterogeneous domains.

6.3 Chapter summary and conclsuions

Based on the finding of Kürzinger (2007) that mixing-controlled biodegradation is not hampered by fluctuations in source zone position, if the plume fringe is effectively focused in the same high-conductivity inclusions beforehand and afterwards, I performed scenario simulations on an ensemble of 100 binary conductivity fields. These fields are constructed to resemble patterns of aquifer heterogeneity encountered in the field more closely than rectangular high-K lenses do. The simulation results suggest that aquifer heterogeneity buffers the effect of fluctuations in source zone position by 10 to 20 *cm* on in-situ biodegradation, which is in the range of the fluctuations in vertical plume position observed by Anneser (2008) at a BTEX/PAH contaminated site in Düsseldorf Flingern.

Chapter 7

Microbial dynamics in flow-through systems under growth and starvation conditions [1]

This chapter deals with the detailed analysis of microbial dynamics and contaminant degradation in aerobic porous flow-through systems under growth and starvation conditions. While batch systems are perfectly mixed and contain only suspended bacteria, natural aquifers are flow-through systems, where bacteria suspended in the mobile aqueous phase and attached to the sediment surface coexist. In aquifers, in fact, the majority of bacteria was found to live attached to the sediment surface rather than freely floating in the aqueous phase (e.g., Hazen et al., 1991; Röling et al., 2001; Griebler et al., 2002; Anneser et al., 2010). Furthermore, a number of studies put forward that diffusive mass-transfer of dissolved compounds to attached cells might be a limiting factor for biodegradation in porous media (e.g., Dykaar and Kitanidis, 1996; Simoni et al., 2001; Hesse et al., 2009). The discrepancy in conditions between flow-through and batch systems rises the question, how representative batch derived degradation and growth rate parameters are for the description of biodegradation in porous media.

Experimental findings regarding the comparability of biodegradation in batch and flow-through systems are ambiguous. While some studies reported that batch derived biokinetic parameters adequately described biodegradation in flow-through systems (e.g.,

[1] The content presented in this chapter is currently prepared for submission to Journal of Contaminant Hydrology (*M. Grösbacher, D. Eckert, O.A. Cirpka and C. Griebler. On the interaction of microbial growth and transport in porous flow-through systems*) and Environmental Science & Technology (*A. Mellage, D. Eckert, M. Grösbacher, O.A. Cirpka and C. Griebler. Microbial dynamics during contaminant degradation in aerobic flow-through systems under growth and starvation conditions*)

Kelly et al., 1996; Schirmer et al., 2000), others observed differences in biodegradation rates between the two different systems (e.g., Simoni et al., 2001; Ballarini et al., 2014).

Based on the finding that the majority of bacteria in aquifers is attached to the soil matrix, the biomass catalyzing the breakdown of organic contaminants is usually treated as immobile species in reactive transport models, and the presence of bacteria suspended in the mobile aqueous phase is neglected (e.g., Barry et al., 2002; Schirmer et al., 2000; Prommer et al., 2006). By contrast, it is well known that bacteria can be transported in porous media, and that they partition between the mobile aqueous phase and the sediment surface (e.g., Ginn et al., 2002; Tufenkji, 2007; Scheibe et al., 2011). The majority of microbial transport studies was conducted under non-growth conditions and aimed to get a better understanding of the physical processes (e.g., straining and filtration) that govern microbial transport in porous media, which is important to understand and predict the spread of pathogens in groundwater.

A few studies, which investigated the effect of biological processes on microbial transport in porous media, indicated that microbial growth strongly affects the partitioning of bacteria between the aqueous phase and the sediment surface in addition to physical processes (e.g., Clement et al., 1997; Murphy et al., 1997a,b; Yolcubal et al., 2002; Jordan et al., 2004). In all of these studies, an increase in microbial detachment, and hence the number of suspended bacteria, was observed after the addition of a growth substrate to the system. Murphy et al. (1997b) suggested that this response might be cell-division mediated transport (Murphy and Ginn, 2000, and references cited herein), i.e. mother cells that are attached to the sediment release the daughter cells to the mobile aqueous phase while they themselves remain attached. Clement et al. (1997) observed an increase in microbial detachment with increasing maximum specific growth rate. Yolcubal et al. (2002) found that the majority of new-grown cells in their column experiments ($68-90\%$) was flushed out of the column under growth conditions, and concluded that suspended bacteria could significantly contribute to biodegradation under appropriate conditions.

In this chapter, I analyze a data set from multiple growth experiments in flow-through columns and batch systems by means of reactive-transport modeling. The experiments were performed by the PhD candidate Michael Grösbacher under the supervision of Dr. Christian Griebler at the Institute of Groundwater Ecology at the Helmholtz Center Munich. Toluene was used as model contaminant and the aerobic toluene degrader *P. putida* F1 was chosen as model organism. Experiments were conducted under growth

as well as substrate-starvation conditions to investigate differences in microbial detachment between these two scenarios. The novelty of this study is that not only growth of suspended cells, but also attached cells at three different locations in the column, were recorded over time. The detailed tracking of suspended as well as attached cells during the course of the experiment enabled the development of a model, which explicitly accounts for cell-division mediated transport.

7.1 Experimental setup

Batch experiments

Batch experiments of aerobic toluene degradation by *Pseudomonas putida* F1 were performed at different initial toluene concentrations, ranging from 10 to 1000 μM, to obtain values for the maximum specific growth rate μ_{max} and the toluene half-saturation concentration K_{tol} that are representative over a wide range of toluene concentrations. In previous studies it was shown that it is impossible to obtain unique values for μ_{max} and K_{tol} from a single growth curve, and that the degree of parameter uncertainty depends on the initial conditions (Schirmer et al., 1999; Liu and Zachara, 2001). Bottles were shaken at 120 rpm to ensure mixing of oxygen into the solution.

Column experiments

Growth experiments with the aerobic toluene degrader *Pseudomonas putida* F1 were performed in short sediment columns with inner dimensions (length $\times$ diameter) of 1.6×1.34 cm (see Fig. 7.1). The columns were filled with natural sediment. Grain sizes ranged from 200 to 630 μm and the porosity was 30%. Experiments were performed at four different seepage velocities: 0.6, 1.8, 3.7 and 9.1 md^{-1}. A multi-channel peristaltic pump (Ismatech, Wertheim, Germany) was used to achieve the desired flow rate. Flow in the column system was from the bottom to the top.

The columns were inoculated with 10^4 to 10^5 $cells/ml$, which is a bacterial concentration frequently encountered in natural aquifers. A bicarbonate-buffered freshwater medium was injected as growth medium (Widdel and Bak, 1992). After inoculation, toluene was injected at concentrations ranging from 30 to 100 μM. To prevent microbial growth in the inlet tubing, toluene and oxygen (electron acceptor) were injected from separate reservoirs. The two solutions joined shortly before the column inlet via tee-connectors.

Water samples were taken at the column in- and outlet to follow toluene degradation and transport of bacteria out of the system. Toluene concentrations were measured by GC-MS analysis and cell numbers were quantified by flow cytometry.
Each experiment was run with several columns in parallel. Two columns were disassembled at specified time points, to measure the bacterial abundance on the sediment. The sediment was partitioned into three layers (bottom, middle and top), and each sediment layer was separately analyzed for attached cells.
Oxygen concentration in the column was measured non-invasively by the optode technique described by Haberer et al. (2011). To this end, oxygen-sensitive foils were glued to the inner column wall at three different locations (bottom, middle and top).

The experiments were performed by the PhD candidate Michael Grösbacher under the supervision of Dr. Christian Griebler at the Institute of Groundwater Ecology at the Helmholtz Center Munich.

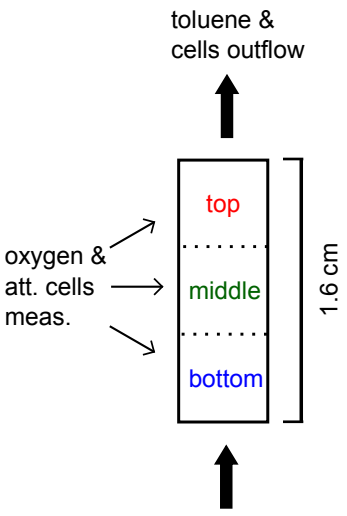

Figure 7.1: *Schematic of a flow-through column.*

7.2 Model description

7.2.1 Batch experiments

Microbially catalyzed toluene (C_7H_8) mineralization to carbon dioxide and water is normally treated as a one-step reaction in reactive transport models:

$$C_7H_8 + 9O_2 \rightarrow 7CO_2 + 4H_2O. \tag{7.1}$$

In reality, however, toluene oxidation proceeds via several intermediates (e.g., Parales et al., 2008). For the aerobic degradation of toluene by *P. putida F1* in batch experiments, Yu et al. (2001a,b) observed and simulated the buildup and further breakdown of 3-methylcatechol, which is formed during initial dioxygenation of the aromatic ring by *P. putida F1*. While the intermediate 3-methylcatechol had to be considered explicitly in the model of Yu et al. (2001b) to jointly match the temporal evolution of toluene concentrations and cell densities, no significant buildup of intermediates could be observed for toluene degradation by *P. putida F1* in the study of Reardon et al. (2000).

Degradation of toluene via the intermediate 3-methylcatechol, coupled to biomass growth, can be described by the following set of ordinary differential equations:

$$\frac{\partial c_{tol}}{\partial t} = -k^{tol}_{max}\frac{c_{tol}}{c_{tol}+K_{tol}}X \tag{7.2}$$

$$\frac{\partial c_{mc}}{\partial t} = +f_{mc}k^{tol}_{max}\frac{c_{tol}}{c_{tol}+K_{tol}}X - \frac{1}{Y_{mc}}\mu_{max}\frac{c_{mc}}{c_{mc}+K_{mc}}X \tag{7.3}$$

$$\frac{\partial X}{\partial t} = \mu_{max}\frac{c_{mc}}{c_{mc}+K_{mc}}X \tag{7.4}$$

in which c_{mc} $[mg/L]$ is the concentration of 3-methylcatechol, f_{mc} $[mg_{mc}/mg_{tol}]$ is a stoichiometric factor for the conversion of toluene to 3-methylcatechol, k^{tol}_{max} $[1/d]$ is the maximum specific toluene degradation rate and Y_{mc} $[cells/mg_{mc}]$ is the cell yield for microbial growth on 3-methylcatechol. Since toluene and 3-methylcatechol contain the same number of carbon atoms, the transformation from toluene to 3-methylcatechol does not lead to cell growth.

7.2.2 Column experiments

The one-dimensional reactive transport model for growth of *P. putida F1* in the column experiments considers the three mobile species: toluene (electron donor and carbon source), oxygen (electron acceptor) and mobile bacteria, and the immobile species: attached bacteria. Microbial growth was simulated by standard dual Monod kinetics

(see Eq. 2.13). In contrast to the batch experiment, toluene degradation could be adequately described as one-step reaction, and the formation and further degradation of 3-methylcatechol did not have to be considered in the model.

The rate of change of immobile X_{att} $[cells/ml_{Sed}]$ and mobile X_{mob} $[cells/ml]$ bacteria is described by:

$$\frac{\partial X_{att}}{\partial t} = r_{gr}^{att} + n r_{att} - r_{det} \tag{7.5}$$

$$\frac{\partial X_{mob}}{\partial t} = -v\frac{\partial X_{mob}}{\partial x} + D_l \frac{\partial^2 X_{mob}}{\partial x^2} + r_{gr}^{mob} - r_{att} + \frac{1}{n} r_{det} \tag{7.6}$$

in which n $[-]$ is the porosity, r_{gr}^{att} $[cells/ml_{sed}/s]$ and r_{gr}^{mob} $[cells/ml/s]$ are the growth rates for attached and suspended cells, respectively , r_{att} $[cells/ml/s]$ is the rate of attachment and r_{det} $[cells/ml_{sed}/s]$ is the detachment rate.

The results from the column experiments indicated, that attached bacteria grew to a maximum density, i.e., that there is a maximum carrying capacity of the system for attached bacteria X_{att}^{max}. Once X_{att}^{max} was reached, attached bacteria still continued to grow. All new-grown cells, however, were released to the mobile aqueous phase and finally flushed out of the column. This release of new-grown cells to the mobile aqueous phase, i.e., cell-division mediated transport (Murphy and Ginn, 2000), was implemented in the model by the dynamic detachment rate r_{det}:

$$r_{det} = r_{gr}^{att} \frac{X_{att}}{X_{att}^{max}}. \tag{7.7}$$

As long as X_{att}^{max} is not reached, new-grown cells partially stay attached and partially are released to the mobile aqueous phase. When the carrying capacity is approached, the term X_{att}/X_{att}^{max} approaches unity. Attached bacteria, however, continue to grow at the same rate, releasing all new-grown cells to the aqueous phase.

Attachment of suspended bacteria to the sediment surface is described by a modified first-order rate law (see Eq. 2.20):

$$r_{att} = k_{att} X_{mob} \left(1 - \frac{X_{att}}{X_{att}^{max}}\right), \tag{7.8}$$

to account for the maximum carrying capacity of the system for attached bacteria (Ding, 2010).

In order to match the base-level washout of cells observed in the column experiments, a constant base inflow needed to be considered. The inclusion of a continuous baseline injection of background cells was confirmed by three separate cell number measurements in the inflowing solution during the course of the toluene-starvation experiment (see Fig. 7.8). The source of this background contamination of cells is unknown and inference on it can only be speculative.

Numerical methods

The coupled system of one-dimensional reactive-transport equations was discretized by the cell-centered Finite Volume Method with a spatial discretization of $\Delta x = 0.5\ mm$. Upwind differentiation was applied to the advective term and dispersion was neglected. The global-implicit approach, with adaptive time stepping and a maximum time step size of $600s$, was adopted for the coupling of advection and reaction terms. The resulting system of coupled non-linear algebraic equations was linearized by the Newton-Raphson method, and the UMFPACK solver implemented in Matlab (Davis and Duff, 1997) was used to solve the linear system of equations. Due to the short residence time of mobile compounds in the column, numerical diffusion, arising from upwind differentiation and implicit integration of the advective fluxes in time, was of no practical relevance in this study.

7.3 Results and discussion

7.3.1 Batch experiments

Batch experiments with four different initial toluene concentrations were analyzed to determine the maximum specific growth rate μ_{max} $[1/d]$, the half-saturation concentrations of toluene K_{tol} $[mg/L]$ and 3-methylcatechol K_{mc} $[mg/L]$ and the growth yield Y $[cells/mg]$. The measured and simulated temporal evolution of toluene concentrations and cell densities is presented in figure 7.2. As previously described by Yu et al. (2001a,b), the buildup and further breakdown of 3-methylcatechol had to be explicitly accounted for in the model, in order to jointly match toluene concentrations and cell densities. 3-methylcatechol, however, has not been part of the chemical analysis so far. The model parameters μ_{max}, K_{tol} and Y were manually adjusted to match all four experiments simultaneously. The half-saturation concentrations for toluene and

3-methylcatechol were assumed to be identical, to reduce the number of fitting parameters. Estimated parameter values are given in Table 7.1. While toluene degradation and microbial growth is well described by the model for high initial toluene concentrations, growth is over estimated by the model for low initial toluene concentrations. This might indicate that microbial growth efficiency is decreasing with decreasing substrate concentration.

Table 7.1: *Kinetic parameters for growth of P. putida F1 on toluene as sole carbon source under aerobic conditions in the batch system.*

Parameter		1-step reaction	2-step reaction
μ_{max}	$[d^{-1}]$	4.5	4.5
k_{max}^{tol}	$[d^{-1}]$	–	50
K_{tol}	$[mgL^{-1}]$	0.1	0.1
K_{mc}	$[mgL^{-1}]$	–	0.1
f_{mc}	$[mg_{mc}/mg_{tol}]$	–	1.35
Y_{mc}	$[cells/mg]$	–	2.2×10^9
Y_{tol}	$[cells/mg]$	3.0×10^9	–

7.3.2 Column experiments

Column experiments were performed at four different flow velocities (0.6, 1.8, 3.7 and 9.1 md^{-1}) and three different toluene concentrations (30, 70 and 100 μM) for the flow velocity of 1.8 md^{-1}. Results of the individual experiments, regarding toluene degradation, oxygen consumption and microbial growth, are listed in Table 7.2.
Experimental results are exemplary presented for experiment two ($v = 1.8\ md^{-1}$, $c_{tol} = 70\ \mu M$) at this point. Figure 7.3 depicts the measured toluene concentrations and *P. putida F1* cell densities at the outlet of the column, as well as the concentrations of oxygen and attached cells measured at three different locations (bottom, middle, top) within the 1.6 *cm* long column. Since flow in the columns was from bottom to top, the location 'bottom' is the one closest to the inlet.

Toluene and oxygen concentrations started to decline immediately after the start of the experiment, and reached stable values of approximately 0.5 and 2 mgL^{-1}, respectively, after one day. The temporal evolution of dissolved oxygen concentrations measured in the bottom, middle and top part of the column looked almost identical. This indicates that oxygen consumption, and hence microbial activity, was restricted to the bottom (inflow) part of the column. The same pattern could be observed in the other five column experiments (data not shown).

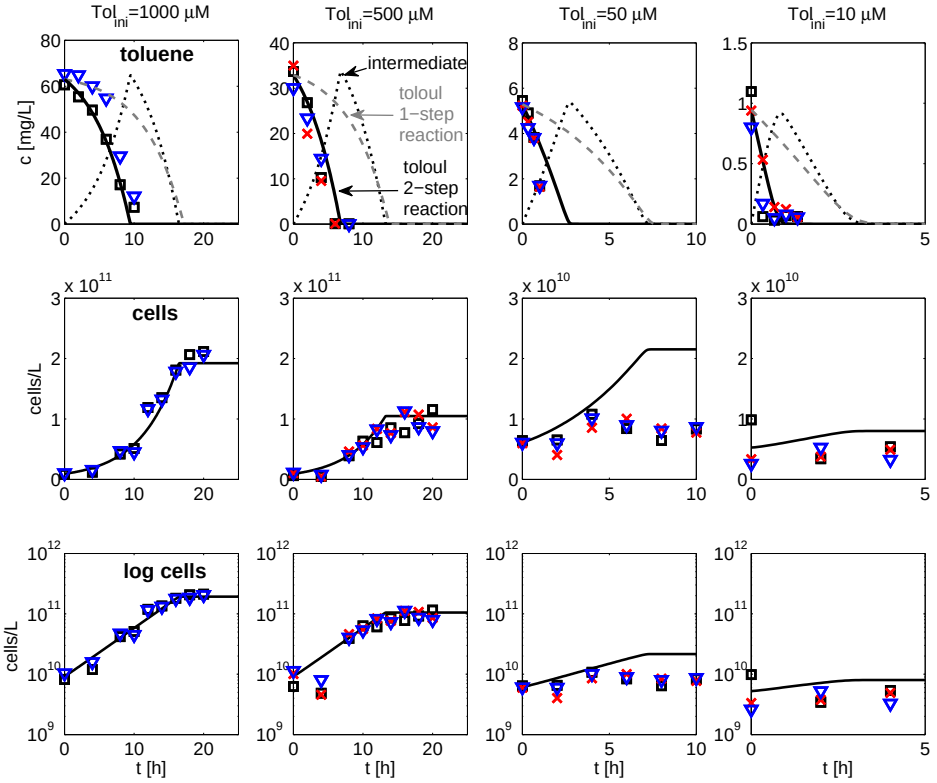

Figure 7.2: *Results of the batch experiments with different initial toluene concentrations and corresponding model fit. Toluene profiles are given in the upper row and the evolution of cell density is shown in the middle (linear scale) and lower row (log scale).*

The number of attached cells per volume of porous media increased by two orders of magnitude between the start of the experiment and the third time-point of sediment sampling at hour 72, whereas it stayed constant for the remaining time of the experiment. The maximum density of attached cells in the bottom part of the column ($2.0 \times 10^8 \pm 3.8 \times 10^7$ $cells/ml_{sed}$) was approximately two times larger than in the middle ($9.9 \times 10^7 \pm 2.0 \times 10^7$) and top part ($9.9 \times 10^7 \pm 2.4 \times 10^7$).

The density of suspended cells in the outflowing water increased by two orders of magnitude and reached a stable value of $2.1 \times 10^6 \pm 2.7 \times 10^5$ $cells/ml$ after 48 hours. The continuous wash-out of 2.1×10^6 $cells/ml$ indicated that attached cells, even though their number stayed constant, were still replicating, releasing the daughter cells to the mobile aqueous phase.

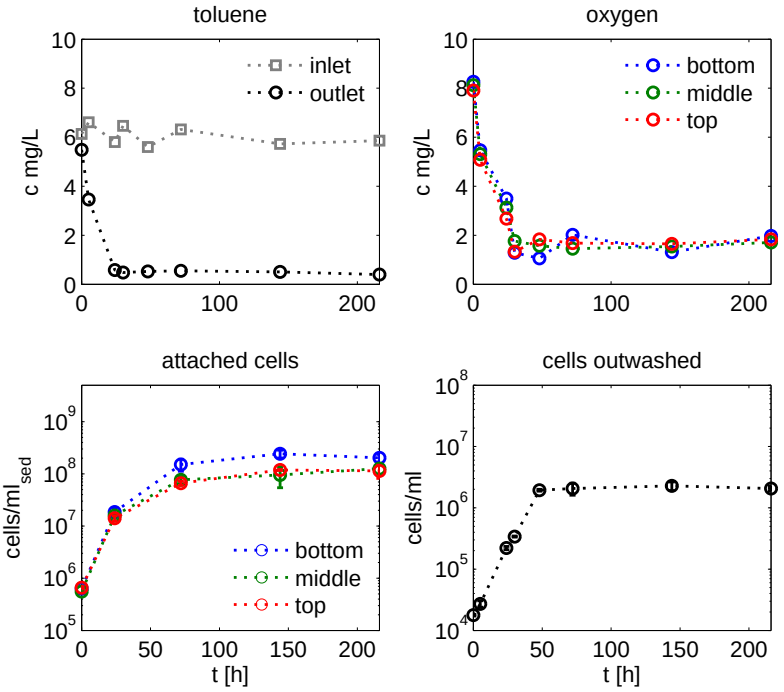

Figure 7.3: *Experimental results for experiment two ($v = 1.8\ md^{-1}$, $c_{tol}^{in} = 70\ \mu M$).*

Table 7.2: *Comparison of the different column experiments.*

Exp	$\mathbf{c_{tol}^{in}}$ $[\mu M]$	**v** $[m/d]$	**Tol deg.** $[mg]$	$\mathbf{O_2}$ **deg.** $[mg]$	$\mathbf{f_{ox}}$ $[mg_{ox}/[cells$	**New cells** $[\times 10^8$ $cells]$	**Cells flush. out** $[\%]$	**Yield** $[\times 10^8$ $cells/mg_{tol}]$	**Cells attached** $[\%]$
1	70	0.6	1.1	1.0	0.9	4.4	70	4	99
2	70	1.8	3.2	4.0	1.3	14	76	4.4	99
3	70	3.7	4.9	6.7	1.4	28	79	5.7	99
4	70	9.1	14.8	n.a.	n.a.	71	60	4.8	99
5	30	1.8	1.0	1.9	1.9	6.6	72	6.6	99
6	100	1.8	4.2	4.9	1.2	53	93	13	98
Batch	-	-	-	-	-	-	-	30	-

Microbial growth in the different column experiments

Results from all six column experiments are listed in Table 7.2. The mass of toluene and oxygen that could be degraded/consumed and the amount of new-grown cells showed an increasing trend with increasing toluene mass flux, i.e., with increasing flow rate as well as with increasing toluene concentration.

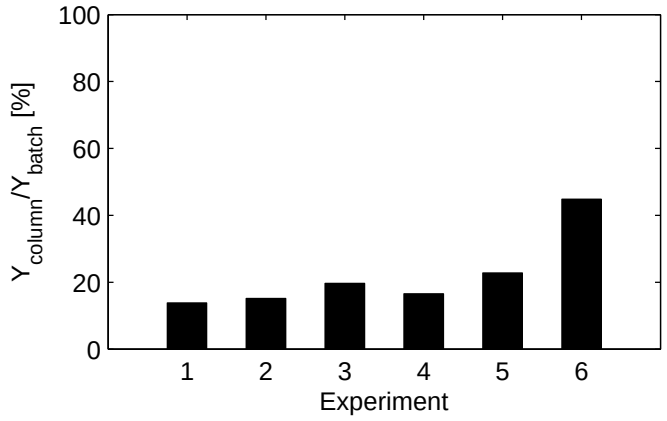

Figure 7.4: *Cell yield for column experiments 1-6 in % of the yield observed in the batch experiments.*

The microbial growth yield Y $[cells/mg_{tol}]$ was calculated for each column experiment by dividing the total amount of new-grown cells (sediment and outflow) by the toluene mass degraded. The values obtained for the different flow-through experiments ranged between 14 % (Exp 1) and 43 % (Exp 6) of the yield observed in the batch experiments (see Fig. 7.4). In contrast to the amount of new-grown cells, the growth yield did not show a clear trend with the flow rate.

Comparing the amount of cells attached to the sediment in the top part of the column (close to the outlet) and the amount of cells in the outflowing water, the distribution of bacteria between water and sediment was estimated . While most of the new-grown cells (60 to 93%) were flushed out of the column over time, the vast majority of cells, and hence biodegradation activity, per volume of porous media ($\geq 98\%$) were found to be attached to the sediment surface in all experiments.

Figure 7.5 depicts the temporal evolution of the amount of attached cells in the individual column experiments, given as mean value of the measured cell densities in the bottom, middle and top part of each column. The mean density of attached cells in the columns under stable conditions ranged between 8.6×10^7 $cells/ml_{sed}$ for experiment one and 9.3×10^8 for experiment four and showed an increasing trend with the toluene mass degraded in the individual experiments. This finding suggests that the mass flux of substrate and electron acceptor might be a control on the biomass carrying capacity of the system, i.e., the amount of attached biomass that can be sustained. For experiment four, the experiment with the highest flow rate, the amount of attached cells under stable conditions in the bottom part of the column was found to be with $2.0 \times 10^9 \pm 5.8 \times 10^8$ $cells/ml_{sed}$ approximately five times larger than in the middle ($4.0 \times 10^8 \pm 1.9 \times 10^8$)

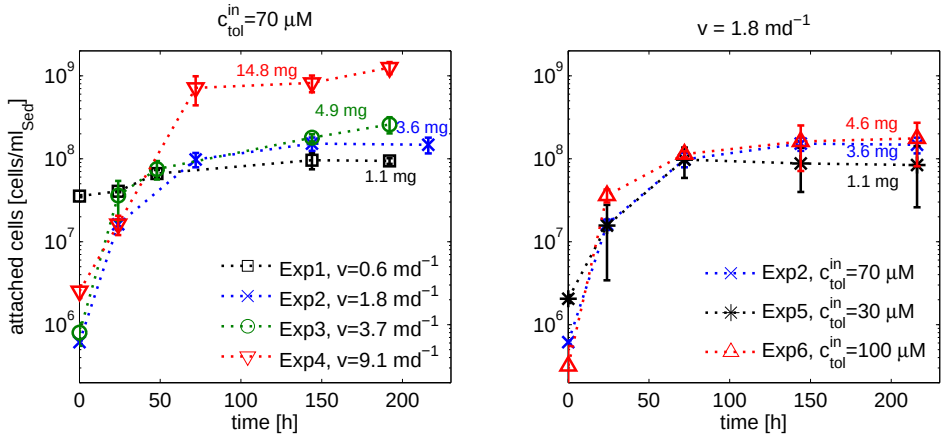

Figure 7.5: *Average amount of attached cells per ml of sediment for the six different column experiments (Exp 1-6). Results for experiments with different flow rates (Exp 1-4) are shown in the left panel and results for experiments with different toluene concentration (Exp 2, 5 and 6) in the right panel. Numbers next to the lines indicate the toluene mass degraded in each experiment*

and top part ($3.6 \times 10^8 \pm 0.9 \times 10^8$). While a gradient in the number of attached cells along the column could also be observed for experiment two, no significant differences in cell numbers between bottom, middle and top were observed in the other experiments.

Oxygen/toluene stoichiometry

Based on a mass balance of toluene and oxygen for each experiment, the stoichiometric ratio f_{ox} [mg_{ox}/mg_{tol}] for oxygen consumption due to growth of *P. putida F1* on toluene was calculated. The f_{ox}-values obtained for the different column experiments ranged between 0.9 and 1.9 mg_{ox}/mg_{tol}. These values are much smaller than the value of 3.1, which is anticipated for the complete mineralization of toluene to carbon dioxide and water. Interestingly, the estimated oxygen/toluene stoichiometry for the toluene-pulse experiment of 1.5 mg_{ox}/mg_{tol} falls in the same range as the values for the column experiments (see Chapter 4.4.2).

Under growth conditions, bacteria oxidize part of the substrate to carbon dioxide to gain energy, while they assimilate the other part of the reduced substrate-carbon into new biomass (Rittmann and McCarty, 2001). This reduces the amount of oxygen needed to degrade one unit of toluene under growth conditions (see Appendix A). In chapter 5, I estimated the stoichiometric coefficient for oxygen consumption under growth conditions f_{gr} to be 2 mg_{ox}/mg_{tol}. This estimate was based on the growth yield obtained from

the batch experiments (3.0×10^9 $cells/mg_{tol}$). Considering the substantially smaller yield values obtained from the column experiments (see Table 7.2), however, results in values for f_{gr} between 2.7 and 3.0 mg_{ox}/mg_{tol}, which is close to the stoichiometry anticipated for complete toluene mineralization. The reason for the small observed oxygen demand in the column experiments can therefore, most likely, not be found in the assimilation of reduced toluene-carbon into biomass.

In the analysis of the toluene-pulse experiment we speculated on incomplete toluene degradation as potential reason for the small observed oxygen demand. The fact that the column data could be reproduced by the one-step reaction model, however, strongly suggests that there is no substantial buildup of intermediates in the column experiments. In the end, the reason for the small oxygen demand for toluene degradation observed in the toluene-pulse as well as in the column experiments remains unclear. It might be helpful to conduct column experiments under nitrate reducing conditions in the future, to see if the nitrate demand for toluene degradation in the column system shows the same pattern.

Reactive transport modeling

Figure 7.6 depicts the results for column experiments two, three and four, and the results of the corresponding reactive-transport simulations. The model parameters are given in Table 7.3. The maximum specific growth rate μ_{max}, the stoichiometric coefficient for oxygen consumption f_{ox}, and the attachment rate coefficient k_{att} were fitting parameters. All remaining parameters were calculated from the batch and column data a priori.

The model reproduces the observed breakthrough curves of toluene and suspended cells at the column outlet, as well as the temporal evolution of the number of attached cells in the bottom, middle and top part of the column very well. The observed and simulated oxygen depletion curves, however, show some mismatch. During the course of experiment four, the observed oxygen concentration at the inlet changed from 4 to 8 and back to 4 mg/L, which is also considered in the model. In contrast to the batch experiments, toluene and cell data could be fitted jointly with the one-step reaction model, and the buildup and further breakdown of intermediates did not have to be considered.

The maximum density of attached cells is approximately one order of magnitude higher for experiment four than for experiments two and three, whereas the density of suspended cells at the outflow is in the same range for all three experiments. The mass flux of cells leaving the column, however, increases with the flow rate from experiment two to experiments three and four. The leveling off of the number of attached cells at

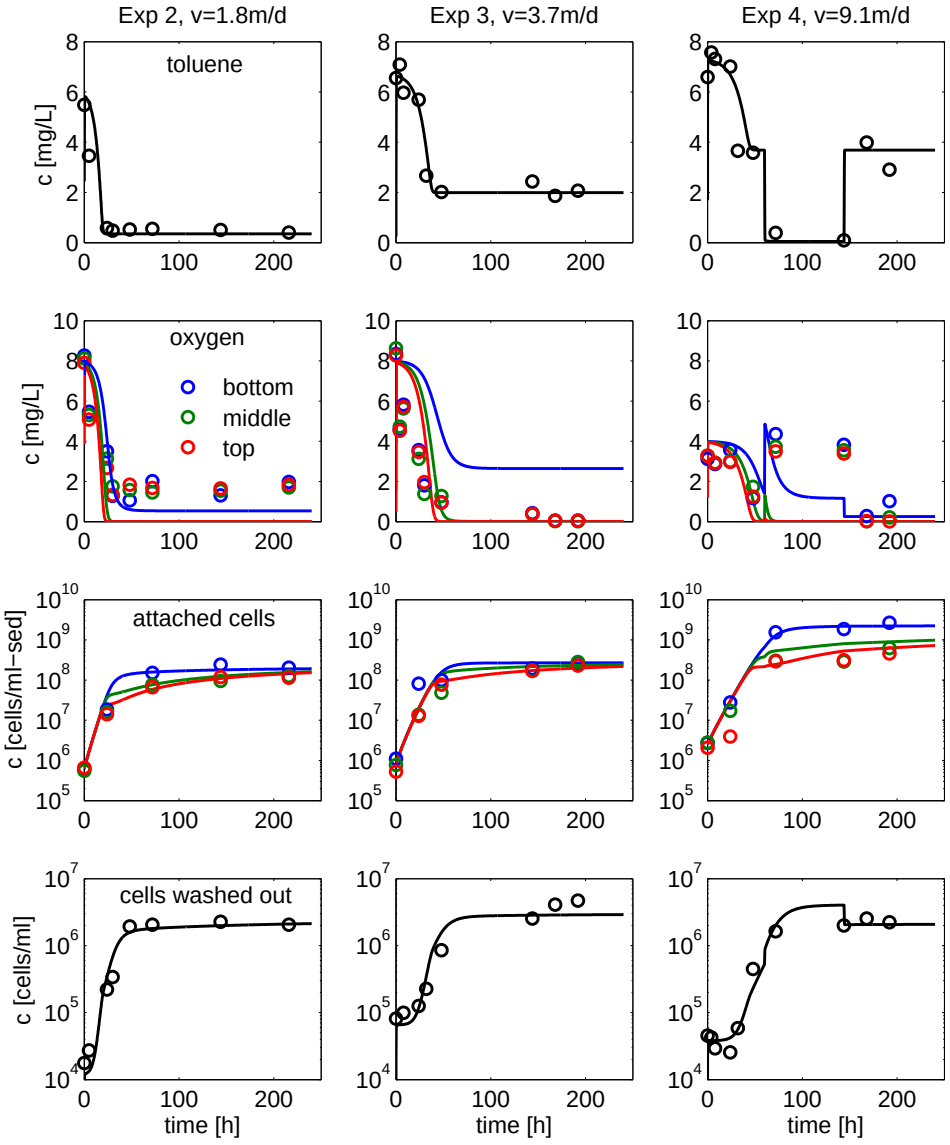

Figure 7.6: *Experimental data and simulation results for experiments two, three and four.*

Table 7.3: *Kinetic parameters for growth of P. putida F1 on toluene in the flow-through columns. Bold parameters are fitted to the column data.*

Parameter		Exp 2	Exp 3	Exp 4
μ_{max}	$[d^{-1}]$	**4.5**	**3**	**2.5**
K_{tol}	$[mg/L]$	0.1	0.1	0.1
K_{ox}	$[mg/L]$	0.3[a]	0.3[a]	0.3[a]
$\mathbf{f_{ox}}$	$[mg_{ox}/mg_{tol}]$	**1.4**	**1.7**	**1.1**
$\mathbf{k_{att}}$	$[d^{-1}]$	**50**	**50**	**100**
X_{att}^{max}	$[cells/ml_{sed}]$	2.0×10^8	2.7×10^8	2.7×10^9
Y	$[cells/mg_{tol}]$	4.4×10^8	5.7×10^8	4.8×10^8

[a] Bauer et al. (2009a)

a maximum value, as well as the continuous outflow of 2 to 4×10^6 $cells/ml$ in all experiments, is well captured by the model, which accounts for cell-division mediated transport, i.e., the release of new-grown cells from the sediment to the mobile aqueous phase. The good fit between the data and the model confirms that attached bacteria in the column system continuously replicate, even though the density of attached cells stays constant after an initial growth phase. While the new-grown cells stay attached to the sediment until the biomass carrying capacity of the system X_{att}^{max} is approached, all new-grown cells are mobilized and finally flushed out of the column later on.

Due to the short residence time of suspended bacteria in the columns, and the fact that the vast majority of bacteria, and hence biodegradation activity, per volume of porous medium were attached to the sediment, toluene degradation in the column system could be fully attributed to the attached bacteria. Therefore, the profiles of toluene, oxygen, and attached cells could also be reproduced without explicit consideration of mobile cells, if a logistic growth-term of the form $(1 - X_{att}/X_{att}^{max})$ is applied to the microbial growth rate, but not to the rates of toluene and oxygen consumption (e.g., Schirmer et al., 2000; Rolle et al., 2010). While suspended bacteria were found to be unimportant for toluene degradation in the column experiments, the majority of new-grown cells (60 to 93%) was flushed out of the columns over time (see Table 7.2). This implies that bacteria have an increased ability to spread and colonize new sediment surfaces under growth conditions.

The remaining toluene concentration at the outlet of the column increases with the flow rate, and the initial drop in concentration is faster for experiment two than for experiments three and four. This is captured by the fitted values of μ_{max}. While the same value was applicable for experiment two and the batch experiment, an almost two-times

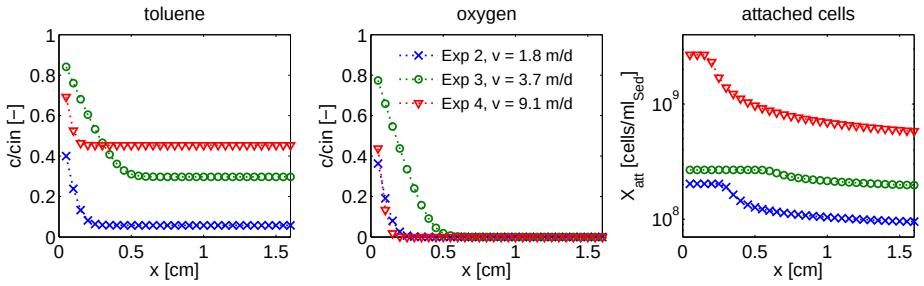

Figure 7.7: *Simulated spatial profiles for toluene, oxygen and attached cells for experiments two, three, and four for t=200h.*

smaller one had to be chosen to match the results of experiment four, the experiment with the highest flow velocity (see Table 7.3). A potential explanation for the observed decrease in the specific growth rate with increasing flow velocity might be a decrease in the bioavailability of toluene and oxygen to the attached bacteria, due to increasing limitations by diffusive mass-transfer on the pore scale at higher flow velocities. Mass-transfer limitations were put forward as explanation for decreased degradation rates in porous media, as compared to batch systems, by numerous studies (e.g., Dykaar and Kitanidis, 1996; Simoni et al., 2001; Hesse et al., 2009). However, the fact that the same value of μ_{max} was obtained for experiment two and the batch experiment, suggests, that diffusive transport of the contaminant and the electron acceptor to, and uptake by the attached bacteria, is not a degradation-rate limiting process at a seepage velocity of 1.8 md^{-1}.

Figure 7.7 depicts simulated spatial profiles of toluene, oxygen, and attached cell concentrations for steady-state conditions ($t = 200h$). The model predicts a rapid decrease in toluene concentrations with travel distance, and the complete consumption of oxygen within the first $5mm$ for all three experiments. This matches the fact that no differences in oxygen profiles could be observed between the three measurement locations, and indicates that microbial activity, and hence toluene degradation, is restricted to a narrow zone at the column inlet.

While microbial attachment is considered in the model, k_{att} is not a very sensitive parameter. The observed increase in the number of attached cells in the middle and top part of the column can be explained to a large extent by microbial growth during the initial phase of the experiment, when oxygen was still available along the entire column.

Starvation experiment

Figure 7.8 shows experimental and modeling results for a modification of experiment two, in which toluene injection was halted for a period of 130 days from day three onwards, to study the behavior of attached and suspended bacteria under conditions of substrate starvation. While toluene injection was switched off for 130 days at day three, the oxygen containing growth medium was continuously injected during the whole experiment.

Except for the growth yield Y, parameters used to simulate experiment two were applicable to match the results of the starvation experiment. To match the observed profiles of attached cells, the yield had to be increased by a factor of two, as compared to experiment two. This resulted in a yield for the starvation experiment which is approximately 30% of the value observed in the batch experiment.

For the simulation of the starvation experiment an inactive fraction of attached bacteria was considered as additional species. The transition between the active and inactive (dormant) state of attached bacteria was mathematically described as outlined in chapter 5.2, with the only difference that the 'switch function' was parameterized with a toluene threshold concentration for microbial activity in this case (Mellage, 2014). A value of 1 $\mu g/L$ for the toluene threshold concentration was merely chosen in order to facilitate a switch in conditions. The actual value was not significant, since the change between good and bad conditions was so abrupt in the experiment. The coefficients for deactivation of attached bacteria during phases of toluene-starvation and reactivation after the resumption of toluene injection were both fitted to a value of 2 d^{-1}.

The number of attached cells increased by a factor of 15 during the first three days and stayed constant for the remaining time of the experiment in the bottom (inflow) part of the column, while cell numbers decreased by approximately 30 to 70% in the middle and top part. The results strongly indicate that no substantial amount of attached cells is lost due to detachment or biomass decay within four months of toluene starvation. While a constant wash-out of about 2×10^5 $cells/ml$ could be observed under toluene-starvation conditions (after day three), the detection of similar cell densities at the column inlet (see Fig. 7.8) indicated that these cells originated to the largest extent from the injection media and did not result from detachment of attached cells.

Upon the resumption of toluene injection into the column at day 133, toluene was readily degraded, and the full biodegradation potential of the system was regained within a quarter of a day.

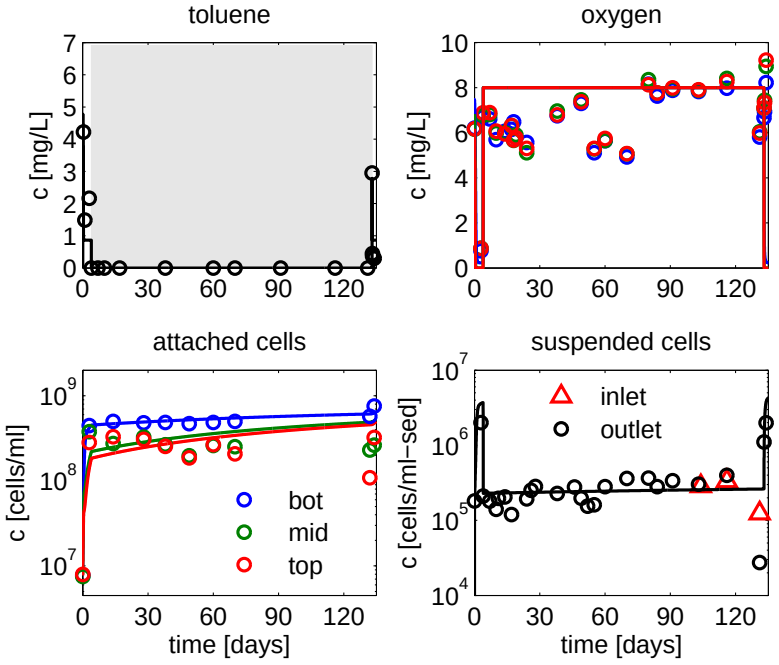

Figure 7.8: *Experimental results and corresponding model fit for the toluene-starvation experiment, in which toluene injection was halted for 130 days at day three and resumed on day 133. The area shaded in grey indicates the toluene-starvation period of 130 days*

The model, which considers a detachment rate of zero under starvation conditions, reproduces the temporal evolution of attached cells in the bottom part of the column well. The slight decrease in the number of attached cells in the middle and top part, however, could not be matched at the same time. Due to the parameterization of the attachment rate (see Eq. 7.8), the model predicts a slight increase in attached cells over time for these locations, which was obviously not observed in the experiment.

7.4 Chapter summary and conclusions

The detailed model-based analysis of multiple column experiments revealed that attached cells were continuously replicating in the presence of the growth substrate toluene. While the vast majority of toluene degrading *P. putida F1* cells per volume of porous medium ($\geq 98\%$) were attached to the sediment surface, most of the new-grown cells ($60-93\%$) were washed-out of the columns over time. Even when the carrying capacity of the system for attached cells was reached, they continued to replicate at the same rate. All new-grown cells, however, were released to the mobile aqueous phase and

finally flushed out of the column. This is of special importance for scenarios where the continuous supply with 'fresh' electron donors and acceptors as well as nutrients gives attached bacteria the ability to continuously replicate, e.g., at the fringe of contaminant plumes. Continuous growth results in a larger contaminant turnover, as the pure fulfillment of maintenance requirements under non-growth conditions does. The carrying capacity of the column systems for attached cells showed an increasing trend with increasing amount of toluene degraded in the individual experiments. This indicates that the utilizable mass flux of substrate might be a control on the carrying capacity for attached bacteria.

Furthermore, the reactive-transport simulations revealed that suspended cells were irrelevant for toluene degradation in the column experiments. Even though the fluid residence time in the columns was very short (2.5 to 39 *min*), a similar behavior can be expected for longer flow distances, since the vast majority of cells, i.e., biodegradation capacity, is attached to the sediment surface. While suspended cells did not contribute to the biodegradation capacity of the system, the continuous release of new-grown cells from the sediment to the mobile aqueous phase strongly increases the ability of bacteria to spread and colonize new sediment surfaces.

The results of the toluene-starvation experiment and the corresponding reactive-transport simulation indicated that no substantial loss in the number of attached cells due to detachment and/or cell decay occurred withing a starvation period of four months, and that the attached bacteria regained their full biodegradation potential within less than a quarter of a day upon the resumption of toluene injection on day 133. In chapter 5 we hypothesized that the time needed for reactivation of the full biodegradation potential might increase with the time of starvation. The results of the column experiments, however, strongly suggest that aerobic contaminant degradation is not drastically hampered by periods of unfavorable conditions of up to four months, which is in the time frame of plume dynamics induced by seasonal fluctuations in hydraulic conditions.

Chapter 8

General conclusions and open questions

8.1 Assessment of in-situ biodegradation by CSIA

Conclusions

In addition to a number of previous studies (e.g., Kopinke et al., 2005; LaBolle et al., 2008; Kampara et al., 2008; Aeppli et al., 2009; Kuder et al., 2009; Rolle et al., 2010; Hoehener and Yu, 2012; van Breukelen and Rolle, 2012; Jin et al., 2014), the results presented in chapters 3 and 4 show that physical processes, such as diffusion/dispersion and sorption, may effect the isotope signature of organic contaminants in groundwater systems, by either acting as rate-limiting step for biodegradation (e.g., inter-phase mass transfer, transverse mixing in fringe-controlled biodegradation) or fractionating themselves between isotopically light and heavy contaminant molecules (e.g., diffusion, transverse dispersion, sorption).

While the extent of isotope enrichment due to biodegradation is always reduced by the rate-limiting effect of physical processes (commitment to catalysis), isotope fractionation by diffusion, transverse dispersion, and sorption can lead to additional isotope enrichment, which might be mistaken for biodegradation. Sorption enhances degradation-induced isotope enrichment at the invading front of a contaminant plume or pulse. Transverse dispersion leads to increased isotope enrichment in the plume center as well as in depth-integrated water samples, withdrawn by fully-screened monitoring wells, if biodegradation is restricted to the plume fringe. Additional isotope enrichment due

to transverse dispersion for depth-integrated water samples, however, seems to be balanced to a large extent by the reducing effect of mixing, if acting as rate-limiting step, in most scenarios investigated.

Considering the adverse effects of physical processes on the isotope signatures of organic contaminants, as well as the difficulties arising from aquifer heterogeneity (Abe and Hunkeler, 2006; van Breukelen and Prommer, 2008; Green et al., 2010), depth-integrated sampling by fully-screened monitoring wells (Kopinke et al., 2005; Thullner et al., 2012), and point sampling by multi-level sampling wells, due to contaminant mass loss by transverse dispersion from individual flow paths (Fischer et al., 2007; Thullner et al., 2012), the quantification of in-situ biodegradation by the Rayleigh equation has to be seen very critical. Nonetheless, CSIA represents a powerful tool to qualitatively assess in-situ biodegradation, since degradation-induced isotope fractionation tends to be reduced or only slightly enriched for most scenarios investigated so far. Isotope enrichment without the occurrence of biodegradation could only be observed, if the invading front of a contaminant plume (sorption), or the plume center (transverse dispersion) is sampled. To ultimately proof the occurrence of in-situ biodegradation, however, CSIA should be applied in conjunction with other methods, such as geochemical measurements, metabolite analysis, or microbiological methods, since "there is no single universally reliable method to asses in-situ biodegradation processes" (Bombach et al., 2010).

Open questions

So far the study presented in chapter 4 represents the only experimental evidence for stable-carbon isotope fractionation of BTEX-hydrocarbons by transverse dispersion. To ultimately constraint the extent of isotope fractionation for these compounds, diffusion/dispersion experiments under abiotic conditions, as performed for deuterated ethylbenzene and Cl-isotope fractionation of PCE (Rolle et al., 2010; Jin et al., 2014), have to be performed in the future.

Another point of interest for future research, which has gained only little attention so far, might be the effect of physical processes on the interpretation of dual-isotope data. In recent years, the analysis of stable isotopes of multiple elements within a molecule, e.g. carbon and chlorine, has been identified as promising tool for the assessment of transformation pathways in natural systems (e.g., Hofstetter et al., 2008; Centler et al., 2013). While the rate-limiting effect of physical processes on isotope fractionation cancels out in 2-D isotope analysis, the fractionating effect of, e.g., diffusion/dispersion

might potentially affect 2-D isotope analysis, if the mass difference between heavy and light isotopes is different for the two elements of interest, such as in the case of stable carbon ($^{13}C/^{12}C$) and chlorine isotopes ($^{37}Cl/^{35}Cl$).

8.2 Effect of dynamic conditions on in-situ biodegradation

Conclusions

While the effect of plume dynamics, such as a shift in plume position due to changing hydraulic conditions, on fringe-controlled biodegradation has only been addressed in a few studies (e.g. Schirmer et al., 2001; Prommer et al., 2002), the results of Anneser (2008) indicate that temporal fluctuations in plume position might not be uncommon.

Microbial activity was shown to be focused in the narrow mixing zone along the fringe of contaminant plumes by a number of recent studies (e.g., Thornton et al., 2001; Tuxen et al., 2006; Takahata et al., 2006; Anneser et al., 2008), and the vast majority of contaminant degraders was found to live attached to the sediments (e.g., Anneser et al., 2010; Holm et al., 1992; Griebler et al., 2002). Therefore, a shift in plume position might transiently impair biodegradation. The experimental and modeling results for aerobic toluene degradation by *P. putida* F1 presented in this thesis, however, suggest that plume dynamics in the order of two weeks to four months do not significantly hamper in-situ biodegradation under aerobic conditions. Four months of toluene-starvation did not lead to a drastic loss of attached *P. putida* F1 cells, and full biodegradation capacity could be regained within a quarter of a day, after four months of toluene-starvation, in the column experiments (chapter 7), and within less than two days, after two weeks of toluene-starvation, in the two-dimensional flow-through microcosm experiments (chapter 5).

The results of additional flow-through microcosm experiments conducted by Kürzinger (2007) with heterogeneous sand fillings, and the field-scale conservative-transport simulations presented in chapter 6, indicate that aquifer heterogeneity buffers the effect of plume dynamics on in situ biodegradation, if the plume fringe is focused in the same high-conductivity zones before and after plume fluctuation. Especially small scale fluctuations in the position of the plume source in the order of 10 to 20 *cm* could be shown

to be almost completely compensated by the effect of flow focusing in heterogeneous media.

Open questions

So far experiments were only performed for toluene degradation by the specific toluene degrader *P. putida* F1 under aerobic conditions. Further experiments with natural microbial communities might be conducted to see if the findings can be generalized. Furthermore, oxygen is only present in trace amounts at many contaminated sites, and contaminant degradation in the field is, therefore, dominated by anaerobic processes (e.g., Wiedemeier et al., 1999; Lovely, 2001; Fischer et al., 2007; Anneser et al., 2008). Comparing intrinsic biodegradation at 38 BTEX-contaminated sites, Wiedemeier et al. (1999) found that sulfate reduction is the dominant electron accepting process, accounting for 70% of intrinsic biodegradation, whereas aerobic respiration was estimated to account only for 3% of intrinsic biodegradation. So far, it is not clear if the results from the aerobic laboratory-scale systems can be transfered to biodegradation under sulfate reducing conditions, which is energetically way less favorable than aerobic biodegradation, and where microbial growth and hence contaminant degradation rates are much smaller (Rittmann and McCarty, 2001).

In the indoor aquifer model experiment (see chapter 4) as well as in the column experiments (see chapter 7), we observed less oxygen consumption for toluene degradation than anticipated for complete toluene oxidation. So far this finding could not be finally resolved. It might be helpful to conduct column experiments under nitrate reducing conditions in the future, to see if the nitrate demand for toluene degradation in the column system shows the same pattern.

8.3 What did/can reactive-transport modeling contribute?

In this thesis I applied reactive-transport modeling to quantify the effects of coupled (bio)geochemical and physical processes on organic contaminants an their stable-carbon isotope ratio under steady-state as well as under transient environmental conditions. In the following I list the contributions to the individual studies, I see in the quantitative model-based data analysis.

- The model-based analysis of the toluene-pulse experiment enabled the separation of the individual contributions of biodegradation, sorption and transverse dispersion on the stable-carbon isotope signature of toluene (see chapter 4), which would have been impossible to do solely experimentally with the experimental setup, which was aimed to represent in-situ field conditions as close as possible.

- By means of reactive-transport simulations the ambivalent effect of transverse dispersion on isotope fractionation in fringe-controlled biodegradation, i.e., the attenuating effect on reaction-induced isotope fractionation by mixing limitations, and the enhancing effect by dispersion-induced isotope fractionation, could be elaborated (see chapter 3). In reality both effects act inevitable together and cannot be separated experimentally.

- Different conceptual models for the behavior of bacteria under toluene-starvation conditions were tested in chapter 5. By the comparison of experimental and simulation results it could be ruled out that microbial growth and decay are responsible for the observed lag phases in toluene degradation after the toluene plume was shifted back to its previous position.

- Based on the high-resolution dataset of attached and suspended *P. putida* F1 cell numbers for the column experiments presented in chapter 7, a quantitative model for microbial growth in porous media, explicitly accounting for peak cell detachment under growth conditions, could be developed.

While the examples listed above show the great potential for reactive-transport modeling as tool to separate the individual effects of coupled biological and physical processes on contaminant fate and transport, the misfit between the observed and simulated $\delta^{13}C$ breakthrough in the toluene-pulse experiment (see Fig. 4.4), as well as the underestimation of the lag phase in toluene degradation after the first plume displacement in the flow-through microcosm experiment (see Fig. 5.8), however, also indicate that the full complexity of the biologically controlled systems investigated in this thesis could not be captured by the models. Therefore, predictive simulations should be treated with caution, especially when models, which were calibrated to laboratory-scale experiments, are applied to predict contaminant fate and transport on the field scale, the ultimate goal of any model development.

Appendix A

Relationship between reaction stoichiometry and specific yield

The redox half reactions for toluene oxidation R_{tol} and oxygen reduction R_{ox}, written for one electron equivalent, read as:

$$\frac{1}{36}C_7H_8 + \frac{14}{36}H_2O \longrightarrow \frac{7}{36}CO_2 + H^+ + e^- \tag{A.1}$$

$$\frac{9}{36}O_2 + e^- + H^+ \longrightarrow \frac{18}{36}H_2O \tag{A.2}$$

Conceptualizing the biomass as chemical species $C_5H_7O_2N$ and considering ammonium as sole nitrogen source for growth (Rittmann and McCarty, 2001) the chemical equation for biomass synthesis R_{bio} reads as:

$$\frac{1}{5}CO_2 + \frac{1}{20}HCO_3^- + \frac{1}{20}NH_4^+ + H^+ + e^- \longrightarrow \frac{1}{20}C_5H_7O_2N + \frac{9}{20}H_2O \tag{A.3}$$

Combining the three half reactions R_{tol}, R_{ox} R_{bio} yields the overall chemical equation for toluene oxidation coupled to biomass growth:

$$R_{overall} = R_{tol} + f_e \times R_{ox} + f_s \times R_{bio} \tag{A.4}$$

in which f_e $[-]$ and f_s $[-]$ are the fraction of electrons transferred to oxygen and used for synthesis of new cellular material, respectively.

Considering the cell yield Y, an average carbon content of one cell of $M_{cell} = 130$ $fg/cell$ obtained in batch experiments, the molar mass of toluene ($M_{tol} = 92.15 mg/mmol$) and the mass of carbon in one mole $C_5H_7O_2N$ ($M_{bio-C} = 60\ mg/mmol$) the fraction of electrons incorporated into biomass f_s can be calculated by:

$$f_s = Y \times M_{cell} \times \frac{M_{tol}}{M_{bio-C}} \times \frac{20}{36} \tag{A.5}$$

While a fraction of electrons of $f_s = 0.35$ is incorporated into the biomass the majority of electrons ($f_e = 0.65$) are transferred to the electron acceptor O_2 to gain energy for cell synthesis.

The stoichiometric coefficients for oxygen consumption due to growth $f_{gr} = 2\ mg_{ox}/mg_{tol}$ and endogeneous respiration $f_{dec} = 1.1\ mg_{ox}/mg_{tol}$ are obtained by multiplying the oxygen demand for the complete mineralization of one mg toluene $f_{ox} = 3.1\ mg_{ox}/mg_{tol}$ with f_e and f_s, respectively.

Appendix B

Incomplete toluene mineralization

Complete mineralization of toluene to carbon dioxide and water yields a stoichiometry of 9 mol oxygen per mol of toluene:

$$C_7H_8 + 9O_2 \rightarrow 7CO_2 + 4H_2O, \tag{B.1}$$

which corresponds to 3.1 mg oxygen per mg of toluene. The inferred stoichiometry of the reaction, however, was 1.5 mg oxygen per mg of toluene, which might indicate incomplete degradation of toluene (Figure 4.7). One potential central metabolite in aerobic toluene degradation pathways is catechol ($C_6H_6O_2$) (e.g., Fuchs et al., 2011). Partial oxidation of toluene to catechol requires 2.5 mol oxygen per mol of toluene:

$$C_7H_8 + 2.5O_2 \rightarrow C_6H_6O_2 + CO_2 + H_2O, \tag{B.2}$$

which corresponds to 0.86 mg oxygen per mg toluene. To match the observed consumption of approximately 1.5 mg_{O_2}/mg_{tol}, 30% of the toluene have to be oxidized to carbon dioxide and 70 % to the intermediate product catechol.

Catechol is chosen here as potential product of incomplete toluene oxidation. Chemical analysis of the water samples, however, did not include concentrations of metabolites. An alternative explanation would be the utilization of toluene as a growth-substrate. However, in a continuous toluene-injection experiment performed after the pulse experiment (Herzyk, 2013), no significant biomass growth was observed. During the pulse experiment itself, no samples for the quantification of biomass were taken.

Appendix C

Simulation results of model 2

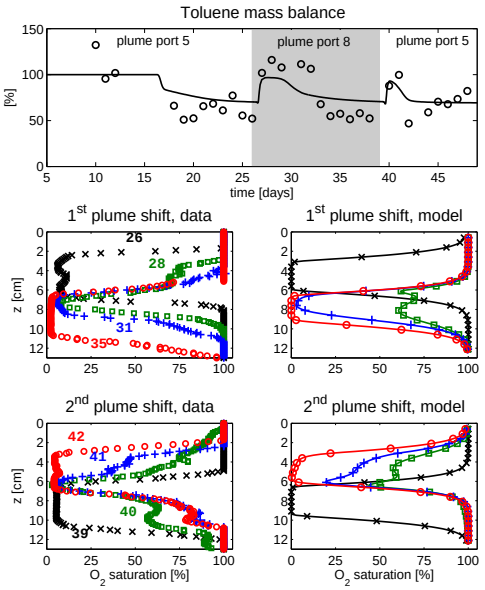

Figure C.1: *Comparison of experimental data for the toluene mass balance (upper panel) and profiles of dissolved oxygen at x=74 cm (mid and lower panel) to the model outcome of model 2, in which endogenous respiration, as well as the ability of microorganisms to switch between an active and an inactive (dormant) state, is neglected.*

Figure C.1 shows the simulation results for model 2, which neglects endogenous respiration of microorganisms in the absence of toluene and the ability of microorganisms to switch between an active and an inactive (dormant) state. The two major model parameters, the maximum specific growth rate μ_{max} and the non-mechanistic, lumped decay

coefficient k_{dec} (see Table 5.3) were calibrated to match the observed toluene mass balance and the vertical oxygen profiles as well as possible, which resulted in the rather large value for the decay coefficient of 0.5 d^{-1}. Since endogenous respiration is not considered in the model, the observed oxygen depletion for regions where the toluene plume has already been washed out, can not be reproduced.

Bibliography

Abe, Y. and Hunkeler, D. (2006). Does the rayleigh equation apply to evaluate field isotope data in contaminant hydrogeology? *Environmental Science & Technology*, 40(5):1588–1596.

Aeppli, C., Berg, M., Cirpka, O. A., Holliger, C., Schwarzenbach, R. P., and Hofstetter, T. B. (2009). Influence of mass-transfer limitations on carbon isotope fractionation during microbial dechlorination of trichloroethene. *Environmental Science & Technology*, 43(23):8813–8820.

Anneser, B. (2008). *Spatial and temporal dynamics of biogeochemical gradients in a tar oil-contaminated porous aquifer - biodegradation processes revealed by high-resolution measurements*. PhD thesis, Eberhard Karls Universität Tübingen.

Anneser, B., Einsiedl, F., Meckenstock, R. U., Richters, L., Wisotzky, F., and Griebler, C. (2008). High-resolution monitoring of biogeochemical gradients in a tar oil-contaminated aquifer. *Applied Geochemistry*, 23(6):1715 – 1730.

Anneser, B., Pilloni, G., Bayer, A., Lueders, T., Griebler, C., Einsiedl, F., and Richters, L. (2010). High resolution analysis of contaminated aquifer sediments and groundwater - what can be learned in terms of natural attenuation? *Geomicrobiology Journal*, 27:130–142.

Anneser, B., Richter, L., and Griebler, C. (2007). Identification and localization of redox processes in an aromatic hydrocarbon plume via high-resolution sampling of biotic and abiotic gradients. In *International Conference on Water Pollution in natural Porous media at different scales*, pages 339–345.

Atteia, O., Franceschi, M., and Dupuy, A. (2008). Validation of reactive model assumptions with isotope data: Application to the Dover case. *Environmental Science & Technology*, 42(9):3289–3295.

Ballarini, E., Beyer, C., Bauer, R., Griebler, C., and Bauer, S. (2014). Model based evaluation of a contaminant plume development under aerobic and anaerobic conditions in 2D bench-scale tank experiments. *Biodegradation*, 25(3):351–371.

Bär, M., Hardenberg, J., Meron, E., and Provenzale, A. (2002). Modelling the survival of bacteria in drylands: the advantage of being dormant. *Proceedings of the Royal Society of London. Series B: Biological Sciences*, 269(1494):937–942.

Barry, D., Prommer, H., Miller, C., Engesgaard, P., Brun, A., and Zheng, C. (2002). Modelling the fate of oxidisable organic contaminants in groundwater. *Advances in Water Resources*, 25(8–12):945 – 983.

Bauer, R. D., Maloszewski, P., Zhang, Y., Meckenstock, R. U., and Griebler, C. (2008). Mixing-controlled biodegradation in a toluene plume: Results from two-dimensional laboratory experiments. *Journal of Contaminant Hydrology*, 96(1-4):150 – 168.

Bauer, R. D., Rolle, M., Bauer, S., Eberhardt, C., Grathwohl, P., Kolditz, O., Meckenstock, R. U., and Griebler, C. (2009a). Enhanced biodegradation by hydraulic heterogeneities in petroleum hydrocarbon plumes. *Journal of Contaminant Hydrology*, 105(1-2):56 – 68.

Bauer, R. D., Rolle, M., Kürzinger, P., Grathwohl, P., Meckenstock, R. U., and Griebler, C. (2009b). Two-dimensional flow-through microcosms - versatile test systems to study biodegradation processes in porous aquifers. *Journal of Hydrology*, 369:284 – 295.

Bayer, P., Huggenberger, P., Renard, P., and Comunian, A. (2011). Three-dimensional high resolution fluvio-glacial aquifer analog: Part 1: Field study. *Journal of Hydrology*, 405(1–2):1 – 9.

Bombach, P., Richnow, H., Kästner, M., and Fischer, A. (2010). Current approaches for the assessment of in situ biodegradation. *Applied Microbiology and Biotechnology*, 86(3):839–852.

Bosma, T. N. P., Middeldorp, P. J. M., Schraa, G., and Zehnder, A. J. B. (1997). Mass transfer limitation of biotransformation: Quantifying bioavailability. *Environmental Science & Technology*, 31(1):248–252.

Bouchard, D., Hunkeler, D., Gaganis, P., Aravena, R., Höhener, P., Broholm, M. M., and Kjeldsen, P. (2008). Carbon isotope fractionation during diffusion and biodegradation of petroleum hydrocarbons in the unsaturated zone: Field experiment at værløse

airbase, denmark, and modeling. *Environmental Science & Technology*, 42(2):596–601.

Braeckevelt, M., Fischer, A., and Kästner, M. (2012). Field applicability of compound-specific isotope analysis (CSIA) for characterization and quantification of in situ contaminant degradation in aquifers. *Applied Microbiology and Biotechnology*, 94(6):1401–1421.

Brusseau, M. L., Hu, M. Q., Wang, J.-M., and Maier, R. M. (1999). Biodegradation during contaminant transport in porous media. 2. the influence of physicochemical factors. *Environmental Science & Technology*, 33(1):96–103.

Centler, F., Hesse, F., and Thullner, M. (2013). Estimating pathway-specific contributions to biodegradation in aquifers based on dual isotope analysis: Theoretical analysis and reactive transport simulations. *Journal of Contaminant Hydrology*, 152(0):97 – 116.

Chakraborty, R. and Coates, J. (2004). Anaerobic degradation of monoaromatic hydrocarbons. *Applied Microbiology and Biotechnology*, 64(4):437–446.

Chiogna, G., Cirpka, O., Grathwohl, P., and Rolle, M. (2011a). Relevance of local compound-specific transverse dispersion for conservative and reactive mixing in heterogeneous porous media. *Water Resources Research*, 47:W07540.

Chiogna, G., Cirpka, O., Grathwohl, P., and Rolle, M. (2011b). Transverse mixing of conservative and reactive tracers in porous media: Quantification through the concepts of flux-related and critical dilution indices. *Water Resources Research*, 47:W02505.

Chiogna, G., Eberhardt, C., Gratwohl, P., Cirpka, O. A., and Rolle, M. (2010). Evidence of compound-dependent hydrodynamic and mechanical transverse dispersion by multitracer laboratory experiments. *Environmental Science & Technology*, 44:688–693.

Chrysikopoulos, C. V., Syngouna, V. I., Vasiliadou, I. A., and Katzourakis, V. E. (2012). Transport of Pseudomonas Putida in a 3-D bench scale experimental aquifer. *Transport in Porous Media,*, 94:617–642.

Chu, M., Kitanidis, P. K., and McCarty, P. L. (2005). Modeling microbial reactions at the plume fringe subject to transverse mixing in porous media: When can the rates

of microbial reaction be assumed to be instantaneous? *Water Resources Research*, 41(6):W06002.

Cirpka, O. A. (1997). *Numerische Methoden zur Simulation des reaktiven Mehrkomponententransports im Grundwasser*. PhD thesis, University of Stuttgart.

Cirpka, O. A. (2005). Effects of sorption on transverse mixing in transient flows. *Journal of Contaminant Hydrology*, 78(3):207–229.

Cirpka, O. A. and Attinger, S. (2003). Effective dispersion in heterogeneous media under random transient flow conditions. *Water Resources Research*, 39(9):1257.

Cirpka, O. A., de Barros, F. P. J., Chiogna, G., Rolle, M., and Nowak, W. (2011). Stochastic flux-related analysis of transverse mixing in two-dimensional heterogeneous porous media. *Water Resources Research*, 47:W06515.

Cirpka, O. A., Frind, E. O., and Helmig, R. (1999a). Numerical methods for reactive transport on rectangular and streamline-oriented grids. *Advances in Water Resources*, 22(7):711 – 728.

Cirpka, O. A., Frind, E. O., and Helmig, R. (1999b). Numerical simulation of biodegradation controlled by transverse mixing. *Journal of Contaminant Hydrology*, 40(2):159 – 182.

Cirpka, O. A., Frind, E. O., and Helmig, R. (1999c). Streamline-oriented grid generation for transport modelling in two-dimensional domains including wells. *Advances in Water Resources*, 22(7):697 – 710.

Cirpka, O. A., Rolle, M., Chiogna, G., de Barros, F. P. J., and Nowak, W. (2012). Stochastic evaluation of mixing-controlled steady-state plume lengths in two-dimensional heterogeneous domains. *Journal of Contaminant Hydrology*, 138:22–39.

Cirpka, O. A. and Valocchi, A. J. (2007). Two-dimensional concentration distribution for mixing-controlled bioreactive transport in steady state. *Advances in Water Resources*, 30(6-7):1668 – 1679.

Cirpka, O. A. and Valocchi, A. J. (2009). Reply to comments on "two-dimensional concentration distribution for mixing-controlled bioreactive transport in steady state" by h. shao et al. *Advances in Water Resources*, 32(2):298 – 301.

Clement, T., Peyton, B., Skeen, R., Jennings, D., and Petersen, J. (1997). Microbial growth and transport in porous media under denitrification conditions: experiments and simulations. *Journal of Contaminant Hydrology*, 24(3–4):269 – 285.

Cunningham, J. A., Rahme, H., Hopkins, G. D., Lebron, C., and Reinhard, M. (2001). Enhanced in situ bioremediation of BTEX-contaminated groundwater by combined injection of nitrate and sulfate. *Environmental Science & Technology*, 35(8):1663–1670.

Cussler, E. (2009). *Diffusion: Mass Transfer in Fluid Systems*. Cambridge University Press, New York, third edition.

D'Affonseca, F. M., Prommer, H., Finkel, M., Blum, P., and Grathwohl, P. (2011). Modeling the long-term and transient evolution of biogeochemical and isotopic signatures in coal tar-contaminated aquifers. *Water Resources Research*, 47(5):W05518.

Davis, T. A. and Duff, I. S. (1997). An unsymmetric-pattern multifrontal method for sparse LU factorization. *SIAM Journal on Matrix Analysis and Application*, 18:140–158.

Díaz, E., Jiménez, J. I., and Nogales, J. (2013). Aerobic degradation of aromatic compounds. *Current Opinion in Biotechnology*, 24(3):431 – 442.

Ding, D. (2010). Transport of bacteria in aquifer sediment: experiments and modeling. *Hydrogeology Journal*, 18(3):669–679.

Dykaar, B. B. and Kitanidis, P. K. (1996). Macrotransport of a biologically reacting solute through porous media. *Water Resources Research*, 32(2):307–320.

Eckert, D. (2011). Isotope fractionation in mixing-controlled bioreactive transport. Master's thesis, University of Tübingen.

Eckert, D., Kürzinger, P., Bauer, R., Griebler, C., and Cirpka, O. A. (2015). Fringe-controlled biodegradation under dynamic conditions: Quasi 2-d flow-through experiments and reactive-transport modeling. *Journal of Contaminant Hydrology*, 172:100 – 111.

Eckert, D., Qiu, S., Elsner, M., and Cirpka, O. A. (2013). Model complexity needed for quantitative analysis of high resolution isotope and concentration data from a toluene-pulse experiment. *Environmental Science & Technology*, 47(13):6900–6907.

Eckert, D., Rolle, M., and Cirpka, O. A. (2012). Numerical simulation of isotope fractionation in steady-state bioreactive transport controlled by transverse mixing. *Journal of Contaminant Hydrology*, 140:95–106.

Elsner, M. (2010). Stable isotope fractionation to investigate natural transformation mechanisms of organic contaminants: principles, prospects and limitations. *Journal of Environmental Monitoring*, 12:2005–2031.

Elsner, M., Zwank, L., Hunkeler, D., and Schwarzenbach, R. P. (2005). A new concept linking observable stable isotope fractionation to transformation pathways of organic pollutants. *Environmental Science & Technology*, 39:6896–6916.

Fischer, A., Theuerkorn, K., Stelzer, N., Gehre, M., Thullner, M., and Richnow, H. H. (2007). Applicability of stable isotope fractionation analysis for the characterization of benzene biodegradation in a BTEX-contaminated aquifer. *Environmental Science & Technology*, 41(10):3689–3696.

Fry, V. A., Istok, J. D., Semprini, L., O'Reilly, K. T., and Buscheck, T. E. (1995). Retardation of dissolved oxygen due to a trapped gas phase in porous media. *Groundwater*, 33(3):391–398.

Fry, V. A., Selker, J. S., and Gorelick, S. M. (1997). Experimental investigations for trapping oxygen gas in saturated porous media for in situ bioremediation. *Water Resources Research*, 33(12):2687–2696.

Fuchs, G., Boll, M., and Heider, J. (2011). Microbial degradation of aromatic compounds - from one strategy to four. *Nature Reviews Microbiology*, 9:803–816.

Ghoshal, S., Ramaswami, A., and Luthy, R. G. (1996). Biodegradation of naphthalene from coal tar and heptamethylnonane in mixed batch systems. *Environmental Science & Technology*, 30(4):1282–1291.

Ginn, T. R., Wood, B. D., Nelson, K. E., Scheibe, T. D., Murphy, E. M., and Clement, T. (2002). Processes in microbial transport in the natural subsurface. *Advances in Water Resources*, 25(8–12):1017 – 1042.

Green, C. T., Boehlke, J. K., Bekins, B. A., and Phillips, S. P. (2010). Mixing effects on apparent reaction rates and isotope fractionation during denitrification in a heterogeneous aquifer. *Water Resources Research*, 46:W08525.

Griebler, C., Mindl, B., Slezak, D., and Geiger-Kaiser, M. (2002). Distribution patterns of attached and suspended bacteria in pristine and contaminated shallow aquifers studied with an in situ sediment exposure microcosm. *Aquatic Microbial Ecology*, 28(2):117–129.

Haberer, C. M., Rolle, M., Liu, S., Cirpka, O. A., and Grathwohl, P. (2011). A high-resolution non-invasive approach to quantify oxygen transport across the capillary fringe and within the underlying groundwater. *Journal of Contaminant Hydrology*, 122(1-4):26–39.

Harvey, R. W. and Garabedian, S. P. (1991). Use of colloid filtration theory in modeling movement of bacteria through a contaminated sandy aquifer. *Environmental Science & Technology*, 25(1):178–185.

Hazen, A. (1893). Some physical properties of sands and gravels, with special reference to their use in filtration. *In twenty-fourth annual report of the State Board of Health of Massachusetts, Publ. Doc. of Mass. 34, edited by H.P. Walcott et al.*

Hazen, T., Jiménez, L., López de Victoria, G., and Fliermans, C. (1991). Comparison of bacteria from deep subsurface sediment and adjacent groundwater. *Microbial Ecology*, 22(1):293–304.

Heinz, J., Kleineidam, S., Teutsch, G., and Aigner, T. (2003). Heterogeneity patterns of Quaternary glaciofluvial gravel bodies (SW-Germany): application to hydrogeology. *Sedimentary Geology*, 158(1–2):1 – 23.

Herzer, J. and Kinzelbach, W. (1989). Coupling of transport and chemical processes in numerical transport models. *Geoderma*, 44(2–3):115 – 127.

Herzyk, A., Maloszewski, P., Qiu, S., Elsner, M., and Griebler, C. (2014). Intrinsic potential for immediate biodegradation of toluene in a pristine, energy-limited aquifer. *Biodegradation*, 25(3):325–336.

Herzyk, A. M. (2013). *Resilience and resistance of a pristine aquifer towards toluene contamination - impact assessment using microbes and elucidation of factors limiting natural attenuation*. PhD thesis, TU München.

Hesse, F., Radu, F., Thullner, M., and Attinger, S. (2009). Upscaling of the advection-diffusion-reaction equation with monod reaction. *Advances in Water Resources*, 32(8):1336 – 1351.

Hoehener, P. and Yu, X. (2012). Stable carbon and hydrogen isotope fractionation of dissolved organic groundwater pollutants by equilibrium sorption. *Journal of Contaminant Hydrology*, 129-130:54 – 61.

Hofstetter, T. B., Schwarzenbach, R. P., and Bernasconi, S. M. (2008). Assessing transformation processes of organic compounds using stable isotope fractionation. *Environmental Science & Technology*, 42(21):7737–7743.

Holm, P., Nielsen, P., Albrechtsen, H., and Christensen, T. (1992). Importance of unattached bacteria and bacteria attached to sediment in determining potentials for degradation of xenobiotic organic contaminants in an aerobic aquifer. *Applied and Environmental Microbiology*, 58(9):3020–3026.

Huang, W., Oswald, S., Lerner, D., Smith, C., and Zheng, C. (2003). Dissolved oxygen imaging in a porous medium to investigate biodegradation in a plume with limited electron acceptor supply. *Environmental Science & Technology*, 37(9):1905–1911.

Hunkeler, D., Chollet, N., Pittet, X., Aravena, R., Cherry, J., and Parker, B. (2004). Effect of source variability and transport processes on carbon isotope ratios of TCE and PCE in two sandy aquifers. *Journal of Contaminant Hydrology*, 74(1-4):265 – 282.

Hunkeler, D., Jörger, D., Häberli, K., Höhener, P., and Zeyer, J. (1998). Petroleum hydrocarbon mineralization in anaerobic laboratory aquifer columns. *Journal of Contaminant Hydrology*, 32(1–2):41 – 61.

Hünniger, M. (2011). *Development of experimental, monitoring, and mathematical methods to quantify water fluxes and transport in heterogeneous aquifer system models*. PhD thesis, Albert-Ludwigs-Universitaẗ Freiburg.

Jin, B., Haderlein, S. B., and Rolle, M. (2013). Integrated carbon and chlorine isotope modeling: Applications to chlorinated aliphatic hydrocarbons dechlorination. *Environmental Science & Technology*, 47(3):1443–1451.

Jin, B., Rolle, M., Li, T., and Haderlein, S. B. (2014). Diffusive fractionation of BTEX and chlorinated ethenes in aqueous solution: Quantification of spatial isotope gradients. *Environmental Science & Technology*, 48(11):6141–6150.

Jobelius, C., Ruth, B., Griebler, C., Meckenstock, R. U., Hollender, J., Reineke, A., Frimmel, F. H., and Zwiener, C. (2011). Metabolites indicate hot spots of biodegradation and biogeochemical gradients in a high-resolution monitoring well. *Environmental Science & Technology*, 45(2):474–481.

Jordan, F. L., Sandrin, S. K., Frye, R. J., Brusseau, M. L., and Maier, R. M. (2004). The influence of system complexity on bacterial transport in saturated porous media. *Journal of Contaminant Hydrology*, 74(1–4):19 – 38.

Kampara, M., Thullner, M., Richnow, H. H., Harms, H., and Wick, L. Y. (2008). Impact of bioavailability restrictions on microbially induced stable isotope fractionation. 2. experimental evidence. *Environmental Science & Technology*, 42(17):6552–6558.

Kaprelyants, A., Gottschal, J., and Kell, D. (1993). Dormancy in non-sporulating bacteria. *FEMS Microbiology Letters*, 104(3-4):271–286.

Kaprelyants, A. and Kell, D. (1993). Dormancy in stationary-phase cultures of micrococcus luterus: flow cytometric analysis of starvation and resuscitation. *Applied and Environmental Microbiology*, 59:3187–3196.

Kelly, W. R., Hornberger, G. M., Herman, J. S., and Aaron, L. M. (1996). Kinetics of BTX biodegradation and mineralization in batch and column systems. *Journal of Contaminant Hydrology*, 23:113–132.

Klenk, I. and Grathwohl, P. (2002). Transverse vertical dispersion in groundwater and the capillary fringe. *Journal of Contaminant Hydrology*, 58(1–2):111 – 128.

Knutson, C., Valocchi, A., and Werth, C. (2007). Comparison of continuum and pore-scale models of nutrient biodegradation under transverse mixing conditions. *Advances in Water Resources*, 30(6–7):1421 – 1431.

Kopinke, F.-D., Georgi, A., Voskamp, M., and Richnow, H. H. (2005). Carbon isotope fractionation of organic contaminants due to retardation on humic substances: Implications for natural attenuation studies in aquifers. *Environmental Science & Technology*, 39(16):6052–6062. PMID: 16173563.

Kuder, T., Philp, P., and Allen, J. (2009). Effects of volatilization on carbon and hydrogen isotope ratios of MTBE. *Environmental Science & Technology*, 43(6):1763–1768.

Kürzinger, P. (2007). Aerobic degradation in transient tolue plumes in porous media - experiments in 2-D model aquifer microcosms. Master's thesis, TU Munich.

LABO (2009). Berücksichtigung der natürlichen Schadstoffminderung bei der Altlastenbearbeitung. Ständiger Ausschnuss Altlasten - ALA. Mainz, Germany.

LaBolle, E. M., Fogg, G. E., Eweis, J. B., Gravner, J., and Leaist, D. G. (2008). Isotope fractionation by diffusion in groundwater. *Water Resources Research*, 44:W07405.

Lennon, J. T. and Jones, S. E. (2011). Microbial seed banks: the ecological and evolutionary implications of dormancy. *Nature Reviews Microbiology*, 9(2):119–130.

Liu, C. and Zachara, J. M. (2001). Uncertainties of monod kinetic parameters nonlinearly estimated from batch experiments. *Environmental Science & Technology*, 35(1):133–141.

Lovely, D. R. (2001). Anaerobes to the rescue. *Science*, 293(5534):1444–1446.

Maggi, F. and Riley, W. J. (2010). Mathematical treatment of isotopologue and isotopomer speciation and fractionation in biochemical kinetics. *Geochimica et Cosmochimica Acta*, 74(6):1823 – 1835.

Maier, U. and Grathwohl, P. (2006). Numerical experiments and field results on the size of steady state plumes. *Journal of Contaminant Hydrology*, 85:33 – 52.

Mak, K., Griebler, C., Meckenstock, R., Liedl, R., and Peter, A. (2006). Combined application of conservative transport modelling and compound-specific carbon isotope analyses to assess in situ attenuation of benzene, toluene, and o-xylene. *Journal of Contaminant Hydrology*, 88(3-4):306 – 320.

Mason, C. A., Hamer, G., and Bryers, J. (1986). The death and lysis of microorganisms in environmental processes. *FEMS Microbiology Letters*, 39:373–401.

Mayer, K., Benner, S., Frind, E., Thornton, S., and Lerner, D. (2001). Reactive transport modeling of processes controlling the distribution and natural attenuation of phenolic compounds in a deep sandstone aquifer. *Journal of Contaminant Hydrology*, 53(3–4):341 – 368.

Meckenstock, R. U., Morasch, B., Griebler, C., and Richnow, H. H. (2004). Stable isotope fractionation analysis as a tool to monitor biodegradation in contaminated acquifers. *Journal of Contaminant Hydrology*, 75(3-4):215 – 255.

Meile, C. and Tuncay, K. (2006). Scale dependence of reaction rates in porous media. *Advances in Water Resources*, 29(1):62 – 71.

Mellage, A. A. (2014). Fringe-controlled biodegradation under dynamic plume conditions: flow-through experiments and reactive-transport modeling. Master's thesis, University of Tübingen.

Mills, R. (1973). Self-diffusion in normal and heavy water in the range 1-45 °C. *Journal of Physical Chemistry*, 77(5):685–688.

Mills, R. (1976). Diffusion relationships in the binary system benzene-perdeuterated benzene at 25°C. *Journal of Physical Chemistry*, 80:888–890.

Morshed, J. and Kaluarachchi, J. J. (1995). Critical assessment of the operator-splitting technique in solving the advection-dispersion-reaction equation: 2. monod kinetics and coupled transport. *Advances in Water Resources*, 18(2):101 – 110.

Murphy, E. and Ginn, T. (2000). Modeling microbial processes in porous media. *Hydrogeology Journal*, 8(1):142–158.

Murphy, E., Ginn, T., Brockmann, F., and D.R., B. (1997a). Growth effetcs on the partitioning and transport of bacteria. In *American Geophysical Union Fall Meeting, San Francisco*.

Murphy, E., Ginn, T., Chilakapati, A., Resch, C., Phillips, J., Wietsma, T., and Spadoni, C. (1997b). The influence of physical heterogeneity on microbial degradation and distribution in porous media. *Water Resources Research*, 33(5):1087–1103.

Northrop, D. (1981). The expression of isotope effects on enzyme-catalyzed reactions. *Anual Review of Biochemistry*, 50:103–131.

Panagos, P., Van Liedekerke, M., Yigini, Y., and Montanarella, L. (2013). Contaminated sites in Europe: Review of the current situation based on data collected through a european network. *Journal of Environmental and Public Health*, vol. 2013:Article ID 158764.

Parales, R., Parales, J., Pelletier, D., and Ditty, J. (2008). Chapter 1 Diversity of microbial toluene degradation pathways. volume 64 of *Advances in Applied Microbiology*, pages 1 – 73. Academic Press.

Peter, A., Steinbach, A., Liedl, R., Ptak, T., Michaelis, W., and Teutsch, G. (2004). Assessing microbial degradation of o-xylene at field-scale from the reduction in mass flow rate combined with compound-specific isotope analyses. *Journal of Contaminant Hydrology*, 71(1-4):127 – 154.

Pooley, K. E., Blessing, M., Schmidt, T. C., Haderlein, S. B., MacQuarrie, K. T. B., and Prommer, H. (2009). Aerobic biodegradation of chlorinated ethenes in a fractured bedrock aquifer: Quantitative assessment by compound-specific isotope analysis (CSIA) and reactive transport modeling. *Environmental Science & Technology*, 43(19):7458–7464.

Press, W. H., Teutolsky, S., Vetterling, W. T., and Flannery, B. (1997). *Numerical Recipes in Fortran 77. The Art of Scientific Computing*. Cambridge University Press, second edition.

Prommer, H., Anneser, B., Rolle, M., Einsiedl, F., and Griebler, C. (2009). Biogeochemical and isotopic gradients in a BTEX/PAH contaminant plume: Model-based interpretation of a high-resolution field data set. *Environmental Science & Technology*, 43(21):8206–8212.

Prommer, H., Aziz, L. H., Bolaño, N., Taubald, H., and Schüth, C. (2008). Modelling of geochemical and isotopic changes in a column experiment for degradation of TCE by zero-valent iron. *Journal of Contaminant Hydrology*, 97(1–2):13 – 26.

Prommer, H., Barry, D., and Davis, G. (2002). Modelling of physical and reactive processes during biodegradation of a hydrocarbon plume under transient groundwater flow conditions. *Journal of Contaminant Hydrology*, 59(1–2):113 – 131.

Prommer, H., Tuxen, N., and Bjerg, P. L. (2006). Fringe-controlled natural attenuation of phenoxy acids in a landfill plume: Integration of field-scale processes by reactive transport modeling. *Environmental Science & Technology*, 40(15):4732–4738.

Qiu, S. (2014). *Investigation into the fate of groundwater contaminants using compound specific isotope analysis*. PhD thesis, University of Tübingen.

Qiu, S., Eckert, D., Cirpka, O. A., Huenniger, M., Knappett, P., Maloszewski, P., Meckenstock, R. U., Griebler, C., and Elsner, M. (2013). Direct experimental evidence of non-first order degradation kinetics and sorption-induced isotopic fractionation in a mesoscale aquifer: 13C/12C analysis of a transient toluene pulse. *Environmental Science & Technology*, 47(13):6892–6899.

Reardon, K., Mosteller, D., and Rogers, J. (2000). Biodegradation kinetics of benzene, toluene, and phenol as single and mixed substrates for Pseudomonas putida F1. *Biotechnology and Bioengineering*, 69(4):385–400.

Rees, H. C., Oswald, S. E., Banwart, S. A., Pickup, R. W., and Lerner, D. N. (2007). Biodegradation processes in a laboratory-scale groundwater contaminant plume assessed by fluorescence imaging and microbial analysis. *Applied and Environmental Microbiology*, 73(12):3865–3876.

Richnow, H. H., Annweiler, E., Michaelis, W., and Meckenstock, R. U. (2003). Microbial in situ degradation of aromatic hydrocarbons in a contaminated aquifer monitored by carbon isotope fractionation. *Journal of Contaminant Hydrology*, 65(1-2):101 – 120.

Rittmann, B. and McCarty, P. (2001). *Environmental biotechnology: principles and applications*. McGraw-Hill.

Röling, W. F. M., van Breukelen, B. M., Braster, M., Lin, B., and van Verseveld, H. W. (2001). Relationships between microbial community structure and hydrochemistry in a landfill leachate-polluted aquifer. *Applied and Environmental Microbiology*, 67:4619–4629.

Rolle, M., Chiogna, G., Bauer, R., Griebler, C., and Grathwohl, P. (2010). Isotopic fractionation by transverse dispersion: Flow-through microcosms and reactive transport modeling study. *Environmental Science & Technology*, 44(16):6167–6173.

Rolle, M., Eberhardt, C., Chiogna, G., Cirpka, O. A., and Grathwohl, P. (2009). Enhancement of dilution and transverse reactive mixing in porous media: Experiments and model-based interpretation. *Journal of Contaminant Hydrology*, 110(3-4):130 – 142.

Rolle, M., Hochstetler, D., Chiogna, G., Kitanidis, P., and Grathwohl, P. (2012). Experimental investigation and pore-scale modeling interpretation of compound-specific transverse dispersion in porous media. *Transport in Porous Media*, 93(3):347–362.

Roszak, D. and Colwell, R. (1987). Survival strategies of bacteria in the natural environment. *Microbiological Reviews*, 51:365–379.

Schäfer, D., Schäfer, W., and Kinzelbach, W. (1998). Simulation of reactive processes related to biodegradation in aquifers: 1. structure of the three-dimensional reactive transport model. *Journal of Contaminant Hydrology*, 31(1–2):167 – 186.

Scheibe, T. D., Hubbard, S. S., Onstott, T. C., and DeFlaun, M. F. (2011). Lessons learned from bacterial transport research at the south oyster site. *Ground Water*, 49(5):745–763.

Scheidegger, A. E. (1961). General theory of disersion in porous media. *Journal of Geophysical Research*, 66(4):3237–3278.

Schirmer, M., Butler, B. J., Roy, J. W., Frind, E. O., and Barker, J. F. (1999). A relative-least-squares technique to determine unique monod kinetic parameters of BTEX compounds using batch experiments. *Journal of Contaminant Hydrology*, 37(1–2):69 – 86.

Schirmer, M., Durrant, G. C., Molson, J. W., and Frind, E. O. (2001). Influence of transient flow on contaminant biodegradation. *Ground Water*, 39(2):276–282.

Schirmer, M., Molson, J. W., Frind, E. O., and Barker, J. F. (2000). Biodegradation modelling of a dissolved gasoline plume applying independent laboratory and field parameters. *Journal of Contaminant Hydrology*, 46(3-4):339 – 374.

Schmidt, T. C., Zwank, L., Elsner, M., Berg, M., Meckenstock, R. U., and Haderlein, S. B. (2004). Compound-specific stable isotope analysis of organic contaminants in natural environments: a critical review of the state of the art, prospects and future challenges. *Analytical and Bioanalytical Chemistry*, 378:283–300.

Scow, K. M. and Hicks, K. A. (2005). Natural attenuation and enhanced bioremediation of organic contaminants in groundwater. *Current Opinion in Biotechnology*, 16(3):246 – 253.

Sherwood Lollar, B., Slater, G. F., Sleep, B., Witt, M., Klecka, G. M., Harkness, M., and Spivack, J. (2001). Stable carbon isotope evidence for intrinsic bioremediation of tetrachloroethene and trichloroethene at area 6, Dover air force base. *Environmental Science & Technology*, 35(2):261–269.

Simoni, S. F., Schäfer, A., Harms, H., and Zehnder, A. J. (2001). Factors affecting mass transfer limited biodegradation in saturated porous media. *Journal of Contaminant Hydrology*, 50(1–2):99 – 120.

Smets, B. F. and Pritchard, P. (2003). Elucidating the microbial component of natural attenuation. *Current Opinion in Biotechnology*, 14(3):283 – 288.

Stolpovsky, K., Martinez-Lavanchy, P., Heipieper, H. J., Van Cappellen, P., and Thullner, M. (2011). Incorporating dormancy in dynamic microbial community models. *Ecological Modelling*, 222(17):3092–3102.

Strobel, K. L., McGowan, S., Bauer, R. D., Griebler, C., Liu, J., and Ford, R. M. (2011). Chemotaxis increases vertical migration and apparent transverse dispersion of bacteria in a bench-scale microcosm. *Biotechnology and Bioengineering*, 108(9):2070–2077.

Sturman, P., Stewart, P., Cunningham, A., Bouwer, E., and Wolfram, J. (1995). Engineering scale-up of in situ bioremediation processes: a review. *Journal of Contaminant Hydrology*, 19(3):171 – 203.

Takahata, Y., Kasai, Y., Hoaki, T., and Watanabe, K. (2006). Rapid intrinsic biodegradation of benzene, toluene, and xylenes at the boundary of a gasoline-contaminated plume under natural attenuation. *Applied Microbiology and Biotechnology*, 73(3):713–722.

Thornton, S. F., Quigley, S., Spence, M. J., Banwart, S. A., Bottrell, S., and Lerner, D. N. (2001). Processes controlling the distribution and natural attenuation of dissolved phenolic compounds in a deep sandstone aquifer. *Journal of Contaminant Hydrology*, 53(3-4):233 – 267.

Thullner, M., Centler, F., Richnow, H.-H., and Fischer, A. (2012). Quantification of organic pollutant degradation in contaminated aquifers using compound specific stable isotope analysis - Review of recent developments. *Organic Geochemistry*, 42(12):1440 – 1460.

Thullner, M., Fischer, A., Richnow, H.-H., and Wick, L. (2013). Influence of mass transfer on stable isotope fractionation. *Applied Microbiology and Biotechnology*, 97(2):441–452.

Thullner, M., Kampara, M., Richnow, H. H., Harms, H., and Wick, L. Y. (2008). Impact of bioavailability restrictions on microbially induced stable isotope fractionation. 1. theoretical calculation. *Environmental Science & Technology*, 42(17):6544–6551.

Thullner, M., Mauclaire, L., Schroth, M. H., Kinzelbach, W., and Zeyer, J. (2002). Interaction between water flow and spatial distribution of microbial growth in a two-dimensional flow field in saturated porous media. *Journal of Contaminant Hydrology*, 58(3–4):169 – 189.

Tufenkji, N. (2007). Modeling microbial transport in porous media: Traditional approaches and recent developments. *Advances in Water Resources*, 30(6–7):1455 – 1469.

Tuxen, N., Albrechtsen, H.-J., and Bjerg, P. L. (2006). Identification of a reactive degradation zone at a landfill leachate plume fringe using high resolution sampling and incubation techniques. *Journal of Contaminant Hydrology*, 85(3-4):179 – 194.

US-EPA (1999). Use of monitored natural attenuation at superfund, RCRA corrective action and underground storage tank sites. Directive number 9200.4-17p. Washington, D.C., USA: Office of Solid Waste and Emergency Response.

US-EPA (2006). Engineering issue in situ and ex situ biodegradation technologies for remediation of contaminated sites. EPA/625/R-06/015. Cincinnati, Ohio, USA: National Risk Management Research Laboratory.

US-EPA (2008). A guide for assessing biodegradation and source identification of organic ground water contaminants using compound specific isotope analysis (CSIA). EPA 600/R-08/148. Ada, Oklahoma, USA: National Risk Management Research Laboratory.

Valocchi, A. J. and Malmstead, M. (1992). Accuracy of operator splitting for advection-dispersion-reaction problems. *Water Resources Research*, 28(5):1471–1476.

van Breukelen, B. M. (2007). Quantifying the degradation and dilution contribution to natural attenuation of contaminants by means of an open system Rayleigh equation. *Environmental Science & Technology*, 41(14):4980–4985.

van Breukelen, B. M., Hunkeler, D., and Volkering, F. (2005). Quantification of sequential chlorinated ethene degradation by use of a reactive transport model incorporating isotope fractionation. *Environmental Science & Technology*, 39(11):4189–4197.

van Breukelen, B. M. and Prommer, H. (2008). Beyond the Rayleigh equation: Reactive transport modeling of isotope fractionation effects to improve quantification of biodegradation. *Environmental Science & Technology*, 42(7):2457–2463.

van Breukelen, B. M. and Rolle, M. (2012). Transverse hydrodynamic dispersion effects on isotope signals in groundwater chlorinated solvents' plumes. *Environmental Science & Technology*, 46(14):7700–7708.

van Leer, B. (1973). Towards the ultimate conservative difference scheme I. The quest of monotonicity. In *Proceedings of the Third International Conference on Numerical Methods in Fluid Mechanics*, volume 18 of *Lecture Notes in Physics*, pages 163–168. Springer Berlin Heidelberg.

Vogt, C., Cyrus, E., Herklotz, I., Schlosser, D., Bahr, A., Herrmann, S., Richnow, H.-H., and Fischer, A. (2008). Evaluation of toluene degradation pathways by two-dimensional stable isotope fractionation. *Environmental Science & Technology*, 42(21):7793–7800.

von Gunten, U. and Zobrist, J. (1993). Biogeochemical changes in groundwater-infiltration systems: Column studies. *Geochimica et Cosmochimica Acta*, 57(16):3895 – 3906.

Werth, C. J., Cirpka, O. A., and Grathwohl, P. (2006). Enhanced mixing and reaction through flow focusing in heterogeneous porous media. *Water Resources Research*, 42:W12414.

Widdel, F. and Bak, F. (1992). Gram-negative mesophilic sulfate-reducing bacteria. In *The Prokaryotes*, pages 3352–3378. Springer New York.

Wiedemeier, T. H., Rifai, H., Newell, C., and Wilson, J. T. (1999). *Natural Attenuation of Fuels and Chlorinated Solvents in the Subsurface*. John Willey and Sons, New York.

Willingham, T. W., Werth, C. J., and Valocchi, A. J. (2008). Evaluation of the effects of porous media structure on mixing-controlled reactions using pore-scale modeling and micromodel experiments. *Environmental Science & Technology*, 42(9):3185–3193.

Wirtz, K. W. (2003). Control of biogeochemical cycling by mobility and metabolic strategies of microbes in the sediments: an integrated model study. *FEMS Microbiology Ecology*, 46(3):295–306.

Worch, E. A. (1993). A new equation for the calculation of diffusion coefficients for dissolved substances. *Vom Wasser*, 81:289–297.

Yolcubal, I., Pierce, S., Maier, R., and Brusseau, M. (2002). Biodegradation during contaminant transport in porous media: V. the influence of growth and cell elution on microbial distribution. *Journal of Environmental Quality*, 31(6):1824–30.

Yu, H., Kim, B., and Rittmann, B. (2001a). The roles of intermediates in biodegradation of benzene, toluene, and p-xylene by Pseudomonas putida F1. *Biodegradation*, 12(6):455–463.

Yu, H., Kim, B., and Rittmann, B. (2001b). A two-step model for the kinetics of BTX degradation and intermediate formation by Pseudomonas putida F1. *Biodegradation*, 12(6):465–475.

Zysset, A., Stauffer, F., and Dracos, T. (1994). Modeling of reactive groundwater transport governed by biodegradation. *Water Resources Research*, 30(8):2423–2434.